이학박사 학위논문

Shear wave velocity and radial anisotropy beneath Northeast Asia from ambient noise tomography

배경잡음 토모그래피를 이용한 동북아시아 지역 하부 전단파 속도 및 이방성 연구

2020년 2월

서울대학교 대학원
지구환경과학부
이 상 준

Abstract

The eastern margin of the Eurasian continental plate has suffered multiple tectonic events including interactions with the subducting Pacific and Philippine Sea plates. Therefore, heterogeneous and distributed extensional basins and intraplate volcanoes in the region are not easily explained with a simple mechanism. To understand seismic activity and complex tectonic processes in the region, reliable seismic velocity models are essential. To construct seismic velocity models for the Northeast Asia, the ambient noise method is used in this thesis. The ambient noise method is widely used for constructing velocity structures of the crust and upper mantle. This method useful for obtaining shorter period data of crustal depth than earthquake data and it is also possible to image structures up to upper mantle depth by using longer periods of surface waves dispersion data. Additionally, the method using ambient noise data is useful for construct seismic velocity models for the regions where have low local seismicity or few available stations inside because Green's functions between station pairs can be obtained from cross-correlations of seismic ambient noise.

In this thesis, seismic velocity models are constructed based on the ambient noise method using various seismic networks for various scale in the Northeast Asia. First, 1-D velocity models for

both the inland and offshore (western East Sea) of the northern Korean Peninsula are constrained based on the results of a Bayesian inversion process using Rayleigh wave dispersion data, which were measured from ambient noise cross correlations between stations in the southern Korean Peninsula and northeast China. The proposed models were evaluated by performing full moment tensor inversion for the 2013 Democratic People's Republic of Korea (DPRK) nuclear test. Using the composite model consisting of both inland and offshore models resulted in consistently higher goodness of fit to observed waveforms than previous models. This indicates that seismic monitoring can be improved by using the proposed models, which resolve propagation effects along different paths in the NKP region. Therefore, the composite model can be useful to understand the characteristics of tectonic earthquakes and monitor anthropogenic seismic events in the NKP.

Second, upper crustal isotropic and radial anisotropic structures beneath Jeju Island are imaged by using ambient noise data from a temporary seismic network. A series of hierarchical and transdimensional Bayesian inversions were performed to construct upper crustal (1–10 km) isotropic and anisotropic structures jointly using surface wave (Rayleigh and Love wave) group and phase velocity dispersion data over a 2–15 s period. The results show that layers of negative anisotropy ($V_{SH} < V_{SV}$) are predominant at

shallower (<2 km) and deeper (>5 km) depths, which was interpreted as reflecting dyke swarms responsible for the more than 400 cinder cones at the surface and the vertical plumbing systems supplying magma from deeper sources, respectively. Additionally, a layer with significantly positive radial anisotropy ($V_{SH} > V_{SV}$, up to 5%) was found at middle depths (2–5 km), and was interpreted as horizontally aligned magma plumbing systems (e.g., sills) through comparisons with several other volcanoes worldwide. In comparison with the isotropic structure, the positive anisotropic layer was separated into upper and lower layers with locally neutral to slightly fast and slower shear wave velocities, respectively, beneath the largest central crater (Mt. Halla). Such a structure indicates that the cooled upper part of the magma plumbing systems formed within the horizontally developed sill complex, and is underlain by still–warm sill structures, potentially with a small fraction of melting. With dykes predominant above and below, the island–wide sill layer and locally high–temperature body at the center explain the evolution of the Jeju Island volcanoes by island–forming surface lava flows and central volcanic eruptions before and after the eruptions of cinder cones.

Lastly, the radial anisotropy model for the East Sea and surrounding region is developed by conducting joint inversion of Love and Rayleigh wave dispersion data using hierachical and transdimensional Bayesian inversion techniques. Using continuous

seismic records of 237 broad-band seismic stations, more than 55,000 group and phase velocities of Love wave fundamental mode are extracted for periods of 5-60 s. Rayleigh wave dispersion data are obtained from a previous study (Kim et al., 2016; for periods of 8-70 s). In addition longer period Love and Rayleigh wave dispersion data from the global dispersion model (Ekstrom, 2011; for periods of 70-200 s) are combined. Therefore, the constructed 3-D radial anisotropy model provides details about the crustal and upper mantle anisotropic structures to the depth of 160 km. The most prominent feature of the model is the variation in the thickness and depth of a layer with strong positive radial anisotropy ($V_{SH} > V_{SV}$), which indicates horizontal upper mantle flows at the top of asthenosphere. The layer exists at depths between 70 and 150 km beneath continental regions compared to the thinner and shallower (30-60 km) structure beneath regions subjected to extension during the Cenozoic. These upper mantle variations represent the undulation of the LAB attributed to complex geodynamic processes in interactions with the preexisting continental lithosphere.

Keyword : ambient noise tomography, Korea Peninsula, nuclear test, surface wave, Bayesian inversion, radial anisotropy, seismic velocity structure, Jeju Island, East sea

Student Number : 2014-30089

Contents

List of Tables

List of Figures

Chapter 1

Introduction

The eastern margin of the Eurasia plate exhibits complex tectonic settings due to interactions with the subducting Pacific and Philippine Sea plates and the colliding India plate and results of tectonic processes remains on the surface as distributed extensional basins,intraplate volcanoes and their heterogeneous features in the region (Wei et al., 2012; Shin et al., 2012; Liu et al., 2017; Van Horne et al., 2017; Zhang et al., 2018). In particular, the East Sea experienced a back-arc extension from the Early Oligocene (~ 32 Ma) to about 15 Ma (Tamaki, 1988; Chough et al., 2000; Yoon et al. 2014; Van Horne et al., 2017). Three major extended basins (Japan, Yamato and Ulleung) and topographic highs (e.g. un-rifted continental crust, volcanic island) are scattered in the East Sea with complex topography. Previous studies using dense seismic networks in the northeast Asia (including northeast China, the southern Korean Peninsula, and the Japanese islands) have reported seismic images for the East Sea and surrounding regions from crust to upper mantle depth (Zheng et al. 2011; Wei et al. 2012; Witek et al. 2014; Shen et al. 2016; Kim et al. 2016b). In order to understand distinctive structures (intraplate volcanoes,

extended basins and etc) in the northeast Asia, it is necessary to study the local scale high-resolution velocity structure of these regions as well as a wide range of studies covering the entire region. Regional models can be a key to explain the complex tectonic history of the region. Proper regional velocity models are also needed for precise analysis of local tectonic earthquakes or man-made seismic sources possibly occurring in the region. Despite the need, there are few local scale studies compared to the number of large scale studies in NE Asia region due to the lack of available data.

In regions with low seismicity or a lack of instrumentation (e.g. the northern Korean Peninsula region, Jeju Island and East Sea), cross-correlation of seismic ambient noise can be utilized to obtain Green's functions between station pairs using surrounding seismic networks (Shapiro et al. 2005; Kang and Shin 2006; Bensen et al. 2007; Pawlak et al. 2011; Lee et al., 2015). The method is widely used for investigating velocity structures of the crust and upper mantle because it is effective for obtaining shorter period data of crustal depth than earthquake data (Bensen et al. 2007; Kang and Shin 2006; Choi et al. 2009; Pawlak et al. 2011; Shen et al. 2016; Kim et al. 2016b). Additionally, seismic anisotropy also can be constrained by joint inversion of Rayleigh and Love wave data from cross-correlations of three-components ambient noise data (Beghein et al., 2014; Jaxybulatov et al., 2014; Mordret et al.,

2015; Lynner et al., 2018; Russell et al., 2019). Radial anisotropy (i.e., velocity differences between horizontally (V_{SH}) and vertically (V_{SV}) polarized shear waves), provides reliable information about tectonic processes in the cust, lithospheric ,asthenospheric upper mantle and the associated variation of the lithosphere–asthenosphere boundary (LAB) (Crampin, 1981, 1984, 1989; Montagner, 1998; Shapiro et al., 2004; Meissner et al., 2006; Karato et al., 2008; Long and Becker, 2010; Mainprice, 2010; Eilon et al., 2014; Russell et al., 2019). Anisotropy observed in the crust is generally explained by a shape–preferred orientation (SPO) which is generally caused by structures aligned to a specific direction (e.g., crack, fault, melt lenses, etc.) or crystallographic–preferred orientation (CPO) which is related to mineral alignments due to sedimentation and deformation (Crampin, 1981, 1984, 1989; Shapiro et al., 2004; Meissner et al., 2006; Ko and Jung, 2015; Jung, 2017; Almqvist and Mainprice, 2017; Kim and Jung, 2019). In the upper mantle scale, the seismic radial anisotropy is mainly due to the lattice preferred orientation (LPO) related with the relative motion of the mantle convection and plate or fossilized fabric in lithosphere from past tectonic activities (Ekström and Dziewonski, 1998; Montagner, 1998; Debayle and Kennett, 2000; Karato et al., 2008; Long and Becker, 2010; Mainprice, 2010; Beghein et al., 2014; Eilon et al., 2014; Russell et al., 2019). Consequently, measured radial anisotropy provides answers to questions related

to more detailed and specific tectonic processes in the crust and upper mantle (Fouch and Rondenay, 2006; Maggi et al., 2006).

In chapter 2, 1-D velocity models for the northern Korean Peninsula region were developed using Rayleigh wave dispersion data obtained from ambient noise cross-correlations between permanent network stations in southern Korean Peninsula and a temporary network in northeast China (Northeast China Extended Seismic Array, NECESSArray). Two different models were presented to account for different propagation paths along the inland and offshore regions of the Korean Peninsula. The reliability of the estimated 1-D models was verified by calculating full model tensor solutions for the 2013 North Korea explosion nuclear test.

In chapter 3, isotropic and anisotropic shear wave velocity models for the shallow crust (<10km) of Jeju Island were constructed using ambient noise tomography from the continuous recordings of 20 temporary and three permanent stations deployed over three years. The fundamental mode of surface wave (Rayleigh and Love waves) group and phase velocity dispersion curves were measured using three-component continuous data. To better constrain anisotropic parameters, a recently developed transdimensional and hierarchical Bayesian technique was used for joint inversion, which employs Rayleigh and Love wave data and estimates isotropic and anisotropic structures simultaneously.

Constructed three-dimensional (3-D) seismic images revealed the magma plumbing system in the shallow crust beneath Jeju Island

In chapter 4, to understand the complex tectonic history of these regions and to clarify relationships between the dominant low velocity anomalies and the surrounding intraplate volcanoes, a three-dimensional radial anisotropy model in northeast Asia was constructed using hierarchical and transdimensional Bayesian inversion techniques with different types of dispersion data up to the depth of the upper mantle (~ 160 km). Constructed radial anisotropic models could be helpful to understand the tectonic process of the opening and the intraplate volcanism in the upper mantle beneath the ES and surrounding regions.

Chapter 2

1-D velocity model for the North Korean Peninsula from Rayleigh wave dispersion of ambient noise cross-correlation

2.1. Introduction

A reliable seismic velocity model is essential for monitoring and analyzing seismic activity and associate hazards. In addition, a well-determined seismic velocity model provides basic information for understanding the tectonic process of a region. However, seismic velocity structures in the northern Korean Peninsula (NKP) region in northeast Asia are not well studied due to a lack of available seismic networks. In contrast, dense seismic networks have been installed in the rest of northeast Asia, including northeast China, the southern Korean Peninsula (SKP), and the Japanese islands, and seismic velocity structures are therefore extensively mapped in these regions (e.g., Zheng et al. 2011; Wei et al. 2012; Witek et al. 2014; Shen et al. 2016; Kim et al. 2016b). In particular, one-dimensional (1-D) structures of the SKP have been estimated from studies using receiver functions and seismic waveform data (Chang and Baag 2005; Chang and Baag 2006; Lee and Baag 2008; Han et al. 2010; Kim et al. 2011; Kim et al. 2016a). Studies of the NKP region (e.g., Shin and Baag 2000; Ford et al. 2010) have relied on approximate velocity structures based on the SKP or global averages.

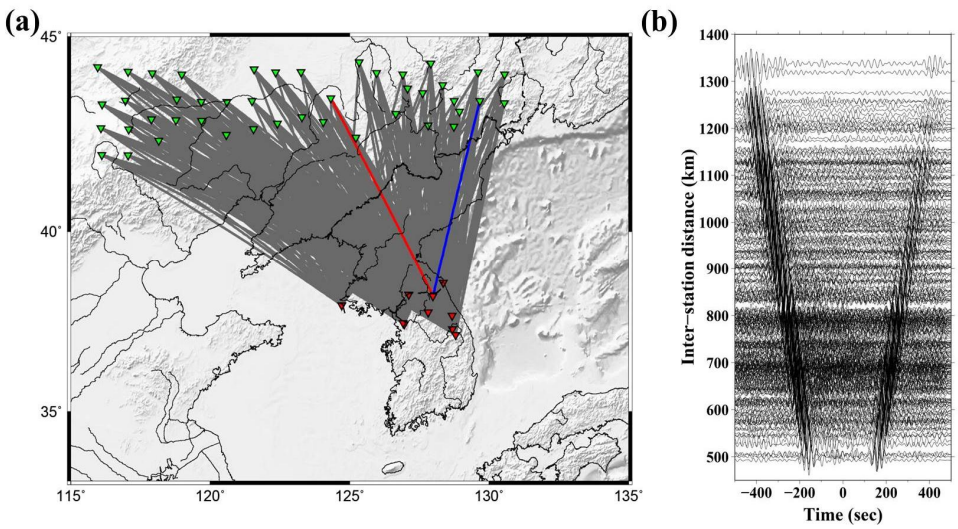

Figure 2.1. (a) Location of Korea Meteorological Administration (KMA) and Korea Institute of Geoscience and Mineral Resources (KIGAM) stations (red triangles) and the NECESSArray (green triangles), as well as all possible 450 ray paths (gray blue lines). (b) Calculated cross-correlation section for ZZ cross-correlations with application of a 10–30 s bandpass filter

Despite relatively low seismicity, monitoring of seismic activity in the NKP region is particularly important. The largest instrumental earthquake (Mw 6.2) in the Korean Peninsula occurred near Pyongyang in North Korea, where more historical records of significant earthquakes are found (Kang and Jun 2011; Kyung et al. 2016). In addition, six nuclear explosion tests have been conducted since 2006 by the Democratic People's Republic of Korea (DPRK) government, generating the need for effective monitoring and detection of future potential activity (Hong and Rhie 2009; Barth 2014; Cesca et al. 2017).

However, complexities along propagation paths between the NKP and surrounding regions with dense instrumentation may thwart high-precision analysis for seismic sources and structures in the NKP. Seismic waves from events in the western NKP predominantly propagate through inland areas to seismic networks in the SKP (Fig. 2.1). On the other hand, offshore areas (the East Sea or Japan Sea) are included in the propagation paths from seismic events on the eastern coast of the NKP to stations in the SKP. According to studies on the crustal and upper mantle structure of northeast Asia (Tamaki 1988; Zheng et al. 2011; Lee et al. 2015), there is a significant difference in Moho depth along the margin of the Korean Peninsula, where crustal thinning due to opening of the East Sea has been suggested (Tamaki 1988; Yoon et al. 2014). In addition, velocity changes between the Korean

Peninsula and East Sea have been reported in previous studies (e.g., Zheng et al. 2011; Witek et al. 2014; Kim et al. 2016b) and research into wave propagation across the continental margin has indicated strong effects of such marginal changes in crustal structure (Hong et al. 2008; Ford et al. 2009; Furumura et al. 2014).

In regions with low seismicity or a lack of instrumentation, such as the NKP region, cross-correlation of seismic ambient noise can be utilized to obtain Green's functions between station pairs (Shapiro et al. 2005; Bensen et al. 2007). The method is widely used for investigating velocity structures of the crust and upper mantle because it is effective for obtaining shorter period data of crustal depth than earthquake data (e.g., Bensen et al. 2007; Kang and Shin 2006; Choi et al. 2009; Pawlak et al. 2011; Shen et al. 2016; Kim et al. 2016b). In this study, we developed 1-D velocity models for the NKP region using Rayleigh wave dispersion data obtained from ambient noise cross-correlations between permanent network stations in SKP and a temporary network in northeast China (Northeast China Extended Seismic Array, NECESSArray). Two different models were presented to account for different propagation paths along the inland and offshore regions of the Korean Peninsula. The reliability of the estimated 1-D models was verified by calculating full model tensor solutions for the 2013 North Korea explosion nuclear test.

2.2. Data and methods

2.2.1. Data and processing

To obtain Rayleigh wave group and phase velocities, we used the vertical component of broadband continuous waveforms. Data were recorded at ten stations from KIGAM (Korea Institute of Geoscience And Mineral Resources) and KMA (Korea Meteorological Administration) installed in the northern part of SKP (above 36° N), and 45 stations from NECESSArray in the southern part of northeast China (below 45° N) from January 2010 to December 2011 (Fig. 2.1). For verification of the resulting models using moment tensor inversions, we used 2013 North Korea nuclear explosion test records for six broadband seismic stations in SKP and northeast China (Fig. 2.2)

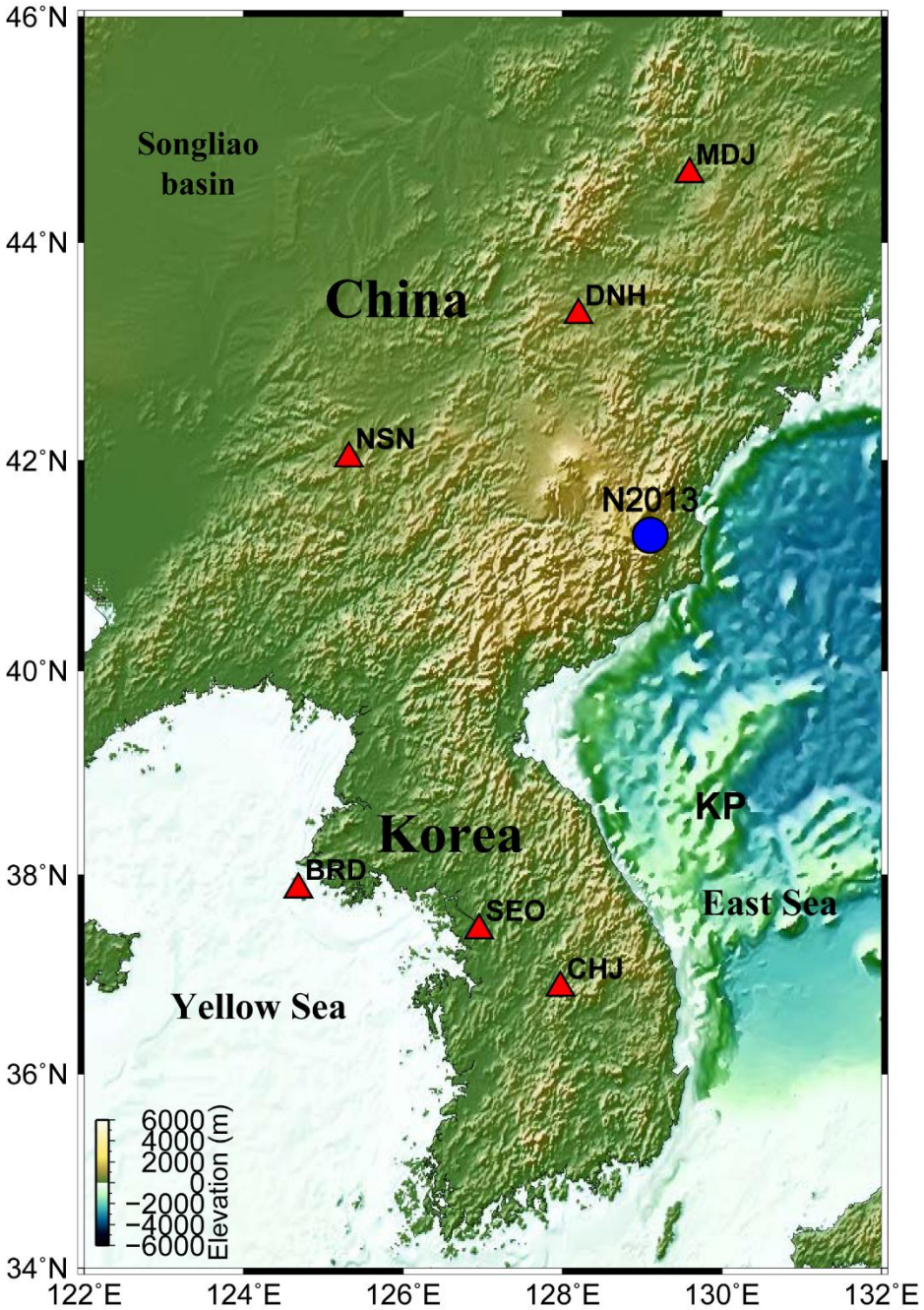

Figure 2.2. Location of the 2013 underground nuclear explosion (blue circle) and stations (red triangle) used to moment tensor inversion (KP = Korea Plateau)

To construct the 1-D velocity model, we measured group and phase velocity dispersion data of the fundamental mode of Rayleigh waves using Green's function waveforms obtained from ambient noise cross correlation. Data preprocessing is similar to that of previous studies (e.g., Bensen et al. 2007; Lee et al. 2015). Instrument response, mean, and trend were removed from the vertical component continuous waveforms, which were divided into 1-day segments. Then, a band-pass filter between 0.01 and 0.45 Hz was applied. To reduce the effects of transient signals with large amplitudes, e.g. earthquakes, one-bit normalization was performed in the time domain. For crosscorrelation functions of all possible pairs, a spectral whitening procedure was applied by dividing a 40-point moving average in the frequency domain. The distribution of stations generates 450 inter-station paths along the NKP mainland, East Sea, and Yellow Sea (Fig. 2.1). Signals with velocities of 3 to 4 km/s, corresponding to fundamental mode Rayleigh waves, were clearly observed in the cross-correlogram sections as a function of time and inter-station distance (Fig. 2.1). Potential interference of other signals from consistent noise sources such as the Aso volcano (e.g., Zheng et al. 2011; Lee et al. 2015) were not found in our data. Hence, we used an average of the positive and negative lag of the cross-correlogram to extract Green's function for each station pair, which was used to measure group and phase velocity dispersion data by applying the multiple filter technique (Herrmann

and Ammon 2004; Yao et al. 2006). In our procedure, dispersion curves were automatically measured based on the reference group and phase dispersion curves, which were obtained from a model of the SKP (Kim et al. 2011) and the AK135 model (Kennett et al. 1995) (Fig. 2.3).

To account for different features of wave propagation due to the complex marginal structures mentioned in section 1, we constructed two individual models for two distinct propagation paths. One model was for the propagation path through the inland of NKP (hereafter Mod_Land) and the other was for propagation paths through the East Sea region (hereafter Mod_Sea) (Fig. 2.4). Each model was constructed based on the 1-D model from Bayesian inversion using average dispersion curves (see section 2.2), which mainly sample each propagation path. The standard deviation of the dispersion curves was used as the observation error for the input parameter

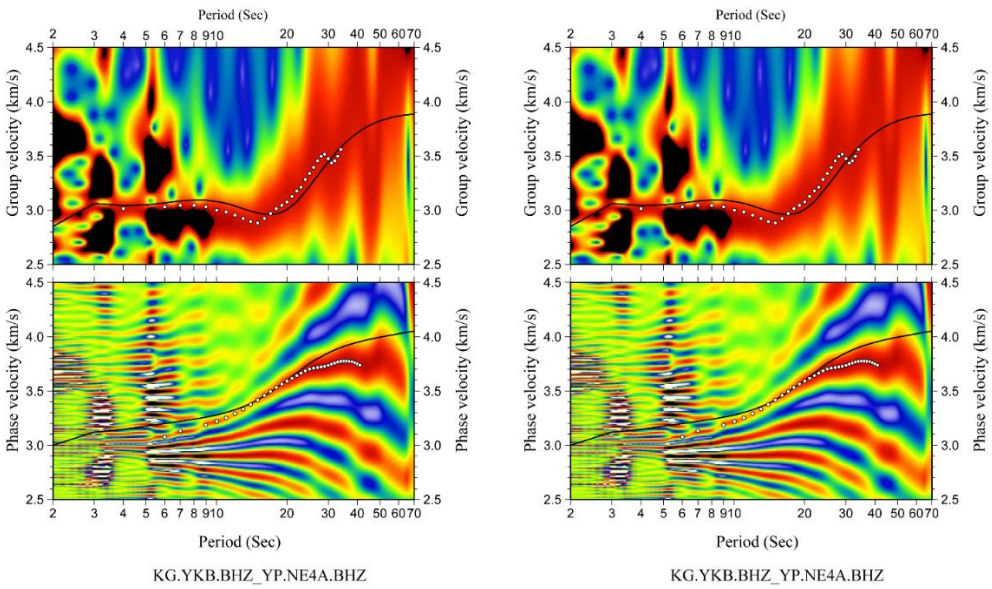

Figure 2.3. Examples of estimated group and phase velocity dispersion curves between YKB-NE47 (red line in Fig. 2.1) and YKB-NE4A (blue line in Fig. 2.1). Background images are the FTAN diagrams for each curve. Ray paths exclusively sampling the northern Korean Peninsula show clear FTAN diagrams and well estimated group and phase velocity dispersion points

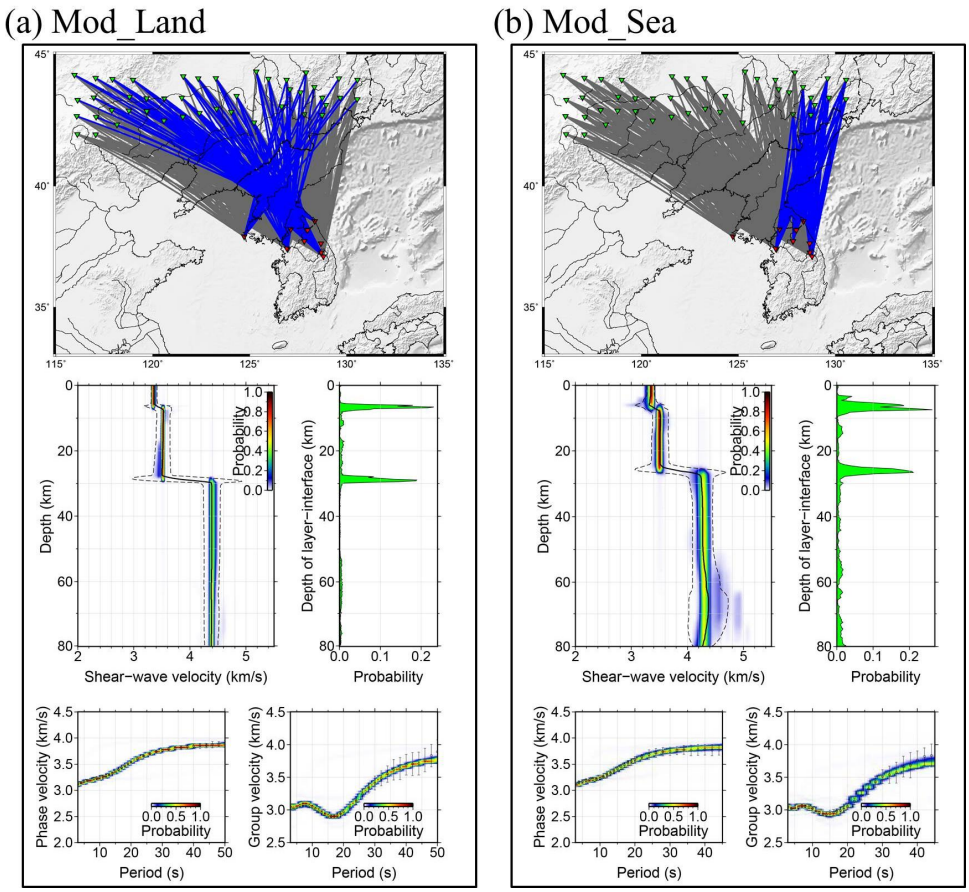

Figure 2.4. (a), (b) 1-D shear velocity models obtained from Bayesian inversion using Rayleigh wave dispersion curves for both cases (Mod_Land, Mod_Sea). Top: all possible ray paths (gray lines) and used ray paths (blue line) for each model. Location of the Korea Meteorological Administration (KMA) and Korea Institute of Geoscience and Mineral Resources (KIGAM) stations (red triangles) and the NECESS array (green triangles). Middle: the posterior probability distribution (PPD) of the model parameters and the PPD of layer boundaries. Bottom: posterior distributions of predicted synthetic data with observed data.

2.2.2. Bayesian inversion

The obtained surface wave dispersion data were inverted to estimate the 1-D shear wave velocity models for the corresponding path coverage regions. It is known that surface wave dispersion data have broader sensitivities to shear wave velocity structures than ballistic wave data such as body wave travel times (Ritzwoller et al. 2011; Obrebski et al. 2011). In this study, therefore, we utilized a Bayesian inversion method to account for potential non-uniqueness of solutions by estimating uncertainties, which were deduced from posterior probability distributions (PPD) of inversion parameters (Bodin et al. 2012; Kim et al. 2016a; Kim et al. 2016b). In particular, robust inversion uncertainties were calculated through a recently developed transdimensional and hierarchical technique (see Kim et al. 2016a and Kim et al. 2017 for further details). In this approach, probability distributions of the number of layers and the levels of data errors (variances) are sampled, through a Markov chain Monte Carlo method, together with those of other inversion parameters (e.g., layer thicknesses and velocities in each layer). Without applying regularization in the inversion process, this scheme systematically controls the balance between model complexity (i.e., the number of layers) and the degree of data fitting (i.e., the level of data errors). As a consequence, inversion results and corresponding uncertainties are less biased by arbitrary inversion settings. In addition, the approach is particularly useful in

joint inversions as group and phase velocity dispersions are used together. The hyper-parameters for implementing the hierarchical scheme encompass the effect of different data sensitivities between different types (group and phase velocity) of data.

We used Rayleigh wave group and phase velocities from the average of the dispersion curves for each model (3~50 s-period for Mod_Land; 3~45 s-period for Mod_Sea). Bayesian inversions were performed for parameters consisting of Vs ($2.0 \leq Vs \leq 5.5$ km/s), Vp/Vs ratio ($1.7 \leq Vp/Vs \leq 2.0$), interface depth (up to 100 km), number of layers (between 2 and 30), and scaling factors for the level of data noise (between − 5.0 and 5.0). In each inversion, 2000 iterations were progressed and the previous 1000 samples were discarded to obtain converged posterior models. We simultaneously used 64 parallel chains to finally form a mean model from 1000 posterior sampled models. Figure 2.4 shows the prior ranges and estimated PPD for two different datasets. Based on the assumption that the PPD can be approximated as Gaussian shapes, we present inversion uncertainties with $\pm$ 2 standard deviations of the sampled models.

2.3. Results and discussion

2.3.1. Models

The final two models are determined in the form of approximately two layers over a half-space model. The depth of layer boundaries is fixed manually based on peaks (the highest probability in a certain range of depths) of the PPD of the layer boundaries (Fig. 2.4). The velocity of each layer is determined by taking average values over each layer. Then, P velocity models are obtained by multiplying the determined S velocity models by the Vp/Vs ratio (Table 1). In Mod_Land, the estimated depth of the Moho is 30 km, which is 5 km deeper than in Mod_Sea (Figs. 2.4 and 2.5). Comparing Mod_Land and Mod_Sea, the depth of the uppermost crustal layer is similar (6.5~7 km) and the difference in velocity is only approximately 0.5%. For the second layer and half-space, velocities in Mod_Land are approximately 1.6% faster than that of Mod_Sea in both layers.

We qualitatively evaluate the obtained models by comparing with previous 1-D velocity models in the SKP. The first is a model determined through travel time data and waveform modeling of seismic phases of local earthquakes (Chang and Baag 2006; Mod_C&B). The second is a model that best fits the observation waveforms determined by a full-grid search (Kim et al. 2011; Mod_Kim). Mod_Land is generally similar to Mod_C&B and Mod_Kim, even taking into account the different number of layers

(four) (Fig. 2.5). The Moho depth in Mod_Land developed using inland sampling data is similar (~ 30 km) to those in Mod_C&B and Mod_Kim and the velocity difference of each layer of Mod_C&B and Mod_Kim compared with Mod_Land is less than 4%, except for the lower crust part. It is known that the lower crust has been significantly modified by tectonic processes (e.g., Chough et al. 2000) in each region of the Korean Peninsula.

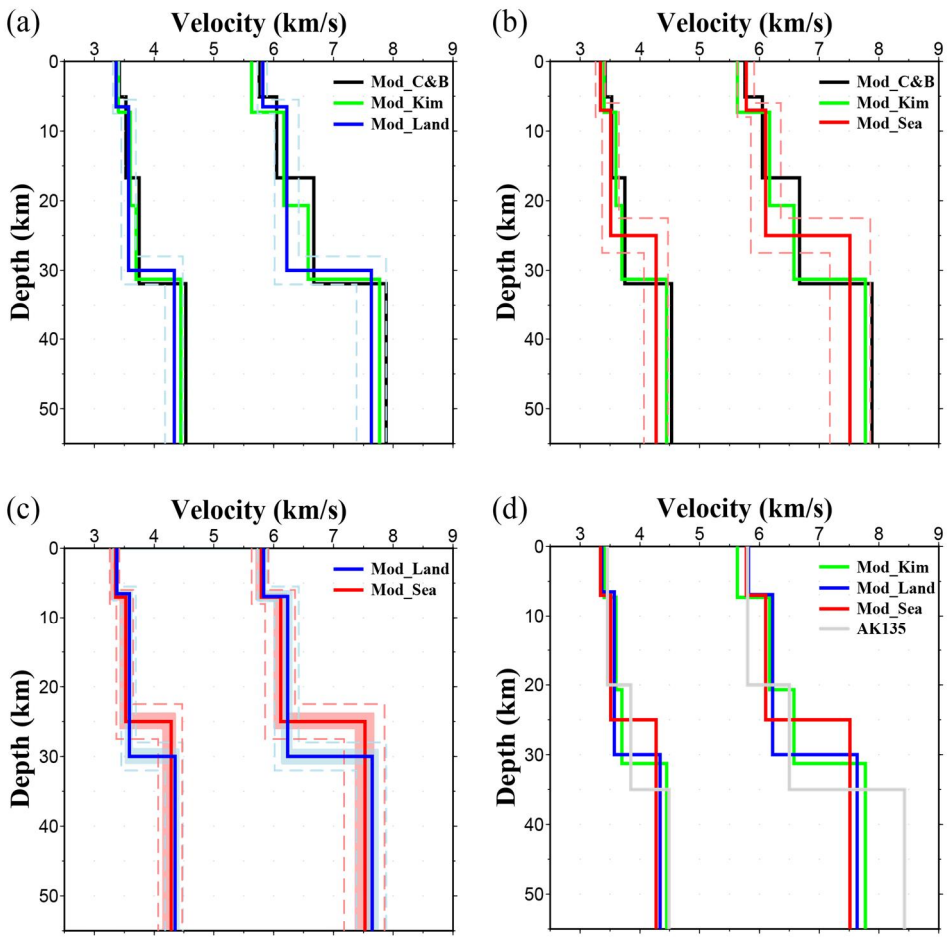

Figure 2.5. (a) 1-D velocity model of Mod_Land and that of previous studies. Dashed line represents 2σ of Mod_Land; (b) same as (a) but for Mod_Sea; (c) comparison of Mod_land and Mod_Sea. Shaded area dashed lines (light blue: Mod_Land; light red: Mod_Sea) represent 1, 2σ of Mod_Land and Mod_Sea; and (d) models used for moment tensor inversions

Model	L1	L2	S1	S2	S3	P1	P2	P3
Mod_Land	6.5 ±1.0 (±1σ)	30.0 ±1.1	3.36 ±0.03	3.57 ±0.07	4.34 ±0.08	5.82 ±0.05	6.22 ±0.1	7.64 ±0.13
Mod_Sea	7.0 ±1.0	25.0 ±1.2	3.34 ±0.02	3.51 ±0.09	4.27 ±0.1	5.78 ±0.04	6.11 ±0.13	7.52 ±0.17

Table 2.1. Model parameters of Mod_Land and Mod_Sea. L1 and L2 = bottom depth of 1st and 2nd layer; S1–S3 = S wave velocity of each layer; and P1–P3 = P wave velocity of each layer

The influence of sampling paths through northeast China on Mod_Land is accounted for by the portion of inter-station paths that crosses the region. Considering previous studies on velocity structure in northeast Asia, the average crustal velocity in northeast China (~ 3.6 km/s) is not significantly different from that in the Korean peninsula (Zheng et al. 2011; Shen et al. 2016). In Songliao basin, the uppermost crustal velocity is slower than in the Korean peninsula by approximately 10% due to thick sediments. The Moho thickness is also relatively shallow; less than 30 km (Guo et al. 2015; Shen et al. 2016). However, the stations selected in this study are located at the boundary of the Songliao basin and the portion of paths through the basin does not exceed 20% of their total path-lengths. In addition, the standard deviation of the average dispersion curve for Mod_Land is small, even though it used paths across various regions (Fig. 2.4). Consequently, we conclude that paths are less influenced by the northeast China region and Mod_Land is sufficiently representative of NKP.

In Mod_Sea, the depth of the Moho is approximately 25 km, which is relatively shallow compared with Mod_Land and South models. Moreover, the velocity difference from Mod_Land is ~ 2% in each layer. This relatively small discrepancy indicates that, as previously suggested, the eastern margin of NKP is not completely oceanic crust but a rifted continental margin formed during expansion (Tamaki 1988; Yoon et al. 2014).

2.3.2. Model validation

To check the reliability of the constructed 1-D models, we perform full moment tensor (FMT) inversions for the 2013 DPRK nuclear experiment using the time domain moment tensor (TDMT) inversion method (Dreger and Helmberger 1993; Ford et al. 2009; Rhie and Kim 2010). The models are evaluated by measuring the goodness of fit between observed waveforms and those resulting from the FMT inversions. The hypocenter location and origin time information from a previous study (Barth 2014) is used. We select three-component waveform data from MDJ, DNH, NSN, BRD, CHJ, and SEO stations to use in the inversions, ensuring data conditions with good azimuthal coverage and high signal-to-noise ratio. For comparison, Mod_Kim and AK135 (Kennett et al. 1995) are also tested. Green's function sets of three fundamental faults and a volumetric source (Saikia, 1994; Minson and Dreger 2008) are produced for each of the four models. Obtained waveforms of Green's functions and observed data are bandpass filtered in the range of 10-50 s. Arbitrary time shifts are often applied in the TDMT process to empirically calibrate the inaccuracy of the used velocity model. In our model assessment, the time shift cannot be used to check model performance in terms of absolute times of phases as well as relative waveform similarities. For the goodness of fit, the variance reduction (VR) is calculated between synthetic and observation waveforms:

$$VR = \left(1 - \frac{\sum_i^n \sqrt{(O_i - S_i)^2}}{\sum_i^n \sqrt{o_i^2}}\right) \times 100,$$

where O_i represents the i−th data−point of the observation with n points, and S_i represents the same but for synthetic data. Using data from the six stations, we perform TDMT inversions for all possible combinations (4,096) of Green's functions. For each station, four different sets of Green's functions are generated using the four different models. Then, each inversion is performed using a composite set of Green's functions allowing the same or different models between stations.

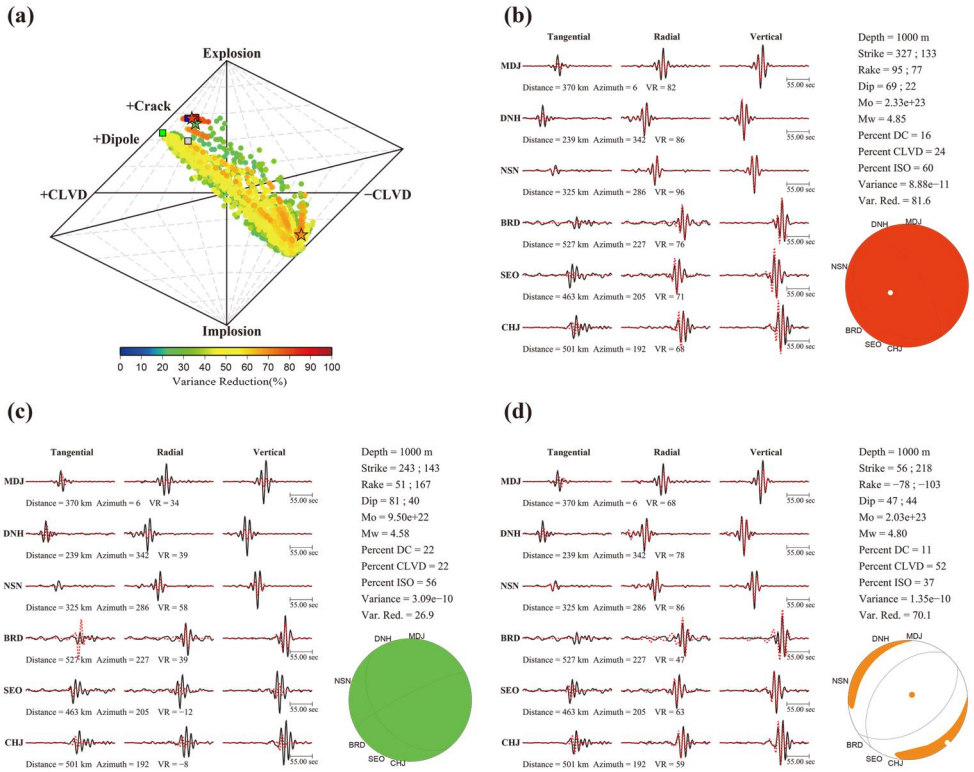

Figure 2.6. (a) Hudson source type diagram for all possible combinations of each model. Red star represents the best result of this study. Blue, red, green, and grey squares represent source type using Mod_Land, Mod_Sea, Mod_Kim, and AK135, respectively; (b) the best moment tensor solution using Mod_Land (BRD, DNH, MDJ, NSN) and Mod_Sea (CHJ, SEO); and (c) and (d) moment tensor solutions of source type for green star (MDJ−Mod_Kim; DNH−Mod_Sea; NSN−Mod_Sea; BRD−Mod_Kim; SEO−Mod_AK135; CHJ−Mod_Kim) and orange star (MDJ−Sea_Kim; DNH−Mod_Sea; NSN−Mod_Land; BRD−Mod_Kim; SEO−Mod_Sea; CHJ−Mod_Sea). Observations are solid lines (black) and simulations are dashed (red)

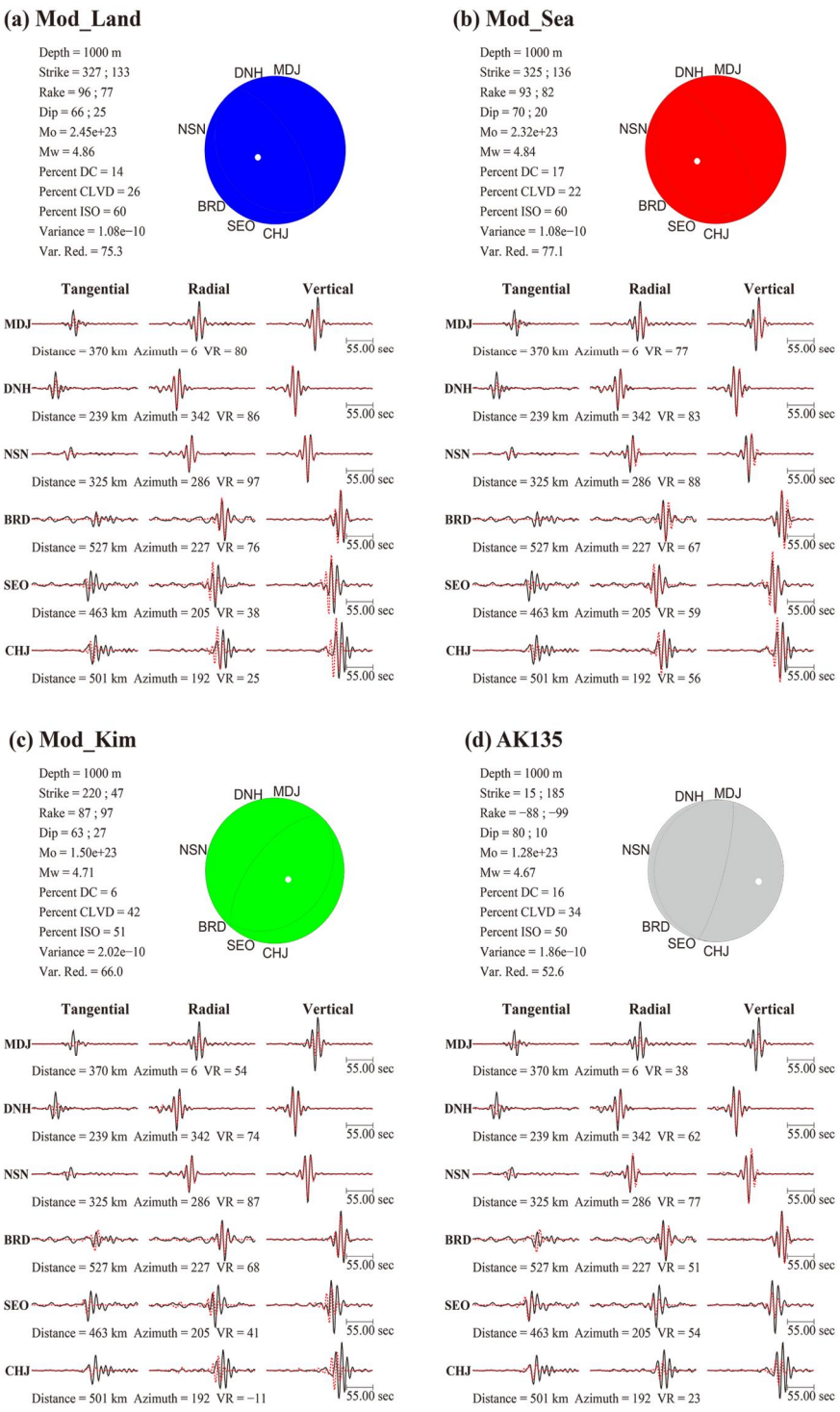

Figure 2.7. (a) Moment tensor solution using Mod_Land only; (b) moment tensor solution using Mod_Sea only; (c) moment tensor solution using Mod_Kim only; and (d) moment tensor solution using AK135 only.

Figure 2.6 shows the results of the test, where the VR values for all combinations of Green's functions range from 10.5 to 81.6% (Fig. 2.6a). The combination of Green's functions from Mod_Land for MDJ, DNH, NSN, and BRD and from Mod_Sea for CHJ and SEO has the highest average VR (Fig. 2.6b). Interestingly, this result corresponds to the spatial coverage of dispersion data used to develop the models. Considering the propagation paths between the source and receivers, seismic waves mainly propagate through inland areas to MDJ, DNH, NSN, and BRD stations. On the other hand, CHJ and SEO stations record waveforms that spend much longer in the East Sea. Because Mod_Land and Mod_Sea are models developed for inland and East Sea regions, respectively, results of the FMT inversion tests indicate that the structural differences between paths through the inland and eastern margin of NKP influence the FMT results. These effects are accounted for by our estimated models.

The value of VR is 81.6% for the optimal combination of Green's functions (Fig. 2.6b). This compares with VRs of inversions using single models of the Mod_Land (75.3%), Mod_Sea (77.1%), Mod_Kim (66.0%), and AK135 (52.6%), which show consistently lower VRs by 4.5 to 29.0% (Figs. 2.6 and 2.7). The FMT solution with the highest VR plotted on the Hudson source type diagram (Hudson et al. 1989) is similar to source types calculated in previous studies (Ford et al. 2009; Cesca et al. 2017). Interestingly,

FMT solutions vary from opening to closing of cracks, even for those with reasonably high VRs (> 60%) (Fig. 2.6a). This indicates that the source type can be misjudged by inaccurate velocity models. Figures 2.6 c and d present inversion examples using different combinations of models, where solutions with high VRs (Fig. 2.6d; VR = 70.1%) can be the opposite (implosion), while an obtained solution with low VR (Fig. 2.6c; VR = 26.9%) has an extremely similar FMT solution. It is noted through this test that structural models used to calculate Green's functions can play a major role in FMT calculation, particularly when the isotropic component is dominant, which makes the inversion unstable. The presented models may thus contribute to stabilizing FMT solutions for seismic events in NKP by using them for corresponding paths along continental regions around NKP and oceanic regions along the margin of NKP.

The FMT inversion results show that the Mod_Land and Mod_Sea models can improve the seismic monitoring of DPRK nuclear tests. Furthermore, this work indicates that the effect of wave propagations should be considered; developing more refined path-specific 1- D models or higher-dimensional models may further improve the FMT inversion results. In the future, radially anisotropic models can also be developed and tested because this study only assumes isotropic structures based on Rayleigh wave dispersion data.

2.4. Conclusion

In this study, we develop 1-D velocity models representing the inland and eastern margin of the NKP through the Bayesian inversion method using dispersion curves from the ambient noise records of surrounding networks (Figs. 2.4 and 2.5, Table 1). Although the velocity difference is small between Mod_Land and Mod_Sea models, Moho depths are clearly identified at 30 and 25 km, respectively. Mod_Land is similar to previous 1-D models (Mod_C&B and Mod_Kim) in the SKP region, which indicates that continental velocity structures in the Korean Peninsula are generally similar. Model verification using the FMT inversion for the 2013 DPRK nuclear test shows that a composite set of models consisting of Mod_Land and Mod_Sea for paths along the inland and eastern margin of NKP, respectively, provide a better solution in terms of the goodness of fit (VR) to waveforms than cases using either one of the models or with any possible combination of AK135 and Mod_Kim. Additionally, we confirm the reliability of the composite model, which may lead to improved FMT estimation for seismic events in NKP.

Chapter 3

Upper crustal shear wave velocity and radial anisotropy beneath Jeju Island volcanoes from ambient noise tomography

3.1. Introduction

Knowledge of the magma plumbing system in the shallow crust is important for understanding the evolution of volcanoes at the surface (Brenquier et al., 2007; Huang et al., 2015; Li et al., 2016; Spica et al., 2015; Spica et al., 2017). Though ideally simple vertical dyke systems have been assumed in many studies, recent higher-resolution studies using seismic, geologic, and geodetic data have shown that the various types of magma structures, including dykes, chambers, and sills, interact with each other in the formation of volcanoes (Klügel et al., 2005; Ishizuka et al., 2008; Peltier et al., 2009; Paulatto et al., 2010; Chadwick et al., 2011; Bagnardi & Amelung, 2012; González et al., 2013; Jaxybulatov et al., 2014; Mordret et al., 2015; Huang et al., 2015; Tibaldi, 2015). It has been suggested that the development of complex magma plumbing systems is affected by the local stress field or inherent structures (e.g., topography, fault, collapsed caldera structure, etc.), not simply by tectonic regimes related to the motion of neighboring plates (Ishizuka et al., 2008; Tibaldi et al., 2015; González et al., 2013). Therefore, more comprehensive and detailed analysis is required to better understand the development of volcanic systems.

Many seismic studies have been conducted to detect magma structures in the crust using local travel time tomography and ambient noise tomography (Aloisi et al., 2002; Brenguier et al., 2007; Stankiewicz et al., 2010; Huang et al., 2015), primarily by

identifying velocity anomalies. These approaches may be more effective for obtaining high-resolution images by accumulating many data points from dense temporary and permanent seismic stations (Jaxybulatov et al., 2014; Mordret et al., 2015; Jeddi et al., 2017; Godfrey et al., 2017; Benediktsdóttir et al., 2017; Lynner et al., 2018; Jiang et al., 2018). Another important and independent property is seismic anisotropy, which is sensitive to the alignment or layering of magma structures in the relatively isotropic upper crust (Jaxybulatov et al., 2014; Mordret et al., 2015; Lynner et al., 2018). Therefore, studies into which both isotropic and anisotropic structures are incorporated, especially using data from many stations, provide unique opportunities to validate each other and to identify more detailed and specific processes in the development of volcanoes. Rayleigh and Love wave dispersion data from ambient noise are particularly useful for estimating isotropic and radially anisotropic velocity structures due to their dominant signals in obtained waveform data and less biased ray coverage (e.g., Jaxybulatov et al., 2014; Mordret et al., 2015; Jeddi et al., 2017; Lynner et al., 2018).

Jeju Island (JI) comprises intraplate volcanoes within a relatively small area (2,400 km^2) located in the southwest offshore of the Korean Peninsula; it is separated by more than 600 km from the southern (and nearest) subduction zone. There has been no evidence of current volcanic activity on or proximal to JI, and the nearest intraplate volcano is 200-km away (Tatsumi et al., 2004; Brenna et al., 2012; Brenna et al., 2015; Yoon et al., 2014; Koh et al., 2013) (Fig. 3.1). Since there is a lack of volcanic activity and no seismicity, volcanic structures have not been well studied seismically. Though there have been some regional studies, including or JI (e.g., Zheng et al., 2011; Kim et al., 2016), it is difficult to identify magma structures beneath its volcanoes.

Recently, Song et al. (2018) presented teleseismic tomography results using data from a temporary seismic network installed on JI, which suggested the existence of a complex, lithosphere-scale magma structure in which sublithospheric magma interacts with the lithosphere along multiple, laterally spreading paths. Moreover, they suggested the existence of a relatively thicker continental lithosphere in the north and west of JI that could cause decompression melting via localized mantle convection. This model would explain the isolated occurrence of volcanism on JI, far from subduction zones and other intraplate volcanoes, and shows that JI was formed by multi-step eruptions of magma of varied durations, spatial existents, and compositions. Taking into account the

methods and data of Song et al. (2018), the shallow crust of JI cannot be estimated due to the lack of resolution, which is critical to fully explaining how magma is supplied to and distributed among surface volcanoes, as well as how the central crater formed near the surface. In this study, we aimed to estimate shallower (~5 km) magma plumbing structures beneath volcanoes on JI using data from the same stations as reported by Song et al. (2018).

In this study, we constructed isotropic and anisotropic shear wave velocity models for the shallow crust (<10km) of JI using ambient noise tomography from the continuous recordings of 20 temporary and three permanent stations deployed over three years. To investigate volcanoes with records of recent eruptions (i.e., during the Holocene) but without current activity, ambient noise tomography using dense temporal network data was found to be a suitable approach. In particular, magma structures at various depths, including in the shallow crust, may be effectively estimated using this method, depending upon the size of the seismic array (Jaxybulatov et al., 2014; Mordret et al., 2015; Kim et al., 2017; Jiang et al., 2018). We measured the fundamental mode of surface wave (Rayleigh and Love waves) group and phase velocity dispersion curves using three-component continuous data. To better constrain anisotropic parameters, a recently developed transdimensional and hierarchical Bayesian technique was used for joint inversion, which employs Rayleigh and Love wave data and

estimates isotropic and anisotropic structures simultaneously. Through these analyses, we were able to generate three-dimensional (3-D) seismic images that reveal the magma plumbing system in the shallow crust beneath JI for the first time.

3.2. Geologic Setting and background

3.2.1. Geologic history and previous studies

Similar to other intraplate volcanoes distributed around the Korean Peninsula, JI has existed in an isolated location without neighboring volcanoes since its formation during the early Pleistocene (~1.7 Ma). Until the recent crater-forming eruption at the center of JI (~3.7 ka), JI suffered four stages of eruptions with variable magma compositions, from the alkali to tholeiitic basalts (Tatsumi et al., 2004; Brenna et al., 2012; Koh et al., 2013;Yoon et al., 2014; Brenna et al., 2015). As a result, the largest volcano (Mt. Halla) was created at the center of the island with ~400 monogenic cinder cones distributed across JI (Park et al., 2008; Shin et al., 2012; Koh et al., 2013; Brenna et al., 2015).

Previous studies on the formation of JI volcanoes have mainly focused on the magma source and timing of eruptions based on the geochemical properties of volcanic rocks, which indicated that the magma originated either from interactions between a shallow mantle

and a deep plume (Tatsumi et al., 2004; Nakamura et al., 1990) or from the sublithospheric upper mantle (Kim et al., 2019) with separate paths (Brenna et al., 2012, 2015). Additionally, Shin et al. (2012) interpreted the magnetic anomaly around JI and proposed that lithospheric folding beneath the island could generate basaltic magma, while Choi et al. (2001) proposed substantial interactions with the lithospheric structure of the magma from xenolith data.

Seismologically, the magmatic structures in the crust of JI have not been well-sampled. A shallow (<2 km) crustal shear wave velocity structure was first studied using a spatial autocorrelation (SPAC) method (Kim and Hong, 2012) and crustal thickness beneath JI was estimated from the inversion of receiver functions using data from permanent seismic stations on the island (Jeon et al., 2013). However, these studies were conducted over limited areas of JI due to the lack of available data.

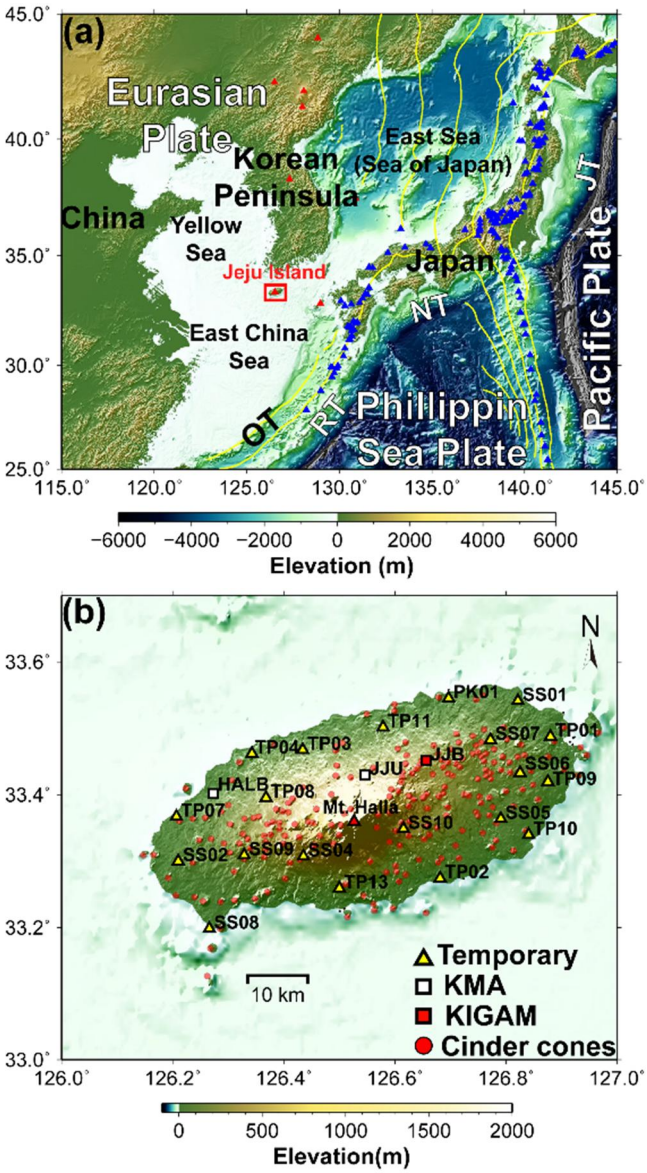

Figure 3.1. (a) Location and topographic map of the Jeju Island (JI) and the surrounding region. (b) Distribution of seismic stations and cinder cones on JI (*after* Song et al., 2018). Portable (yellow triangles) and permanent (white and red rectangles) broadband seismic stations are evenly distributed across the island. The yellow contour indicates the subduction depth of the Pacific Plate and Philippine Sea Plate. Abbreviations: OT, Okinawa Trough; RT, Ryukyu Trench; NT,

Nankai Trough; JT, Japan Trench. Red triangles indicate intraplate volcanoes, and blue triangles indicate arc-volcanoes.

3.2.2. Radial anisotropy in the volcanic field

Anisotropy observed in the crust is generally explained by a shape-preferred orientation (SPO) or crystallographic-preferred orientation (CPO). The former is generally caused by structures aligned to a specific direction (e.g., crack, fault, melt lenses, etc.), while the latter is related to mineral alignments due to sedimentation and deformation (Crampin, 1981, 1984, 1989; Shapiro et al., 2004; Meissner et al., 2006; Eilon et al., 2014; Ko and Jung, 2015; Jung, 2017; Almqvist and Mainprice, 2017; Kim and Jung, 2019; Russell et al., 2019). For volcanic structures, the radial anisotropy of shear wave velocities is used to identify magma-related structures (Leary et al., 1990; Crampin & Lovell, 1991; Shapiro et al., 2004; Meissner et al., 2006). Positive radial anisotropy ($V_{SH} > V_{SV}$) mainly originates from horizontally intruded structures (e.g.., sill or melt lenses), frozen lava flows, or pyroclastic deposits, while negative radial anisotropy ($V_{SV} > V_{SH}$) results from vertically oriented intrusions (e.g., dykes) and cracks. An effective way to measure radial anisotropy is through the comparison of Rayleigh (for V_{SV}) and Love (for V_{SH}) waves, particularly from ambient noise data (e.g., Shapiro et al., 2004; Huang et al., 2010; Moschetti et al., 2010; Guo et al., 2012, 2016). Consequently, measured radial anisotropy provides answers to questions related to the magma plumbing system, including how magma was supplied, what predominant direction of magma

intrusion was, and whether or not shallow chambers exist (Mordret et al., 2015; Jeddi et al., 2017; Godfrey et al., 2017; Benediktsdóttir et al., 2017; Lynner et al., 2018).

3.3. Data and Methods

3.3.1. Data

We used a comprehensive broadband dataset from temporary and permanent seismic stations. The temporary network was jointly operated by Seoul National University and Pukyong National University (Fig. 3.1). Three pilot stations were installed in advance from March of 2013, and 17 more stations were deployed over JI from September of 2013 to February of 2017. Locations of the pre-existing permanent stations (denoted as HALB, JJU, and JJB) were taken into account to design a more evenly distributed network. Many of the stations were located on relatively flat basaltic lava fields, except for five stations. Three of the stations in the east (SS05, SS06, and SS07) were at the top of cinder cones and two (SS04 and SS10) were installed on the slope of Mt. Halla. The altitude of the highest station was ~700 m, in contrast to the lowest station, which was located near sea level. All instruments for the temporary stations consist of homogeneous Nanometrics Trillium compact broadband sensors with Taurus digitizers

(Nanometrics, Inc., Canada). For analyses in this study, we used continuous, two-year, three-component data from 2014 to 2015, when continuous data from the 20 temporary stations were fully available.

3.3.2. Data processing and estimation of surface dispersion maps

We used well-established ambient noise cross-correlation methods to process our data and obtain surface wave dispersion curves (e.g., Bensen et al., 2007; Lin et al., 2008). Instrument response, mean values, and trends were removed from the three-component continuous waveforms, and divided by 1-hour-long time windows. Afterward, the windowed data were decimated to 1 Hz and band-pass filtered between 0.01-0.45 Hz. We applied one-bit time domain normalization and spectral whitening in the frequency domain. Lastly, cross-correlation functions were calculated for all available station-pairs and stacked. The transverse-transverse cross-correlogram of each station-pair was calculated by a linear combination of cross-correlograms between horizontal components (i.e., east-east, east-north, north-east, and north-north) (Lin et al., 2008). Finally, we obtained 253 cross-correlograms, which exhibited clear signals of Rayleigh and Love waves (Fig. 3.2).

To estimate group and phase velocities from the fundamental modes of Rayleigh and Love waves, a multi-filter analysis (e.g., Herrmann & Ammon, 2002; Yao et al., 2006) was applied to the obtained cross-correlograms. We automatically measured group and phase velocities using an iterative process. During the initial iteration, preliminary dispersion curves were estimated based on a reference curve calculated from a 1-D velocity model of the Korean Peninsula (Kim et al., 2011). Then, the mean of the previously measured dispersion curves of all station-pairs was used as a reference dispersion curve for the next time measurements. We repeated this process three more times to calculate the final dispersion curves (Fig. 3.3).

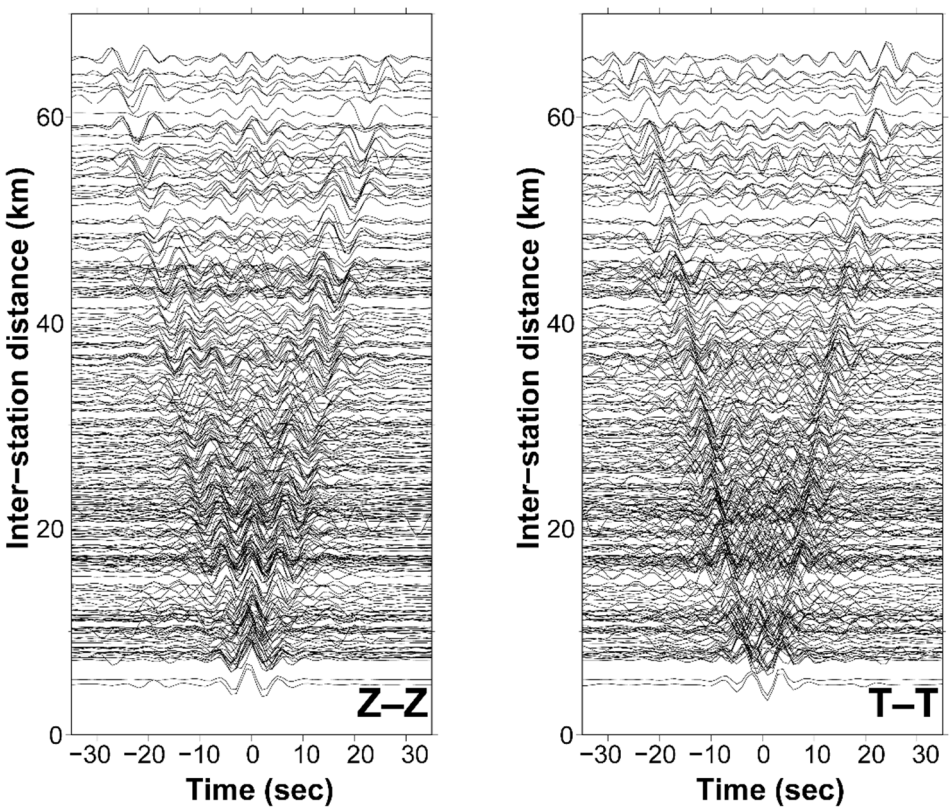

Figure 3.2. Calculated cross-correlation sections for (left) Z-Z and (right) T-T component pairs (top) and all possible station-pairs for cross-correlations (bottom). A 5-15-s bandpass filter was applied.

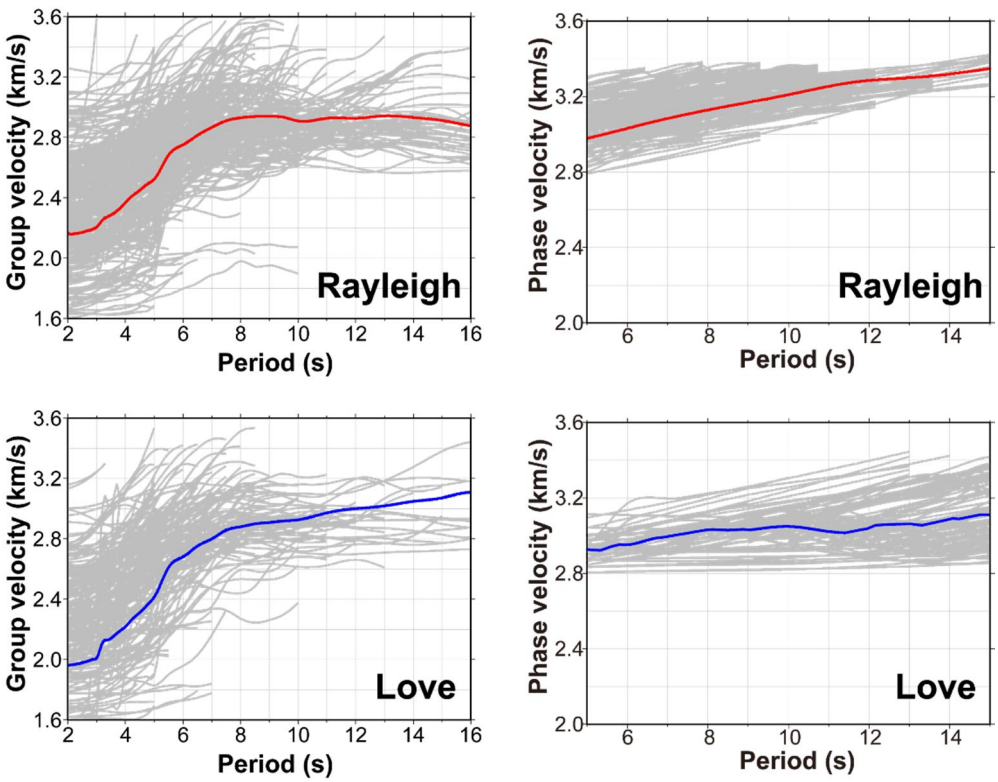

Figure 3.3. Group and phase velocity dispersions of Rayleigh and Love waves extracted from cross-correlations using the multi-filter technique of Herrmann & Ammon (2002).

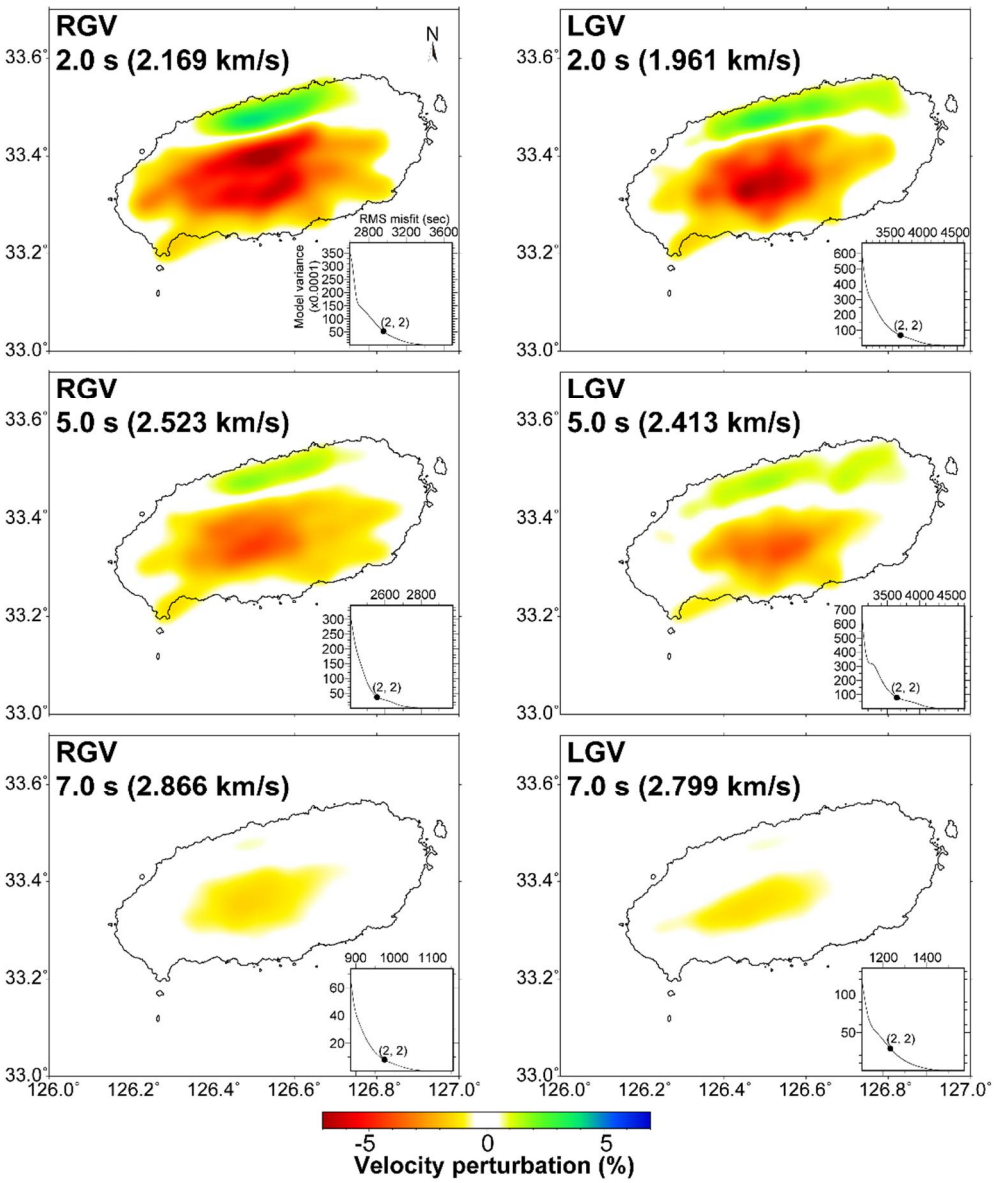

Figure 3.4. Examples of constructed Rayleigh wave group velocity (RGV) and Love wave group velocity (LGV) maps of JI for 2, 3, and 7 s. The trade-off curve and selected smoothing and damping parameters are also plotted in the lower right corner of each velocity map.

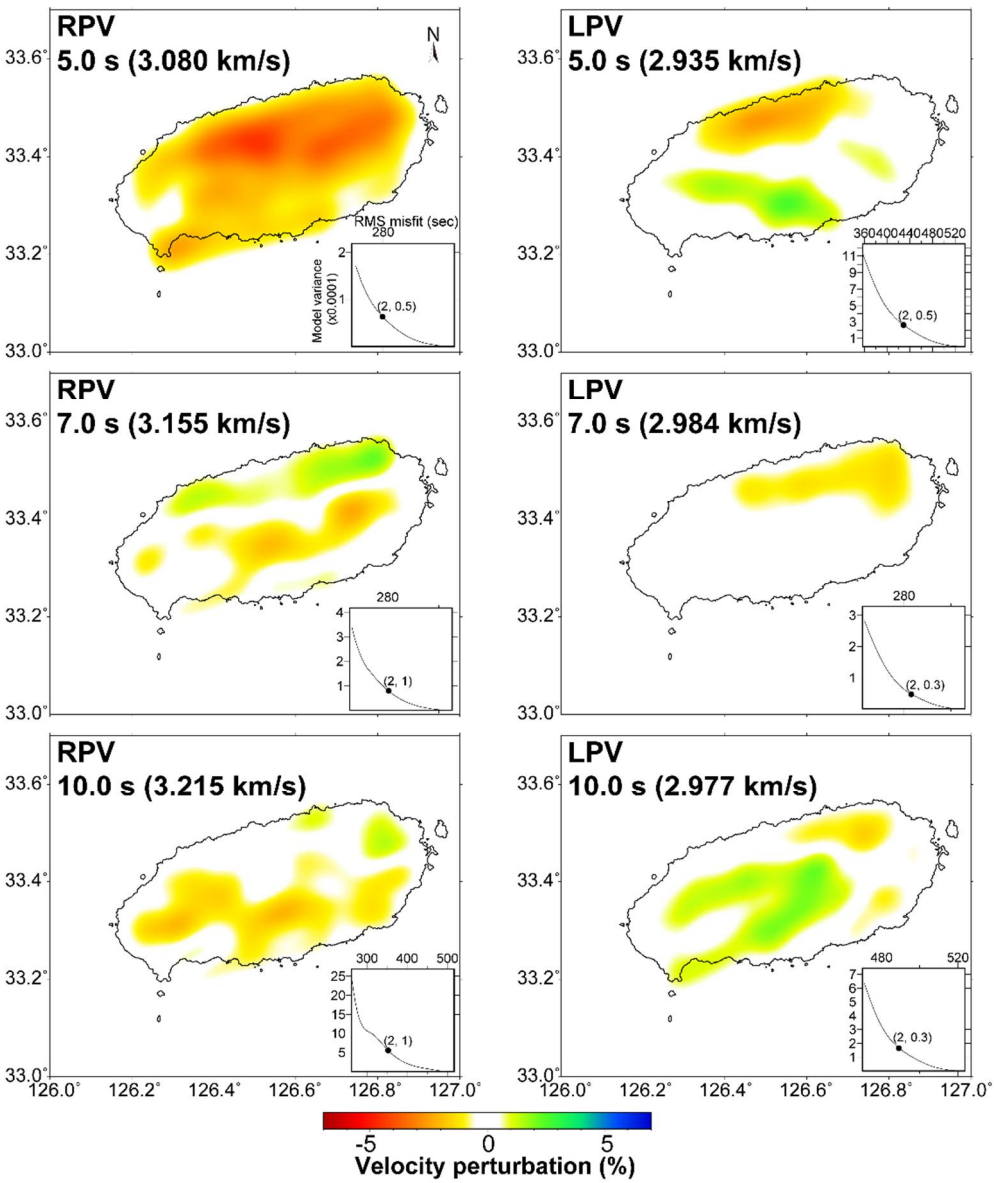

Figure 3.5. Examples of constructed Rayleigh and Love phase velocity (RPV and LPV, respectively) maps of JI for 5, 7, and 10 s. The trade-off curve and selected smoothing and damping parameters are also plotted in the lower right corner of each velocity map.

Spatial distributions of group and phase velocities in different wave periods were estimated using a nonlinear 2-D tomographic method, which combined a fast marching method and subspace inversion (Kennett et al., 1988; Rawlinson, 2005). We constructed 2-D group and phase velocity maps of Rayleigh and Love waves for a period between 2 and 15 s (Figs. 3.4 and 3.5). To account for the trade-offs between data misfit and model variance, we determined optimum sets of damping and smoothing values by selecting elbow-points in L-curve analyses (insets in Figs. 3.4 and 3.5).

3.3.3. Construction of a 3-D model from Bayesian joint inversions

To estimate 3-D isotropic and anisotropic velocity structures, a series of one-dimensional (1-D) inversions were performed for 461 nodes over a geographical grid spacing 0.02°. We used the previously established Bayesian inversion technique of Kim et al. (2017). This approach offered several particular advantages when applied to the data in this study. First, to estimate inversion parameter values, fully nonlinear Markov chain Monte Carlo (MCMC) sampling is used without assuming arbitrary constraints (e.g., initial models). Therefore, the density distributions of full probabilities for inversion parameters (i.e., posterior probability distribution or PPD) can be obtained, allowing us to estimate the uncertainties of the

resulting models. Through the MCMC sampling of probability densities, implementing simultaneous searches for multiple parameters (e.g., isotropic and radially anisotropic velocities in this study) in a layer is straightforward during the inversion process. The second advantage of using the inversion technique of Kim et al. (2017) is that with the hierarchical scheme in the method, different weightings are automatically imposed by searching for different noise levels in different types of data based on the information within the data. The level of noise in each type of data is a critical factor for determining the goodness of fit for a proposed model to the measured data. This is particularly useful for obtaining less biased results in joint inversions using several different types of data, in which arbitrary selected data weightings are often chosen in conventional joint inversions. Finally, the transdimensional scheme in the inversion process searches a set of optimum parameters (i.e., numbers of layers) to balance the trade-offs between model roughness and data misfit. Consequently, no damping or smoothing is required when using this technique. This method was used in each grid node with four different types of surface dispersion data, consisting of Rayleigh and Love wave group and phase velocity dispersions.

Four dispersion curves were composed via interpolation using dispersion velocity maps in periods ranging from 2–16 s and 5–15 s for group and phase velocities, respectively (Figs. 3.4 and 3.5). In

the Bayesian inversions, we used reasonably broad and flat distributions for the prior probabilities (or search ranges) of the inversion parameters: isotropic *Vs* (V_{ISO} = 0.5–5.0 km/s), *Vp/Vs* ratio = 1.5–2.0, radial anisotropy (ξ = −50–50%), interface depths (0–40 km), the number of layers (2–30), and the scaling factors for noise levels (−5.0–5.0). We defined the parameters for isotropic velocity as $V_{ISO} = (2V_{SV} + V_{SH})/3$ and radial anisotropy as $\xi = 100 * (V_{SH} - V_{ISO})/ V_{ISO}$. In each inversion, the Markov chain was run for 50,000 iterations and the first half were discarded to obtain converged samples from the latter half.

3.4. Results

3.4.1. Dispersion velocity maps

In Rayleigh wave group velocity (RGV) maps (Fig. 3.4), a low velocity anomaly was consistently observed in the center of JI, with a maximum amplitude of −7% in the short period maps (2–3–second period) and weaker for longer periods. Along the northern part of JI, a high−velocity anomaly was found with a perturbation of up to 4% faster than the average of each period. The pattern of velocity perturbations was maintained in the Love wave group velocity (LGV) maps (Fig. 3.4), which had slightly weaker amplitudes (6% and −3% average values for fast and slow anomalies, respectively) than the RGV maps. For the RPV and RGV

maps, the velocity anomalies were weaker than those of the group velocity maps (Fig. 3.5). Calculated sensitivity kernels (Fig. 3.6) showed that phase velocity data sampled deeper depths than group velocity data for the same wave period and provided more reliable estimates to at least 10 km, given the ranges of data periods used in our inversions (Fig. 3.6).

In order to evaluate the lateral resolution of the velocity maps (Figs. 3.4 and 3.5), we performed a series of checkerboard tests with velocity perturbations of ±5% in 0.08 ° x 0.08 ° checkers. The results (Fig. 3.7) showed that the input anomalies were generally well recovered, particularly for 5 s RGV and LGV maps, and 10 s RPV maps (Fig. 3.7). Since the velocity anomalies of the velocity maps were larger than 0.08° × 0.08°, it could be confirmed that the anomalies were undistorted, even considering the path coverage. However, the LPV result was distorted in the northeast-southwest direction over a 10 s period. This is due to the shape of the temporary network, which is installed along an elliptical shape across JI, and a smaller number of cross-correlograms used for LPV (~120) than for the RGV, LGV, and RPV maps (generally >200).

3.4.2. 1-D Bayesian inversions

Figure 3.8 shows an example of the 1-D inversion results for a

grid-point at the central volcano (Mt. Halla) (33.36° N, 126.52° E). The marginal PPDs of V_{ISO} and ξ show sharp changes at ~2 and ~5 km depths in a general trend wherein the velocity increases with depth (Fig. 3.8a). The marginal distribution of layer boundaries (Fig. 3.8a) confirms that higher probabilities were found at the corresponding depths. Though the PPDs provide credible ranges, we focus on the depth range of 1–10 km based on the calculated sensitivity kernels (Fig. 3.6) and resolution of the dispersion maps (Fig. 3.7).

It was noted that the depth sensitivity of the data was reasonably high at depths greater than 10 km; therefore, the interpreted depth range was a conservative choice to present the most reliable shallow magma structures. An interesting trend in most of inversion results was the layering of different anisotropic structures (e.g., Bodin et al., 2016) through a combination of strong negative radial anisotropy ($V_{SV} > V_{SH}$) at depths <2 km, strong positive radial anisotropy ($V_{SH} > V_{SV}$) from 2–5 km, and another negative value at depths >5 km. This pattern is reliable when the $\pm 2\sigma$ ranges of the marginal PPD for ξ are taken into account.

The marginal PPD for the number of layers (Fig. 3.8b) revealed that the inversion results comprised many different models with different numbers of layers, which fit both the Rayleigh and Love wave dispersion data (Fig. 3.8c). A test inversion assuming isotropic structures using the same data (Fig. 3.9) resulted in a

similar marginal distribution of isotropic shear wave velocity models and a good fit to RGV and RPV. However, the constrained inversion exhibited a poorer fit to LGV and LPV (Fig. 3.9c) than those in Figure 3.8(c) at shorter and longer periods in LGV and longer periods in LPV, which correspond to the highly anisotropic layers shown in Figure 3.8(a).

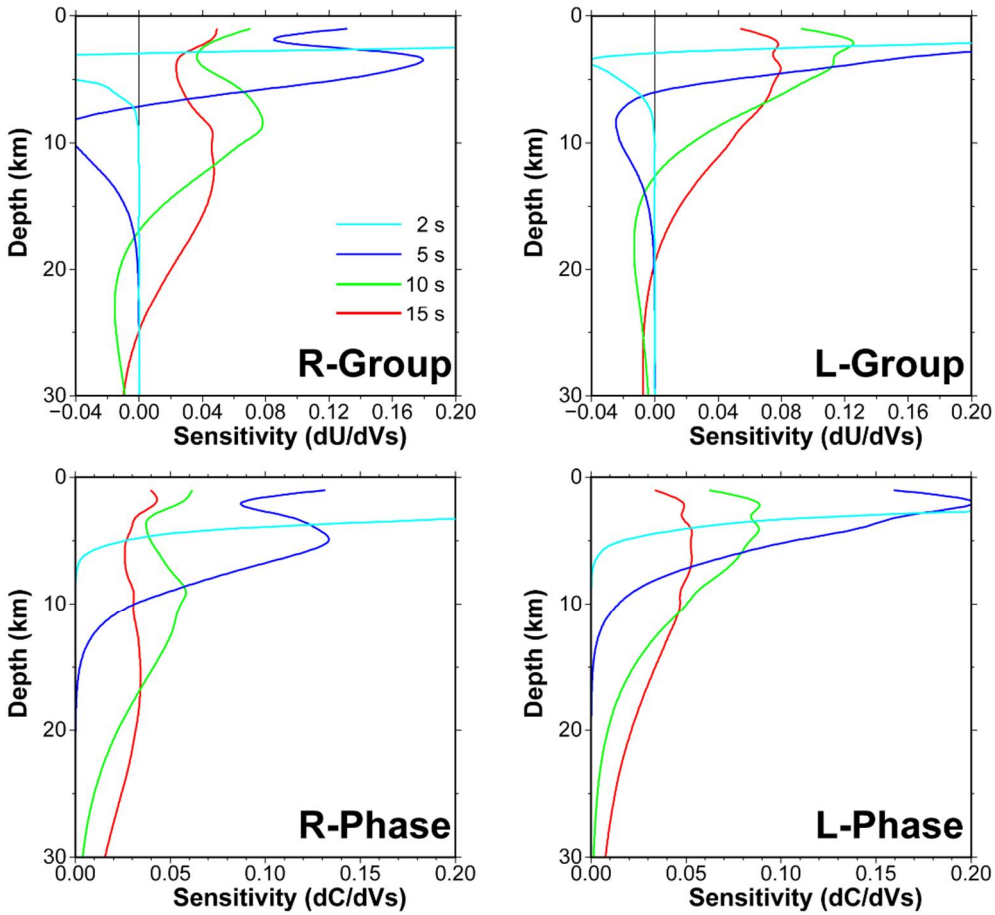

Figure 3.6. Sensitivity kernel at 2, 5, and 15 s using the 1-D average model of JI from the study of Kim et al. (2016b). The Rayleigh and Love wave group/phase velocities for periods of 2 and 15 s are sensitive to shear wave velocities at depths of up to 15 km.

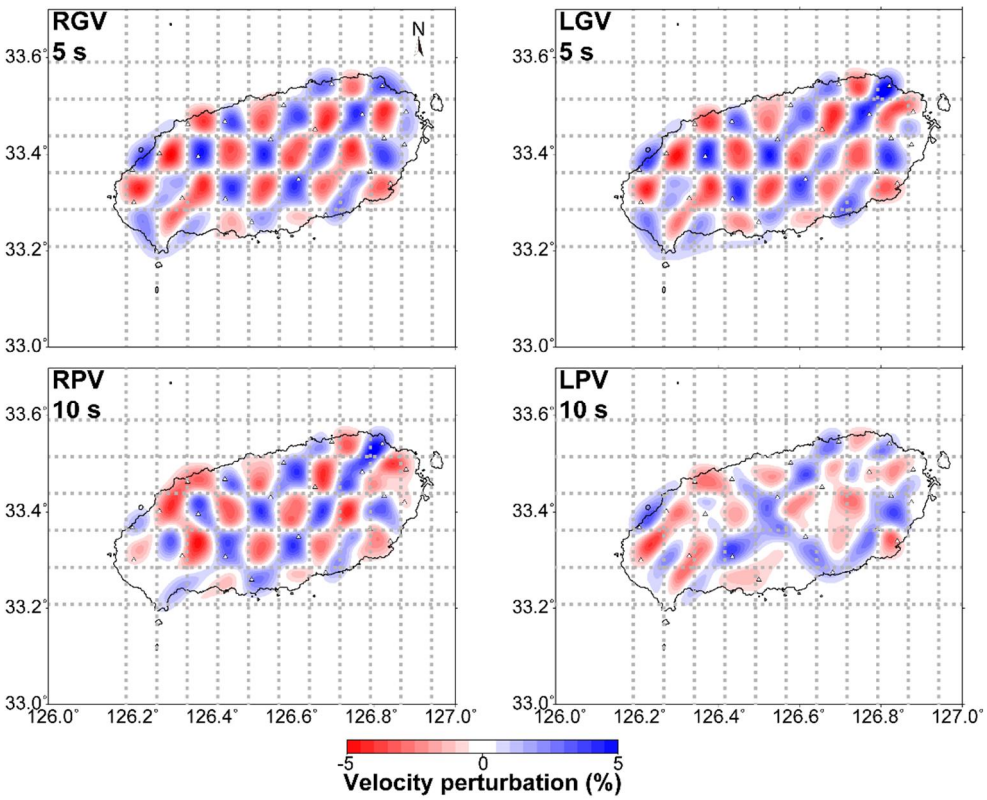

Figure 3.7. Checkerboard test results for RGV and LGV at 5 s and RPV and LPV at 10 s. A grid size of 0.08° x 0.08° (gray dashed line) was used in the calculations.

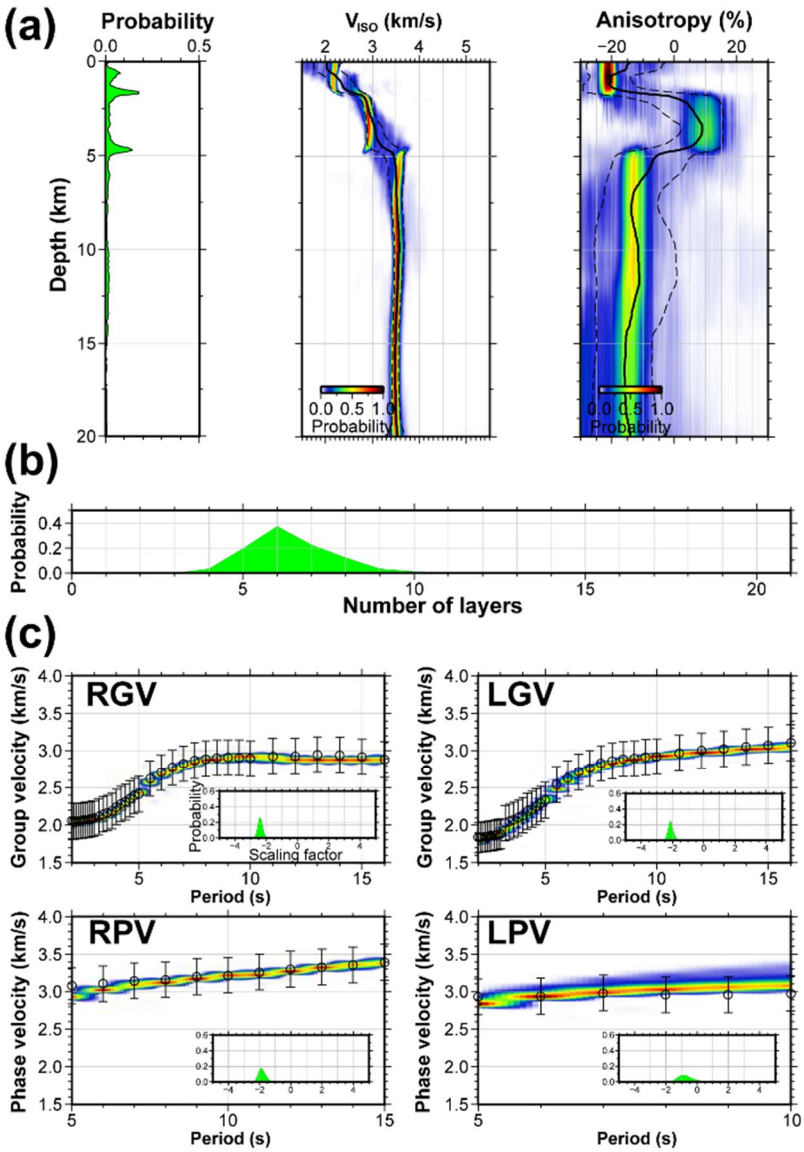

Figure 3.8. An example of a one-dimensional (1-D) shear velocity model with results of the Bayesian inversion using Rayleigh wave dispersions at 33.36° N, 126.52° E. Posterior probability distribution (PPD) of (a) layer boundaries, shear wave velocity, density, and anisotropy with depth, (b) the number of layers, and (c) the predicted synthetic data with the observed data. A total of four different types of dispersion data for Rayleigh and Love wave group velocities (period: 2–15 s) and Rayleigh and Love wave phase velocities from this study (period: 5–15 s) were jointly inverted using a hierarchical and transdimensional Bayesian technique.

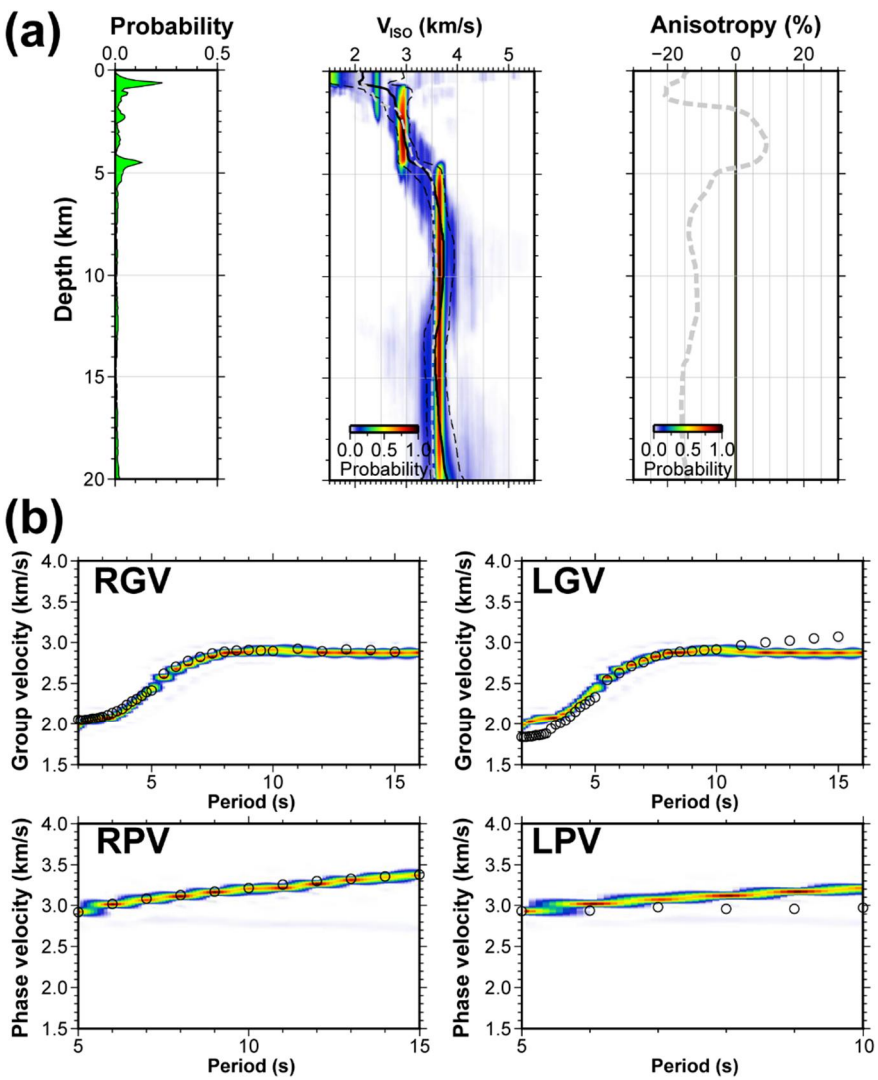

Figure 3.9. The same results as those shown in Figure 3.8, less the number of layers (Fig. 3.8b), but with isotropic inversion applied. Gray dashed lines represent the anisotropic inversion results shown in Figure 3.8.

3.4.3. Isotropic and anisotropic 3-D models

We constructed isotropic and radially anisotropic 3-D velocity structure models by integrating the results of the 1-D Bayesian inversions individually performed at 460 grid nodes (Figs. 3.10 and 3.11). In the V_{ISO} model (Fig. 3.10), a broad, low-velocity anomaly (lower than -8%) was found at 1.5 km beneath the central area in JI, including the Mt. Halla volcano (L_V1 in Fig. 3.11). Meanwhile, the northern coast exhibited a relatively high velocity anomaly (~3%). The pattern changed significantly from 2 km, where that all of JI exhibits normal velocities, with slightly higher (~2%) velocities around the central region (L_V2). At depth of ~4 km, low-velocity anomalies (lower than -4 km s^{-1}) were found within a limited area beneath the central volcano (L_V3). From depths greater than 5 km (L_V4), the variation in velocity was small, with a range from 1% to -2% to the mean value in this region (~3.48 km s^{-1}), which is slower than the mean upper-middle crustal velocity (~3.6 km/s) in the southern Korean Peninsula (Kim et al., 2011) and corresponds to the results from teleseismic tomography using body wave data in this region (Song et al., 2018).

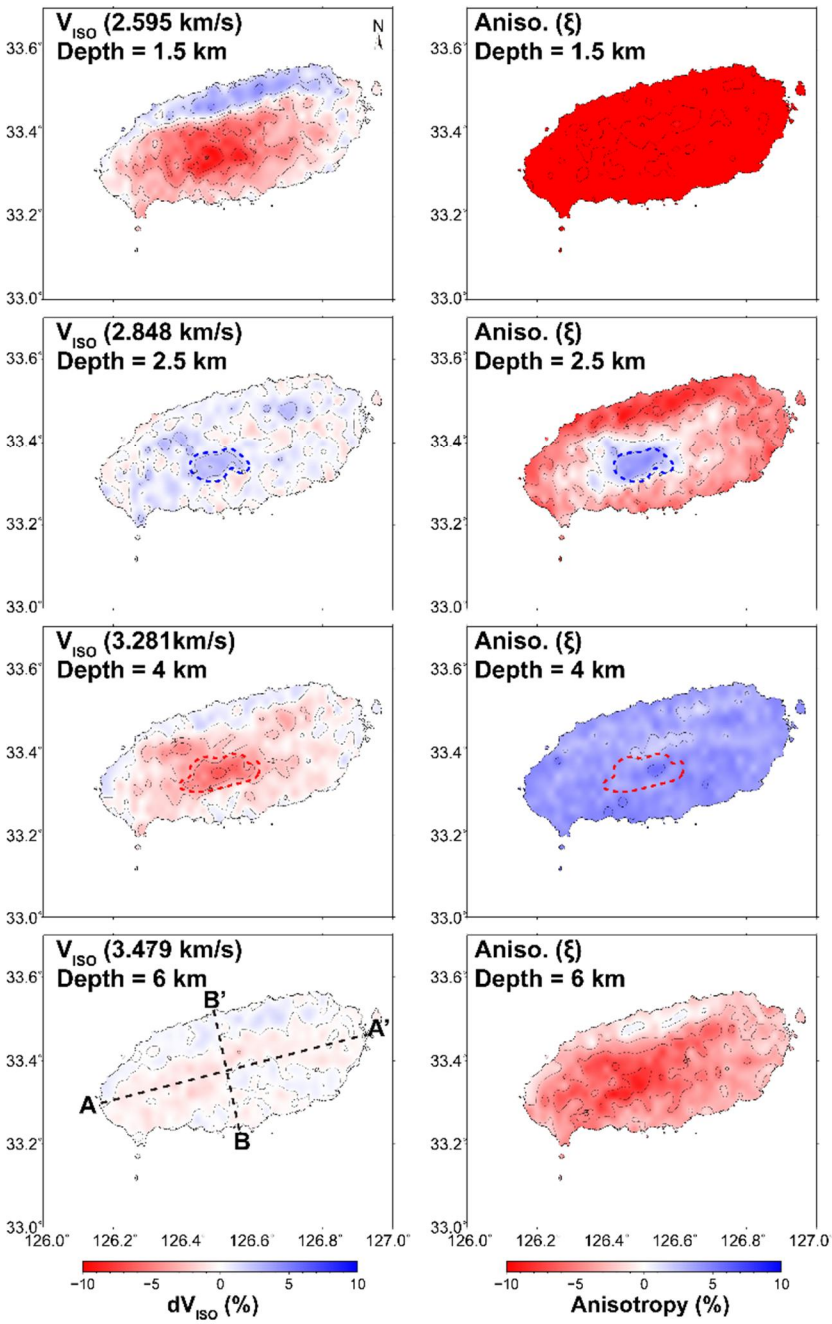

Figure 3.10. Horizontal slices of the 3−D V_{ISO} models and anisotropic models at depths of 1−6 km. Relative V_{ISO} was calculated based on the average of the V_{ISO} models for grids following the coastline. Contour lines show the second and third layers, as categorized from the patterns in the V_{ISO} and ξ models.

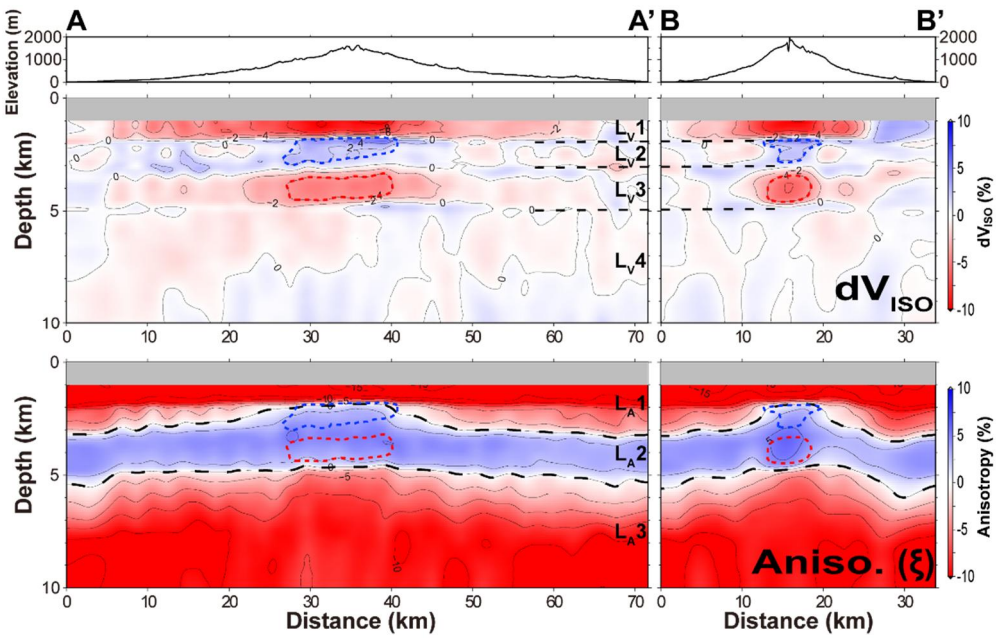

Figure 3.11. Vertical sections of the $V_{ISO} = (2V_{SV} + V_{SH}) / 3$ and anisotropy models following the A–A' and B–B' transects shown in Figure 3.10.

In the radial anisotropy model (Fig. 3.10), strong negative radial anisotropy ($\xi < -12.5\%$) was observed at shallow depths (<2 km) beneath the entire JI region (L_A1 in Fig. 3.11). In the same area but at deeper depths (>5 km), slightly weaker negative anisotropy (< ~7.5%, L_A3) was observed. In contrast, positive anisotropic structures were included at the depth range between 2– 5 km (L_A2). The horizontally fast structure was the thickest beneath the central volcano, with a thickness of 3 km, and the anisotropic structure thinned to 1.5 km toward the outside of JI. The thicker part corresponds to the region with large perturbations of isotropic velocities beneath the central volcano. Figure 3.11 shows vertical profiles of the V_{ISO} and ξ models along the long axis (A–A') and the short axis (B–B') of the ovoid JI (Fig. 3.10). By combining the patterns described in the V_{ISO} and ξ models, upper crustal structures beneath JI were identified and categorized into a structure with three layers over a basement, including:

1. A top layer down to 2 km with slow V_{ISO} (lower than −8%, L_V1) and strongly negative ξ (less than −12.5%, L_A1);
2. A second layer with positive ξ (>5%, central top of L_A2) and slightly fast V_{ISO} (2–4%, L_V2) at depths between 2 and 3 km, particularly beneath the central volcano and within areas of ~20 km and ~10 km along the major and minor axes of JI, respectively;

3. A third layer with the same magnitude of positive ξ (L_A2) and relatively slow V_{ISO} (lower than −4%, L_V3) in a similar area to the upper layer, but at depths between 3 and 5 km;
4. A vertically fast basement (ξ > 7.5%, L_A3) with generally neutral V_{ISO} over across JI (L_V4).

It is notable that the pattern changes moving away from the center of JI. The structure with the first positive ξ becomes thinner, and thus is located at the depth corresponding to the third layer (3–5 km, L_V3), with more neutral isotropic velocities at all depth ranges except for the top layer.

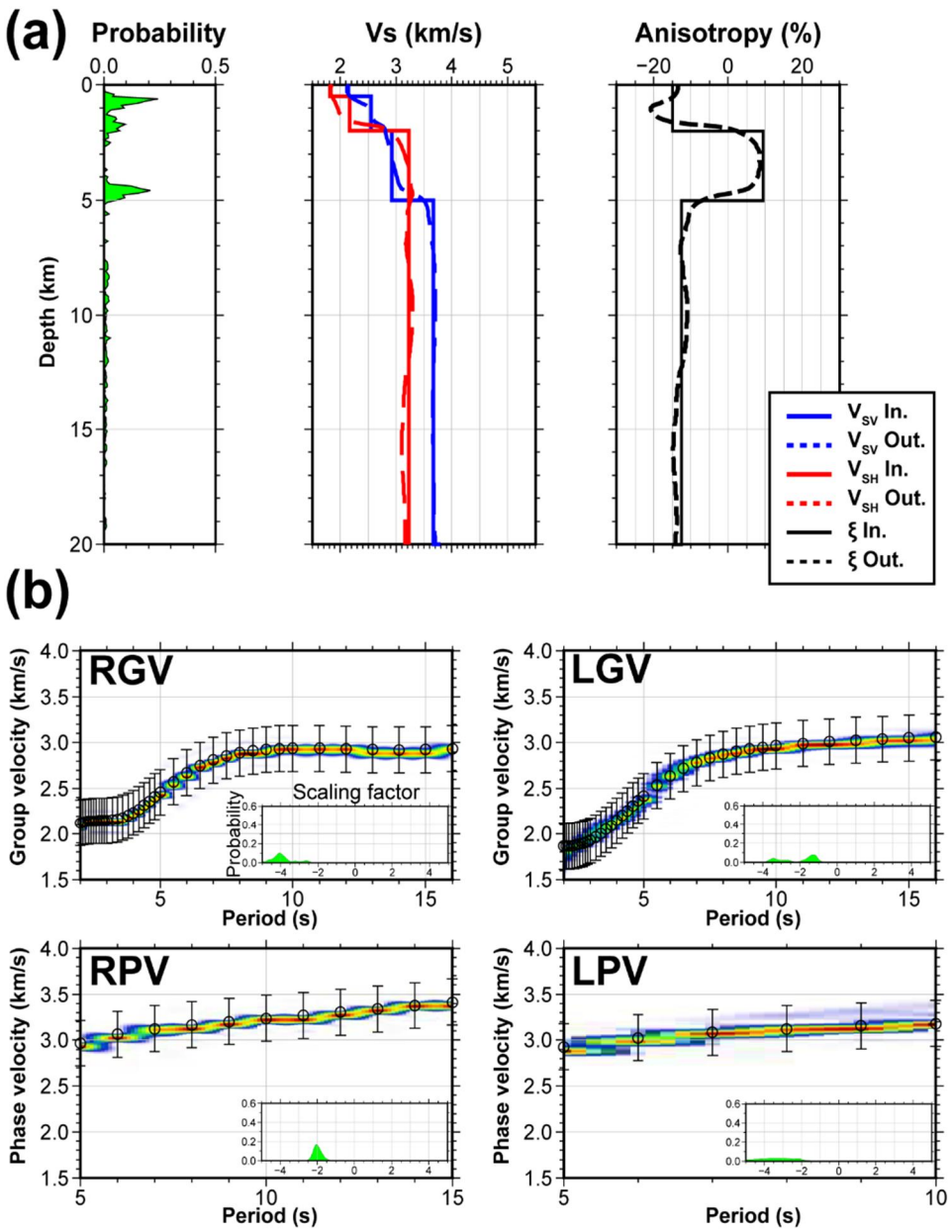

Figure 3.12. (a) Synthetic results of 1-D shear velocity and anisotropy models. Rayleigh and Love dispersion curves were calculated using input V_{SV}, V_{SH}, and anisotropy models (red, blue, and black solid lines, respectively) similar to those observed in the center of Mt. Halla. The V_{SV}, V_{SH}, and radial anisotropy models were inverted following our inversion scheme. (b) Posterior distributions of predicted synthetic data with the observed data.

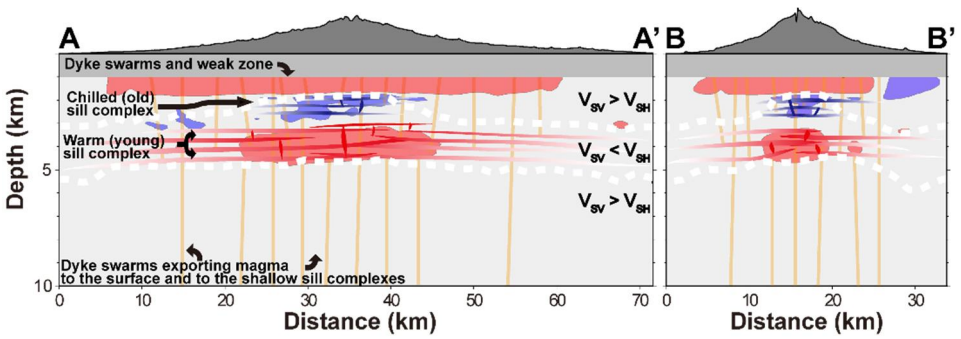

Figure 3.13. Model of the magma plumbing system of JI. Blue and red shaded zones with gray dashed lines represent the ± 2% isosurfaces of the relative isotopic model, and white dashed lines show the boundaries of anisotropic changes.

3.5. Discussion

Jeju Island exhibits significant topographic variation from sea level to 1.95 km at the top of Mt. Halla, all within a limited ovoid area of approximately 75 km x 32 km. In this study, we assumed a flat surface to estimate the distribution maps of surface wave dispersion velocities and the final 3-D models, similarly to the assumptions made in previous studies (Jaxybulatov et al., 2014; Jeddi et al., 2017; Benediktsdóttir et al., 2017). This is due to the fact that the propagation of surface waves along uneven surfaces is complex, difficult to understand, and dependent upon wave periods, in contrast to studies using the rays of body waves. Instead, we estimated the effect of topography on the dispersion measurements for two extreme cases, as similar tests have been previously performed (Jaxybulatov et al., 2014; Jeddi et al., 2017; Benediktsdóttir et al., 2017). We estimated differences in the dispersion velocity for the station-pair with the longest interstation distance (65 km) and a large elevational gradient (1.9 km) (stations SS02 and TP01), as well as for the pair with the highest altitude difference (~1 km) to the interstation distance (17 km) (stations SS04 and JJU) (Fig. 3.1). Simple calculations assuming rays propagating along the surface without accounting for frequency effects showed that the possible velocity uncertainties due to topography were 0.2% and 0.7% for the former and latter pairs, respectively (Jaxybulatov et al., 2014; Jeddi et al., 2017;

Benediktsdóttir et al., 2017). These uncertainties are insignificant considering the velocity perturbations in the dispersion maps (Figs. 3.4 and 3.5) and variances in data, which were ~15–20% of the mean dispersion curves (Fig. 3.3). In particular, much larger variations in velocity (>5%), compared to the estimated uncertainties, were consistently estimated in all of the shortest period maps (2–s maps in Figs. 3.4 and 3.5), which are the most sensitive periods to topographical variation.

As a way to verify our inversion results with strong radial anisotropy (Fig 3.8), we conducted a recovery test using synthetically generated data. To calculate synthetic RGV, RPV, LGV, and LPV dispersion curves, we used V_{ISO} and ξ models at the top of Mt. Halla (Fig. 3.8) and simplified them to have three layers over a half–space (Fig. 3.12). Notably, the third layer exhibited abruptly large and positive radial anisotropy (10%) from the dominantly negative background of radial anisotropy (Fig. 3.12). Residual errors between the observed and modeled data in Figure 3.8 were applied as data error to the calculated synthetic dispersion curves. The inversion results from the synthetic data showed that the input anomalies were well recovered in both isotropic and radial anisotropic models (Fig. 3.12).

The shallowest layer (<2km) had relatively slow isotropic structures with vertically fast anisotropy (L_V1 and L_A1 in Fig. 3.11) at the central and southern part of JI (Fig. 3.10). The surface

geology and data from a drilling survey indicate that JI has generally thick sedimentary structures (~2 km), which have mainly been formed by hydrovolcanic eruptions and pyroclastic depositions (Koh et al., 2013; Yoon et al., 2014). In general, such horizontal layering of deposited materials results in positive radial anisotropy due to both CPOs and SPOs, as reported in several previous studies (e.g., Shapiro et al., 2004; Meissner et al., 2006; Ko and Jung, 2015; Jung, 2017; Almqvist and Mainprice, 2017). Massive lava flows along a gentle slope also cause positive anisotropy (e.g., Mordret et al., 2015). The observations on JI are inconsistent with the surface features. Similar negative anisotropy has been reported in volcanoes dominated by vertically aligned SPOs (e.g., Spica et al., 2017; Lynner et al., 2018). Spica et al. (2017) showed that negative radial anisotropy was dominant within a low-velocity layer at the central part of the Colima volcano, with a dyke swarm above a shallow magma chamber. Vertically developed crustal magma plumbing systems have also been detected with negative anisotropy (Lynner et al., 2018).

It has been known that JI and the volcanic bodies in it were formed by the overlap of more than 400 scattered small cones from laterally distributed magma plumbing structures (Park et al., 2008; Shin et al., 2012; Koh et al., 2013; Brenna et al., 2015; Song et al., 2018). Our observations from the top layer correspond to previous results that suggested that a vertically aligned SPO, due to highly

developed dyke swarms (Fig. 3.13) over most of JI, could play a major role in producing the negatively anisotropic structures, which are similar to many other regions worldwide (Jaxybulatov et al., 2014; Tibaldi, 2015; Spica et al., 2017; Lynner et al., 2018; Çakır, 2018). Volcanic activities forming the central vent (Mt. Halla) were episodic within limited time periods during the continuous and small-scaled monogenic volcanism via ubiquitous cones (Brenna et al., 2012; Koh et al., 2013; Yoon et al., 2014; Brenna et al., 2015). Therefore, the formation of the shallow volcano-sedimentary structures may have been less affected by the central eruptions, but rather by the more heterogeneous deposition filling in gaps between cones, which resulted in weaker horizontally fast anisotropy than distributed and vertically aligned structures (i.e., dyke swarms).

In the second and third layers (2–5 km), the pattern of radial anisotropy changed from negative to strongly positive (greater than ~5%) (Fig. 3.10 and L_A2 in Fig. 3.11). At upper crustal depths, the alignment of fluid-saturated microfissures (i.e., SPO) is the primary origin of anisotropy (Okaya et al., 1995). To produce positive radial anisotropy, the presence of laterally elongated cracks is necessary, along with an alignment of regional tectonic stress fields (e.g., Guo et al., 2012). Specifically, in volcanic fields, such structures could be formed by cooled and fluid-filled melt lenses, sills, or layered magma stores (Shapiro et al., 2004; Meissner et al., 2006; Jaxybulatov et al., 2014; Spica et al., 2017;

Lynner et al., 2018; Jiang et al., 2018). The formation of these volcanic structures has been commonly understood as resulting from changes in vertical volume (e.g., caldera collapse) (Masterlark et al., 2010; Jaxybulatov et al., 2014; Cashman & Giordano, 2014; Ward et al., 2014; Jeddi et al., 2017; Benediktsdóttir et al., 2017). More generally, recent studies have shown that the horizontal magma transportation at shallow depths in volcanic fields is strongly controlled by the applied stress related to topographic loading, faults, and heterogeneities in local stress fields (Ishizuka et al., 2008; Tibaldi et al., 2015; González et al., 2013).

Horizontally elongated magma structures at upper crustal depths have been reported in various volcanic regions (Ishizuka et al., 2008; Spica et al., 2017; Çakır, 2018; Lynner et al., 2018). All of these regions have shown highly similar patterns to the anisotropic structure in this study, with embedded and horizontally layered magma structures at a middle depth between the vertically aligned structures above and below. Ishizuka et al. (2008) reported structures of laterally transported magma over 30 km at 5 km depth below the Hachijo Nishiyama volcano. They explained that the structure was formed by vertical pressures from the loading of the overlying rock mass and the upward pushing of magma from bottom plumbing structures. Çakır (2018) imaged a similar scale positive anisotropy (> 10%) at shallow crustal depths beneath the Aegean region within negative radially anisotropic ambient structures. They

specified the lateral structure as a sill (or small-scale horizontally elongated magma chamber) complex in a predominantly extensional tectonic setting. In extensional regimes, similar sill intrusions are developed at deeper depths (Spica et al., 2017; Lynner et al., 2018).

It has been suggested that volcanism was less focused on the central vent, and thus no large caldera formed on JI (Brenna et al., 2012, 2015). The primary stress regime (Shin et al., 2012) was extensional during the period of JI volcanism, which occurred in a back-arc setting due to the subduction of the Philippine Sea Plate (Brenna et al., 2015; Kim et al., 2016). Together with the striking similarity in the patterns of layered horizontally and vertically aligned magma structures beneath different volcanoes, the features of magma structures below JI indicate that the layer with positive radial anisotropy at a depth of 2–5 km likely consists of intrusive sills fed by scattered cones and the central volcano.

Overlapping with the isotropic velocity distribution, the horizontally fast anisotropic structure at the middle depth of 2–5 km was divided into two parts, with faster and slower isotropic velocities (the second and third layer, respectively) below the central volcano and over a limited volume of 600 km^3 (L_V2 and L_V3 in Fig. 3.11). The perturbation of shear waves can be caused by many factors, including thermal variations, a compositional dichotomy, and the existence of fluids or melts (Artemieva et al., 2004; Dalton et al., 2009; Cammarano et al., 2011). Separation and

focusing of crustal fluids is less likely to occur in a limited part of highly developed sill complexes. Additionally, the relatively small reduction in velocity (up to −4%) and lack of current volcanism at the surface rule out the existence of melted materials.

Compositional variation might be caused by magma separation within a magma structure via fractional crystallization, resulting in the faster, more mafic upper layer overlying the slower felsic layer (Shervais et al., 2006; Ishizuka et al., 2008). However, in the case of JI, it is difficult to explain the upward deposition of crystallized mafic materials and the consistent horizontally fast direction of both sides with different compositions. Therefore, it is more reasonable to interpret these structures in terms of thermal variations. Differences in cooling time present a plausible explanation for the temperature variation in the same sill texture. In the case of simultaneous injections of magma and the formation of a sill structure, cooling speeds will change with depth, which could control the variation in velocity. However, the sharp transition in isotropic velocity is more favorable to a time lag between the formation of the upper and lower layers. The second layer may have been formed first, before the third layer, in the same setting that produced similar sill structures. Many similar structures have been reported in volcanic systems with multiple layers of sill-like magma accumulations in the shallow crust (e.g., Cervelli & Miklius, 2003; Peltier et al., 2009; Chadwick et al., 2011; Baker & Amelung,

2012; Bagnardi & Amelung, 2012.).

Regional horizons of neutral buoyancy, magma supply rates, and thermomechanical structure in the crust control the depth distribution of multiple small magma chambers (Clague and Dixon, 2000; Hildner et al. 2012; González et al., 2013; Edmonds et al., 2019). Based on the magma supply rate on JI (~0.0003 km^3/yr), volcanoes on Réunion and in the Galápagos are particularly similar to JI, with extensive distributions of sill-like chambers at 2-7 km depths (Edmonds et al., 2019). Though there is no clear evidence of focusing for volcanic activities on the central volcano, the contrast in the thickness of the laterally fast anisotropic layer between this area and the surrounding regions shows that magma supplies to the central volcano lasted longer. While speculative, the formation of the third layer by sill intrusions could have pushed up the second layer, building a high-topography central volcano (Archer et al., 2005; McLean et al., 2017). Compared to the surrounding small monogenic cones, this would correspond to episodic eruptions with larger volumes of magma (Brenna et al., 2012; Koh et al., 2013; Yoon et al., 2014; Brenna et al., 2015).

Song et al. (2018) showed that magma on JI originated from the sublithospheric upper mantle interacting intensely with the lithosphere to form broadly distributed magma structures in the deeper crust. The basement, with its negative radial anisotropy, is explained as the magma plumbing system connecting from the deep

source to the structures in the shallow crust (L_V4 and L_A3 in Fig. 3.11). A setting within the deeper crustal dyke structures and shallow sill layers of diverse scales has often been reported in many volcanoes (e.g., Mordret et al., 2015; Tibaldi, 2015; Spica et al., 2017; Godfrey et al., 2017; Lynner et al., 2018; Çakır, 2018). Depending upon the flux of magma and the level of ambient stress, this type of vertical plumbing system consists of a few large dykes or many smaller but more widely distributed dyke systems. Together with the monogenic and randomly distributed eruptions over time and space, the more homogeneous and vertically fast anisotropy indicates the latter structure is more plausible (Brenna et al., 2012; Yoon et al., 2014; Brenna et al., 2015; Mordret et al., 2015; Spica et al., 2017; Godfrey et al., 2017; Lynner et al., 2018; Çakır, 2018).

3.6. Conclusions

In this study, we constructed 3-D V_{ISO} and ξ models of JI, an isolated intraplate volcano located offshore of the southeastern Korean Peninsula, by applying hierarchical and transdimensional Bayesian inversions with temporary seismic network data. The 3-D V_{ISO} and ξ models of JI show that various types of plumbing systems exist in the upper crust. A top layer that extends down to 2 km with slow V_{ISO} and strongly negative ξ (L_V1 and L_A1) could

represent vertically aligned SPOs due to the highly developed dyke swarms related to the scattered small cones over most of JI. The second and third layers with positive ξ (L_A2) may be interpreted as multiple layers of sill-like magma accumulation in the shallow crust, while there is central thermal variation between the two layers (L_V2 and L_V3) due to episodic eruptions with larger volumes of magma and differences in cooling time. Moving away from the center of JI, these central velocity anomalies decrease and the structure with firstly positive ξ values becomes thinner. The vertically fast basement (ξ, L_A3), with generally neutral V_{ISO} and where average upper-middle crustal velocities are slower than those of the southern Korean Peninsula, over the entire JI (L_V4) is explained as the magma plumbing system connecting from the deep source reported from the results of a previous teleseismic tomography study that used body wave data on JI. These characteristic plumbing systems have supplied various types of magma from deeper sources and have been involved in complex and episodic eruptions, which ultimately formed JI.

Chapter 4

Imaging the anisotropic upper mantle structure beneath northeast Asia from Bayesian inversions of ambient noise data

4.1. Introduction

The seismic radial anisotropy in the scale of the upper mantle is mainly due to the lattice preferred orientation (LPO) caused by the relative motion of the mantle convection and plate (Montagner, 1998; Karato et al., 2008; Long and Becker, 2010; Mainprice, 2010; Eilon et al., 2014; Russell et al., 2019). In addition, the remaining fossilized fabric in the lithosphere from past tectonic activities (e.g., extension) can cause the radial anisotropy (Ekström and Dziewonski, 1998; Debayle and Kennett, 2000; Beghein et al., 2014; Russell et al., 2019). Positive radial anisotropy (the horizontally polarized shear wave (V_{SH}) is faster than the vertically polarized shear wave (V_{SV})) is generally observed in the upper asthenosphere because of the dominant mantle flow (Kawakatsu et al., 2009; Yuan and Romanowicz, 2010; Carlo Doglioni and Giuliano Panza, 2015). This positive radial anisotropy in the asthenosphere can be weakened by mantle upwelling, and convection and thermal heterogeneities (Eilon et al., 2014; Alder et al., 2017; Isse et al., 2019). As the radial anisotropy contains information of the tectonic history and present state of the mantle, it can be key to understanding the complex tectonic dynamics in the scale of the mantle (Fouch and Rondenay, 2006; Maggi et al., 2006). The northeast Asia (NEA) region has experienced various tectonic events affected by the collision of the Indo-Australian plates and

the subduction of the Pacific and Philippine Sea plates (Wei et al., 2012; Liu et al., 2017). The result of tectonic processes remains on the surface in the form of extensional basins, and intraplate and arc volcanism, etc. (Shin et al., 2012; Liu et al., 2017; Van Horne et al., 2017; Zhang et al., 2018). In particular, the East Sea (ES) experienced a back-arc extension from the Early Oligocene (~32 Ma) to about 15 Ma (Tamaki, 1988; Chough et al., 2000). Three major extended basins (Japan, Yamato, and Ulleung) and topographic highs (e.g., unrifted continental crust, volcanic island) are scattered in the ES with complex topography. Previous studies have confirmed the presence of strong low-velocity anomalies beneath the ES (Simutė et al., 2016; Ma et al., 2019). A number of intraplate volcanoes (e.g., Mt. Baekdu or Changbi) are located along the western boundary of strong low-velocity anomalies (Kim et al., 2016; Kim et al., 2017; Ma et al., 2019). Kim et al. (2016) suggested that these intraplate volcanoes could be associated with the interaction between preexisting continental lithosphere and back-arc processes beneath the ES (e.g., edge-driven upwelling).

In this study, we developed a radial anisotropy model for the ES and surrounding region to understand the complex tectonic history of these regions and to clarify relationships between the dominant low-velocity anomalies and the surrounding intraplate volcanoes. Using the horizontal component waveform data of broadband stations installed in NEA, we calculated Love-wave group and

phase-velocity dispersion maps for the ES and surrounding region. Then, to obtain anisotropic shear wave velocity models, the Rayleigh wave group/phase dispersion data from Kim et al. (2016) and dispersion data from the global model (Ekstrom, 2011) were inverted together with the Love wave dispersion data of this study up to the depth of the upper mantle (~160 km). Through this inversion, we were able to construct three-dimensional (3-D) radial anisotropic models that could help to understand the tectonic process of the opening and the intraplate volcanism in the upper mantle beneath the ES and surrounding regions.

4.2. Data and Methods

We used three-component continuous broad-band seismic data from January 2010 to December 2011, which were recorded at 31 stations from the Korea Institute of Geoscience and Mineral Resources (KIGAM) and Korea Meteorological Administration (KMA), 84 stations from the F-net broadband seismograph network operated by the National Research Institute for Earth Science and Disaster Prevention (NIED), and 129 stations from the northeast China Extended Seismic Array (NECESSArray) (Fig. 4.1).

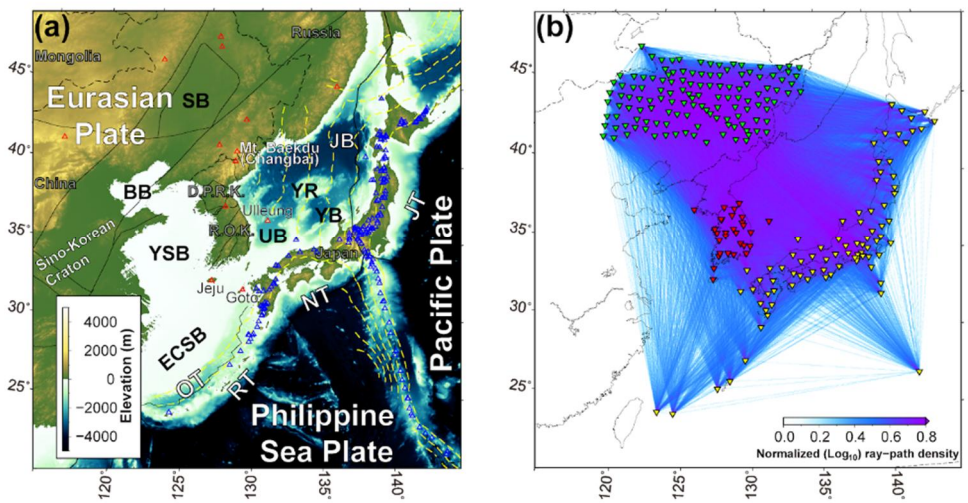

Figure 4.1. (a) Topographic map of the Northeast Asia region. The yellow contour indicates subduction depth of the Pacific plate and Philippine Sea plate. Features: SB, Songliao Basin; BB, Bohaiwan Basin; YSB, Yellow Sea Basin; ECSB, East China Sea Basin; UB, Ulleung Basin; JB, Japan Basin; YB, Yamato Basin; YR, Yamato Rise; RT, Ryukyu Trench; OT, Okinawa Trough; NT, Nankai Trough; JT, Japan Trench; Red triangles: intraplate volcanoes; Blue triangles: arc volcanoes. (b) All possible station pairs for cross-correlations. Receiver locations are shown by triangles for the following networks used in this study: F-net (yellow), KIGAM and KMA (red), and NECESSArray (green) stations.

A conventional preprocess for the ambient noise cross-correlation was applied (Bensen et al., 2007). The three-component data from each station were divided into one-day windows and the instrument response, mean, and trend were removed. In order to reduce a signal with a large amplitude such as an earthquake signal, a band-pass filter of 0.01-0.45 Hz and then frequency-time normalization were applied. In addition, spectral whitening was performed by dividing the frequency domain into 40 equal parts and then dividing each section with its average. Cross-correlograms between the horizontal components (East-East, East-North, North-East, and North-North) were calculated and stacked for the entire period. Then, transverse-transverse (T-T) cross-correlograms were calculated by rotating cross-correlograms of the horizontal components in a linear combination with coefficients from azimuth and backazimuth information between stations (Lin et al., 2008). In addition, orientation corrections were performed for each station pair to obtain accurate cross-correlograms of the T-T components. The orientation error of each station was estimated by using the characteristics of the surface wave that there should be a 90° phase difference between the Rayleigh wave's vertical and radial components (van Wijk et al., 2011; Zha et al., 2013). The Hilbert-transformed vertical-vertical (Z-Z) cross-correlogram was compared to the radial-vertical (R-Z) cross-correlogram to find the corrected angle with the greatest variance reduction, and

the orientation correction was applied for horizontal components of each station (Zha et al., 2013; Lee and Rhie, 2015).

We basically used one side lag of the cross-correlograms. The ambient noise cross-correlograms for the NEA region were known to contain the signal of Aso volcanic activity at a period of 8-30 s (Zheng et al., 2011; Lee et al., 2015; Kim et al., 2016). As we know the location of the station pairs and the Aso volcano, we can predict whether the Aso volcanic signal will appear in the positive or negative lag of the cross-correlograms (Zheng et al., 2011; Kim et al., 2016). Therefore, we used a negative lag of the cross-correlogram for the station pairs where the signal from the Aso volcano was expected to appear in a positive lag.

The multiple filter technique was applied to cross-correlograms to extract dispersion curves of the Love wave group and phase velocity (Herrmann and Ammon, 2002; Yao et al., 2006). First, based on the dispersion curve calculated from the ak135 model (Kennett et al. 1995), the group and phase velocity of the Love wave were automatically measured using frequency-time analysis (FTAN) diagrams for each station pair. The average of the entire dispersion curves was set as a new reference curve. Then, the automatic measurement was repeated, and extracted dispersion curves were set as a reference curve for the next time measurement. The final dispersion curves were determined by

repeating the automatic measurement three times. Dispersion maps for the Love wave group and phase velocity in different wave periods were constructed using a nonlinear 2-D tomographic method, which combined a fast-marching method and subspace inversion (Kennett et al., 1988; Rawlinson, 2005). We constructed 2-D group and phase velocity maps of Love waves for a period between 8 and 65 s (Fig. 4.2). The optimum set of damping and smoothing values for each period was selected from elbow-points in the trade-off curves of data misfit and model variance.

To construct a 3-D anisotropic (ξ) model, a series of one-dimensional (1-D) inversions were performed for 609 nodes (Kim et al., 2016; Kim et al., 2017). We used the Bayesian inversion technique of Kim et al. (2017). A total of eight different types of dispersion maps of Love waves from this study (period 8-60 s), Rayleigh waves from a previous tomographic study (Kim et al., 2016; period 8-60 s), and longer period data (period 70-120 s) from a global model (Ekstrom, 2011) were inverted together to estimate 1-D radial anisotropy models. In the Bayesian inversions, we used reasonably broad and flat distributions for the prior probabilities (or search ranges) of the inversion parameters: Vs ($0.5 \leq Vs \leq 5.5$ km/s), Vp/Vs ratio ($1.5 \leq Vp/Vs \leq 2.0$), radial anisotropy ($0.1 \leq \xi \leq 1.9$), interface depths (up to 250 km), number of layers (between 1 and 20), and scaling factors (between -7.0 and 7.0). In the inversion process, there were no other

regularizations than parameter configurations. A total of 200,000 iterations were carried out, and the first 100,000 were discarded. In addition, the model complexity (i.e., the number of layers) and the degree of data fitting (i.e., the level of data errors) were considered at the same time.

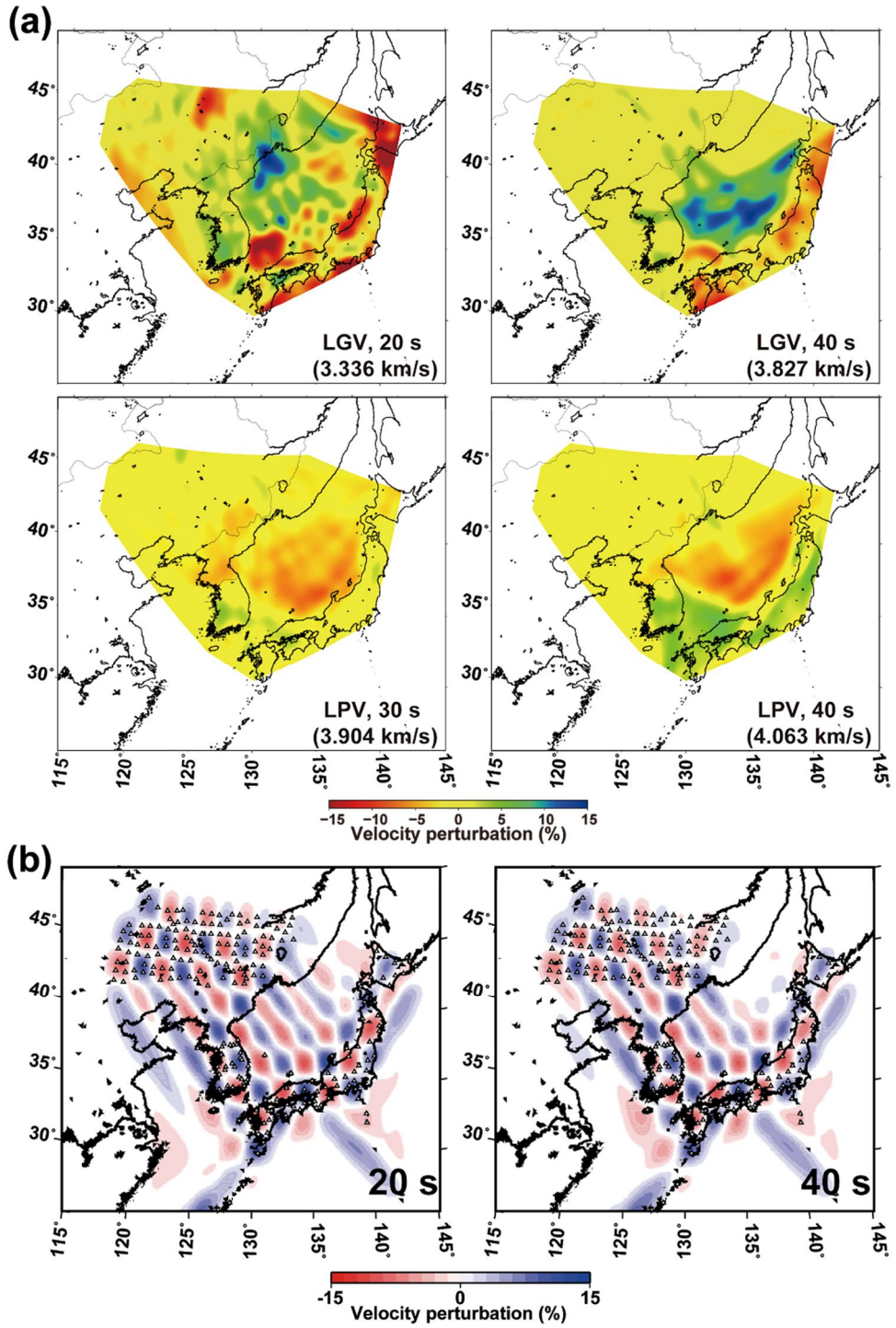

Figure 4.2. (a) Love wave group and phase velocity maps. (b) Checkerboard test results of synthetic tests for Love wave group and phase velocity at 20 and 40 s

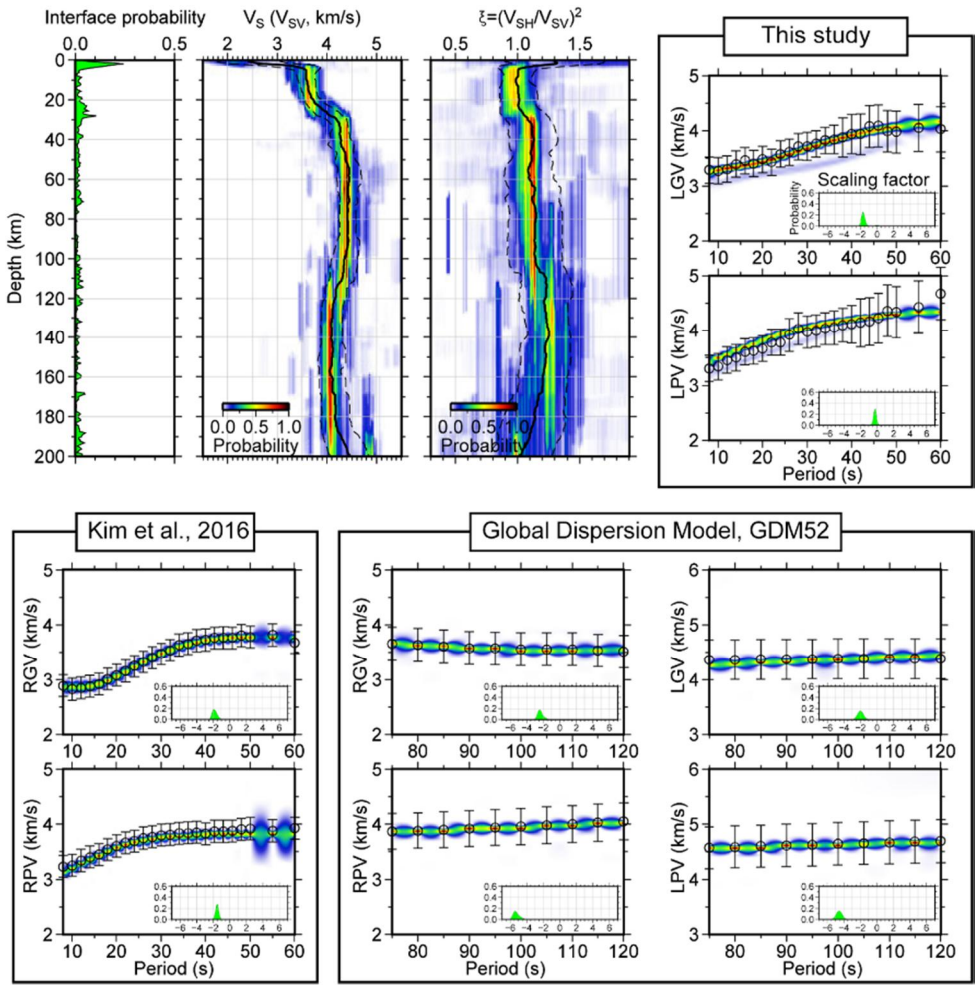

Figure 4.3. Posterior probability distribution (PPD) of layer boundaries, shear wave velocity, anisotropy in depth, number of layers of the Bayesian inversion result using Rayleigh/Love wave dispersions at Korea peninsula (34.9° N, 129.5° E), and posterior distributions of predicted synthetic data with observed data. Total of eight different types of dispersion maps of Love waves from this study (period 8–60 s), Rayleigh waves from previous tomographic study (Kim et al., 2016; period 8–60 s), and longer period data (period 70–120 s) from a global model (Ekstrom, 2011) are inverted together to estimate 1–D shear wave velocity models. Rayleigh wave group velocity: RGV; Love wave group velocity: LGV; Rayleigh wave phase velocity: RPV; Love wave phase velocity: LPV.

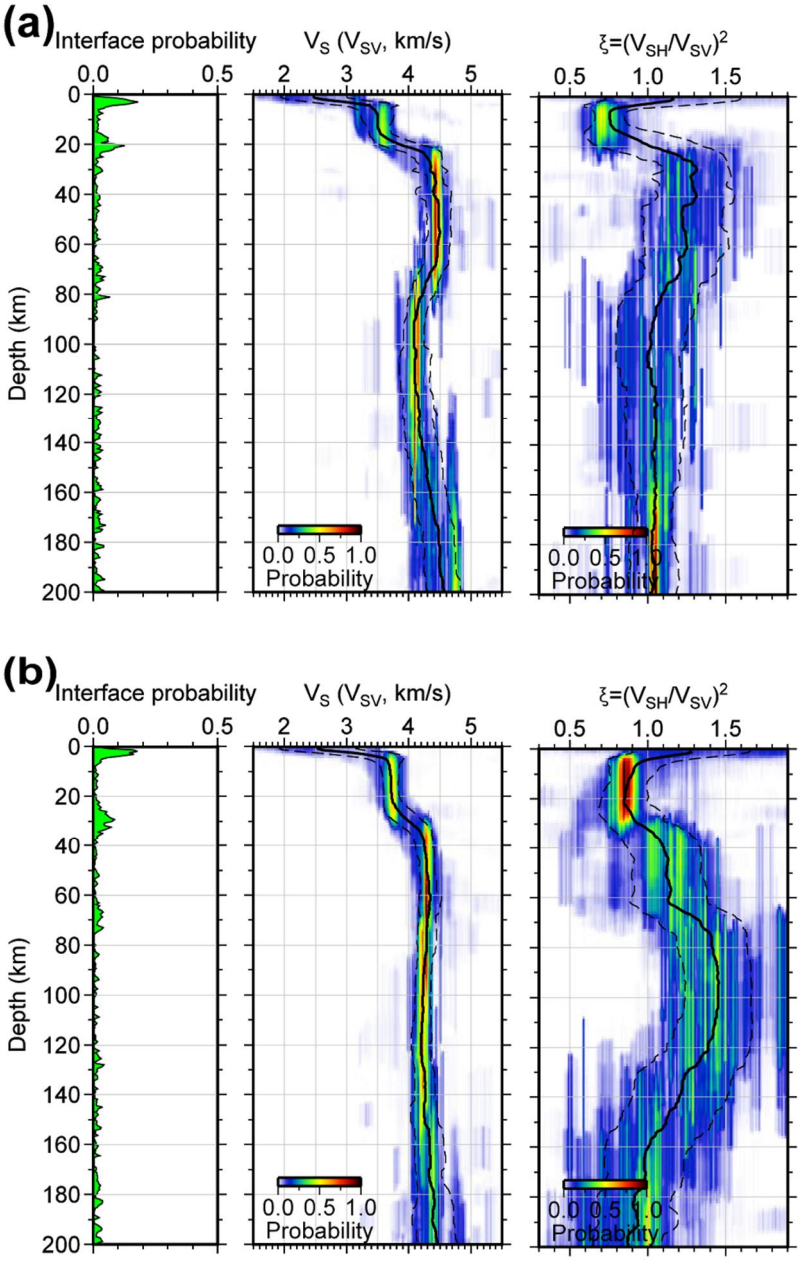

Figure 4.4. The posterior probability distribution (PPD) of layer boundaries, shear wave velocity, anisotropy in depth, and number of layers of the Bayesian inversion result using Rayleigh/Love wave dispersions at (a) Ulleung basin and (b) Mount Baekdu region.

4.3. Results and Discussion

4.3.1. Inversion

The constructed Love wave group velocity (LGV) maps were generally similar to those of the Rayleigh wave group velocity (RGV) maps of the previous study (Fig. 4.2a) (Zheng et al., 2011; Lee et al., 2015; Kim et al., 2016). At 20 s, a low-velocity anomaly of more than 10% was observed beneath the Ulleung basin (UB), and low-velocity anomalies were also dominant beneath the Japan basin (JB) and Yamato basin (YB). In contrast, a high-velocity anomaly was dominant in other ES regions and the Korean Peninsula (KP). Meanwhile, a high-velocity anomaly was generally dominant in the ES, and a low-velocity anomaly appeared following the Japan Island (JI) at 40 s. In the northeastern China region, a low-velocity anomaly occurred in the area corresponding to the Songliao basin (SB) at 20 s, and the anomaly weakened in long periods (Zheng et al., 2011). In Love wave phase velocity (LPV) maps, a low-velocity anomaly of about 5% was dominant in the ES and the northern part of the KP, and a high-velocity of anomaly about 5% was narrow in the southern part of the KP. This pattern was shown up to longer periods, but a high-velocity anomaly extended from the southern part of the ES to the JI. The results of a checkerboard test with a velocity difference of ±15% at 2° × 2° grids showed that the velocity difference was generally well restored at periods

of 20 and 40 s (Fig. 4.2b). The checkers were restored well without distortion in northeastern China, the KP, and the JI, while they were smeared in the northwest–southeast direction in the northern part of the ES because of the path effect between the networks.

Fig. 4.3 presents 1–D inversion results for the KP region (34.9° N, 129.5° E). The calculated posterior probability distributions (PPDs) show that the V_{SV} increases at around a depth of 30 km and ξ also changes to positive radial anisotropy ($V_{SH} > V_{SV}$). This depth coincides with the known average Moho depth of the south of the KP (Kim et al., 2011). The PPDs of V_{SV} and ξ change once more around a depth of 110 km where V_{SV} decreases, and the positive radial anisotropy becomes stronger. Generally, the lithosphere–asthenosphere boundary (LAB) is determined as the depth where V_{SV} decreases and positive radial anisotropy becomes stronger in the upper mantle (Fischer et al., 2010; Doglioni and Panza, 2015; Russell et al., 2019). In these 1–D inversion results, therefore, the LAB can be determined as 110 km, which is similar to results of the previous studies that estimated the LAB to be 90–150 km in the southern part of the KP (Hamza and Vieira, 2012; Wang et al., 2017). However, the result is different from the LAB of Litho 1.0 (Pasyanos et al., 2014), where the LAB was less than 60 km in the southern part of the KP. Considering recent local tomography results of the East Asia region, which show a thicker

lithosphere (>100 km) than surrounding regions, the difference of LAB depth with Litho 1.0 in the Korea peninsula seems to be due to the difference in global data and local data (Wang et al., 2017; Tao et al., 2018; Ma et al., 2019). Meanwhile, the PPD of the radial anisotropy changes rapidly with depth in the UB (Fig. 4.4a). Considering V_{SV} changes together, the Moho depth is about 20 km, which is consistent with the previous study (Chough et al., 2000). In addition, radial anisotropy rapidly changes from negative to positive, and positive radial anisotropy is dominant up to about 70 km but weakens at deeper depths. In contrast, a 1-D example of the Mt. Baekdu volcano (MBV) shows that negative radial anisotropy is dominant up to 30 km, and the PPD of ξ changes to positive at deeper depths (Fig. 4.4b). This positive radial anisotropy is strongest at a depth of 60-120 km and weakens at deeper depths. Comparing the 1-D inversion results, the radial anisotropy changes more rapidly in the UB and MBV than in the KP. In order to verify that our inversion scheme can be restored with rapid changes in the ξ model, we calculated synthetic RGV, LGV, RPV, and LPV using the linear inversion scheme of Herrmann and Ammon (2002) with simplified input models from the 1-D inversion results for the UB or MBV and adopted our inversion scheme (Fig. 4.5). Synthetic test results show that rapid changes in the ξ model are generally well restored, and initial models and the results mostly overlap within $\pm 2\sigma$ up to depth a 150 km.

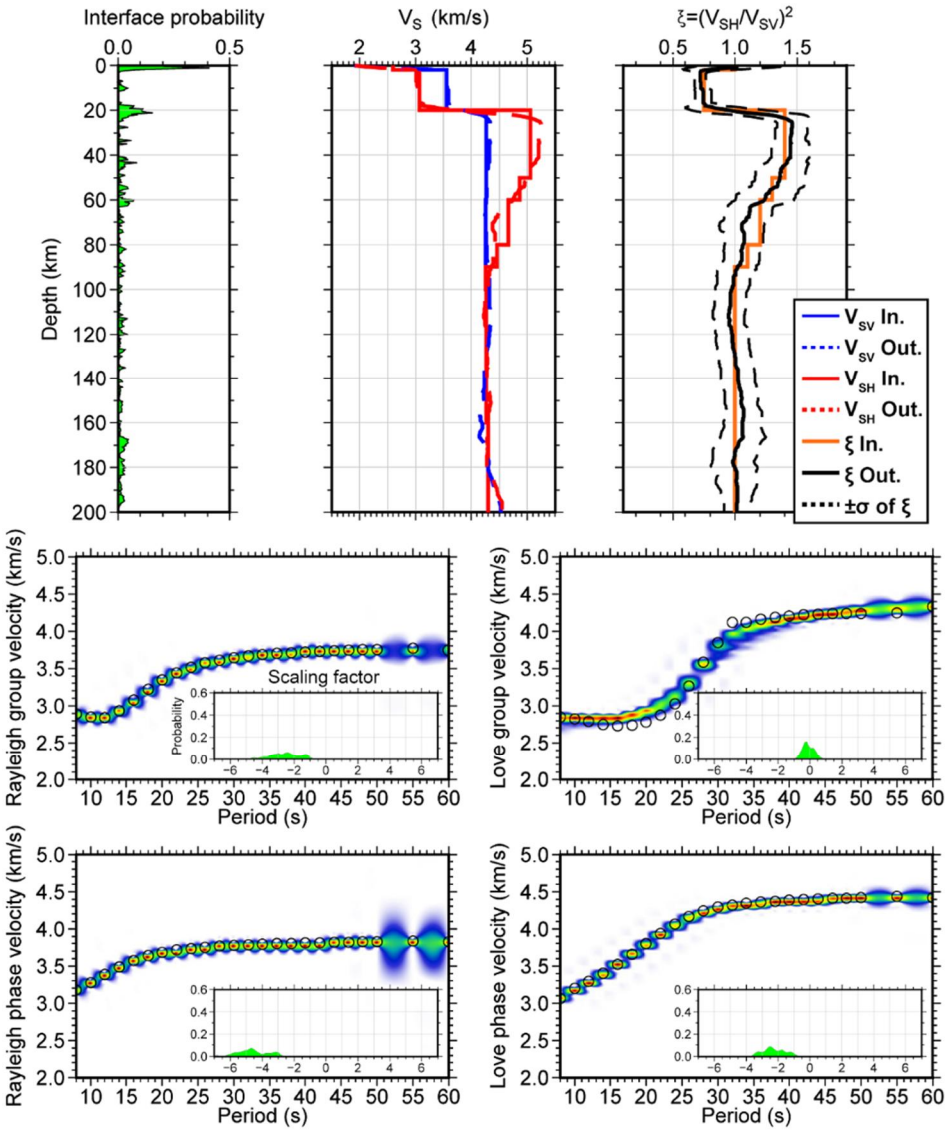

Figure 4.5. Synthetic test results of 1−D shear velocity and anisotropy in depth. Rayleigh and Love dispersion curves are calculated by using inputs V_{SV}, V_{SH}, and anisotropy models (red, blue, and orange solid lines), similar to those observed in Ulleung Basin. V_{SV}, V_{SH} (red and blue dashed lines, respectively), and radial anisotropy (black) models are inverted following the inversion scheme. Inverted models and posterior distributions of predicted synthetic data match input models and dispersion curves reasonably well.

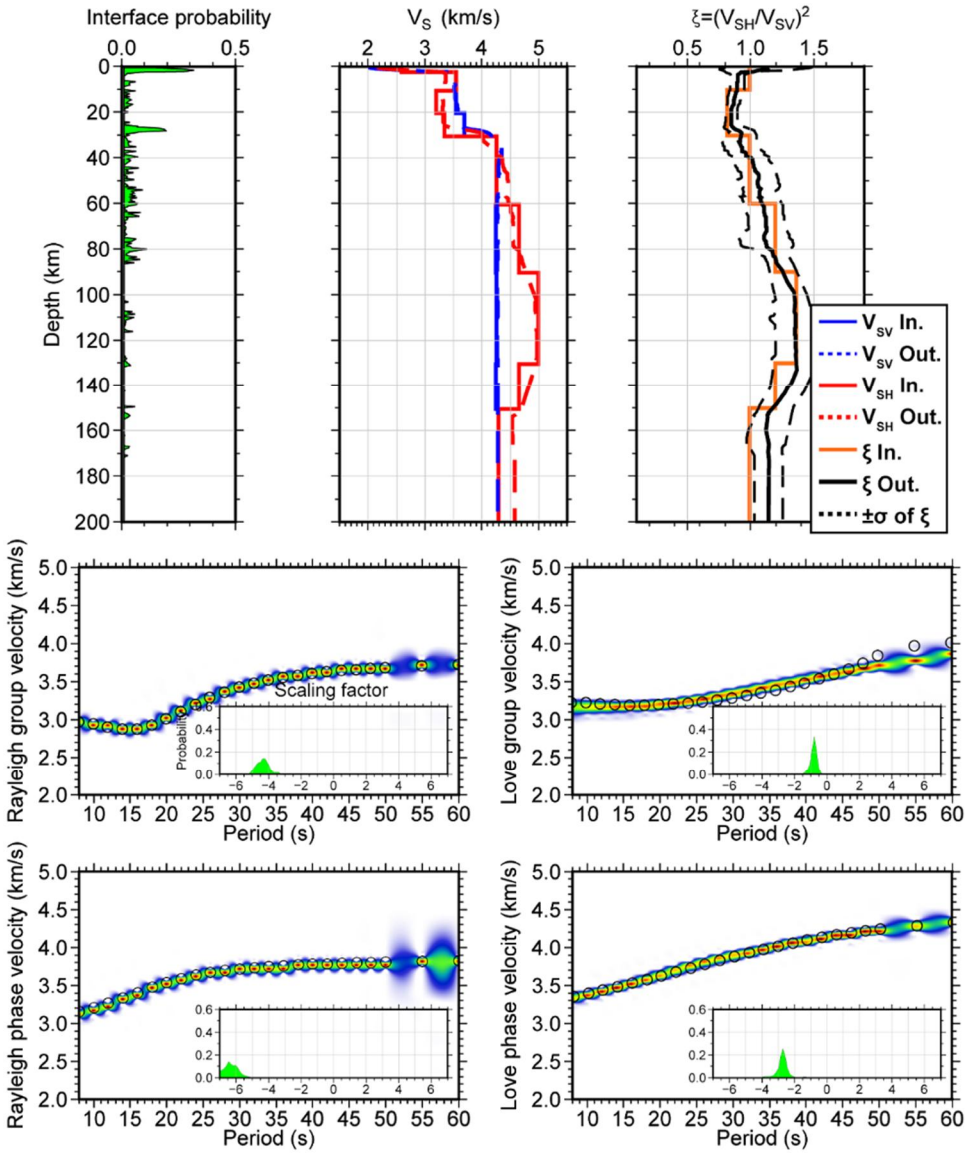

Figure 4.5. Continued.

4.3.2. 3-D model

We constructed 3-D ξ and V_{SV} models by integrating the results of 1-D Bayesian inversions at 609 grid nodes (Fig. 4.6). The ξ model at a depth of 30 km showed that the positive radial anisotropy is dominant in the ES. The same characteristics were also identified in the area corresponding to the SB, which was known to experience crustal extension (Zheng et al., 2011; Guo et al., 2016). Considering the V_{SV} model at a depth of 30 km, both ES and SB regions were relatively faster than the surrounding regions. Previous studies suggested that the crust thickness of the two regions is about 20 km (Chough et al., 2000; Zheng et al., 2011; Guo et al., 2016). Therefore, relatively high velocity and the predominance of positive radial anisotropy seem to indicate the top of the mantle in the two regions. With the increase in depth, the positive radial anisotropy in the ES began to weaken from JB to the entire region. Deeper than 100 km, the radial anisotropy was weak throughout the ES, while the positive radial anisotropy predominated along the KP, northeast China, the JI, and also following the shallow continental margin (e.g., Korea Strait) and topographic highs (e.g., Korea plateau) around the ES. In the V_{SV} model, the Y-shaped low-velocity anomaly reported by Zheng et al. (2011) appeared along the edge of the ES at a depth of 60 km. With the increase in depth, the low-velocity anomaly became dominant throughout the ES and gradually expanded westward.

The difference in ξ and V_{SV} models of the inland and ES was also clear in profiles that cross these regions (Fig. 4.7). The predominant depth of positive radial anisotropy was about 70–150 km in the inland area, while it was strong at shallower depth (20–70 km) and became weak as the depth deepened in the ES. It is well-known that there is a flow with positive radial anisotropy beneath the lithosphere, and this characteristic can be used to define the physical LAB with the velocity model (Fischer et al., 2010; Doglioni and Panza, 2015; Russell et al., 2019). The LAB of the northeastern China region from Litho 1.0 was 60–80 km, which corresponded to the depth where the positive radial anisotropy became dominant in the ξ model (profile A, B of Fig. 4.7). In addition, the descending high-velocity body of the southern SB was also identified in the V_{SV} model, and corresponding weak anisotropy appeared in the same region, unlike the surrounding area where the positive radial anisotropy predominated (Guo et al., 2016). In the JI region, the subducting Pacific plate could be identified in the V_{SV} model, its depth was well-matched with the Wadati-Benioff slab interfaces, and the strong low-velocity anomaly at the top of the V_{SV} model coincided with the locations of the arc volcanoes. In addition, the positive radial anisotropy reflecting the horizontal mantle flow above the subducting slab was also confirmed in the ξ model. These results of fitting well-known structures suggest that the 3-D ξ and V_{SV} model were generally well-constructed.

In the ES region, the thickness of the lithosphere was 25–70 km in the global and regional models (Hamza and Vieira, 2012; Pasyanos et al., 2014; Wang et al., 2017). Considering this, the ES seemed to consist of the lithosphere with strong positive radial anisotropy and the asthenosphere with weak anisotropy, which is different from the general continental region. The JB was composed of oceanic crust formed from the ridge (Chough et al., 2000). A previous study showed that near the ridge, the lithosphere is thin and the anisotropy at the asthenosphere is weakened because the horizontal flow was disturbed by the upwelling flow (Eilon et al., 2014). In addition, the direction of olivine in the lithosphere arranged along the divergence direction of the plate, resulting in positive radial anisotropy in the lithosphere (Beghein et al., 2014; Russell et al., 2018). In profile B of Fig. 4.7, the positive radial anisotropy was dominant up to 50 km and weakened with the relatively low velocity (–5%) with depth. Therefore, the JB region could be seen as a typical structure common in the ridge and the oceanic plate.

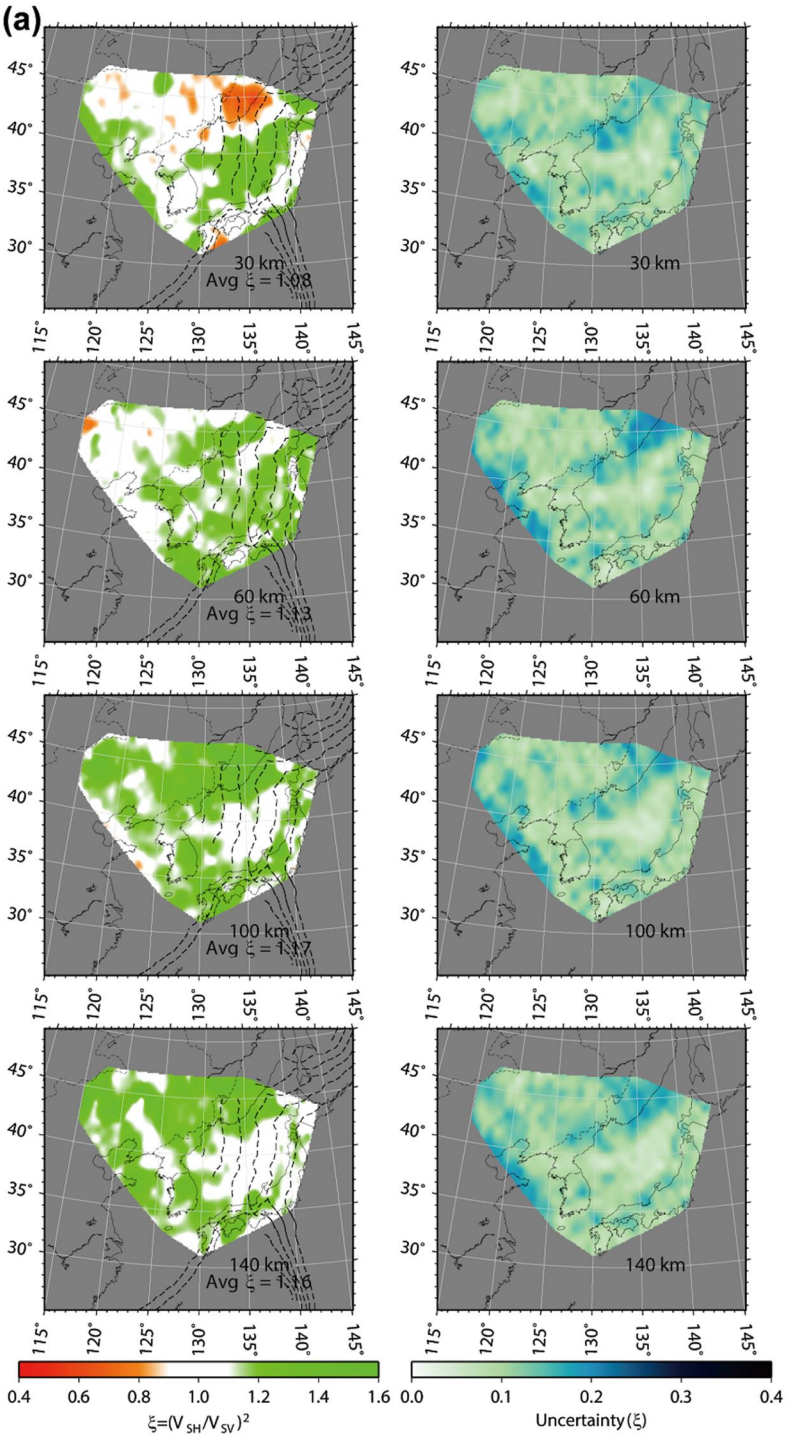

Figure 4.6. (a) Horizontal slices of the anisotropy model and uncertainties for NE Asia for selected depths. The depth and mean anisotropy are presented in the right corner. (b) Horizontal slices of the Vsv model and uncertainties.

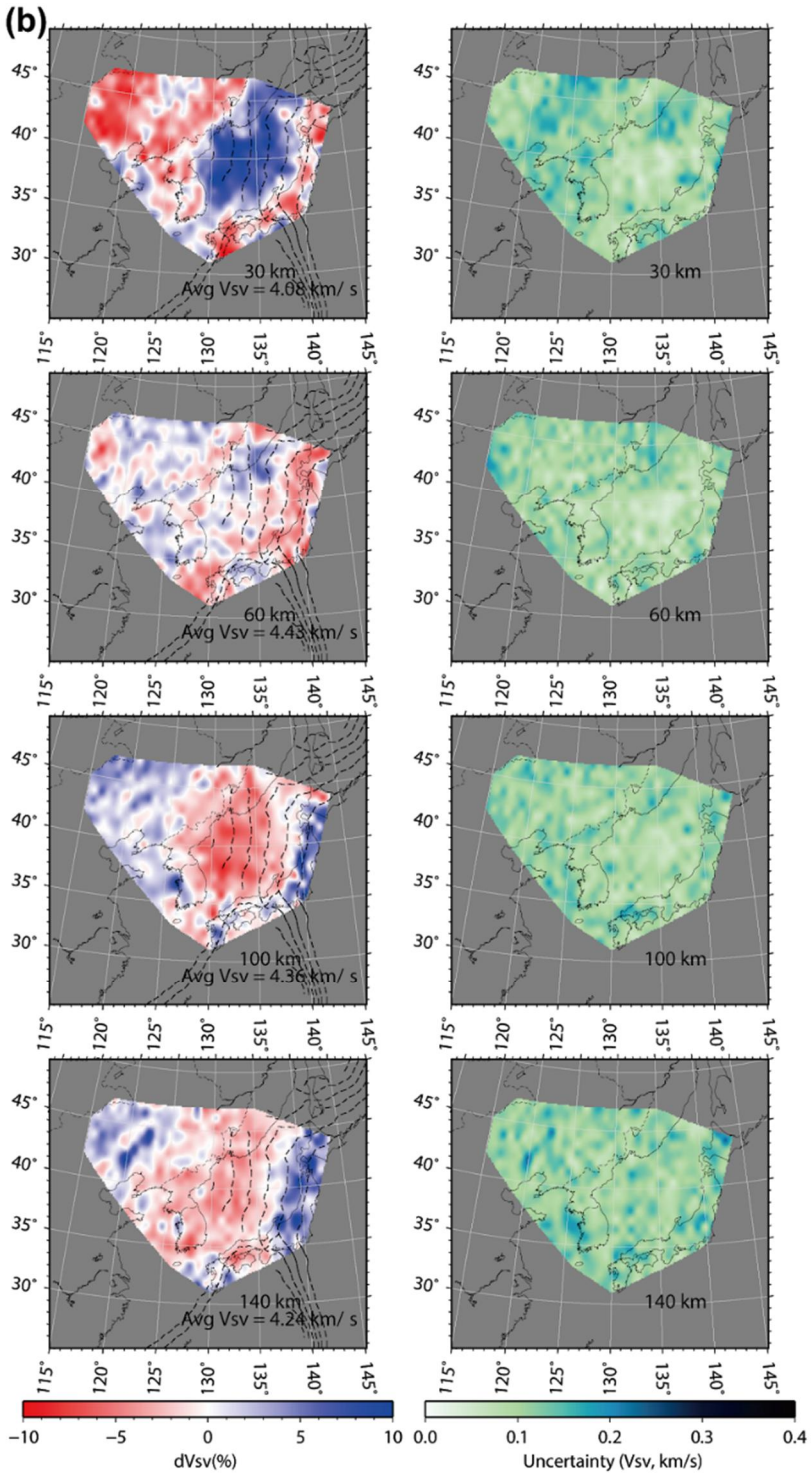

Figure 4.6. Continued.

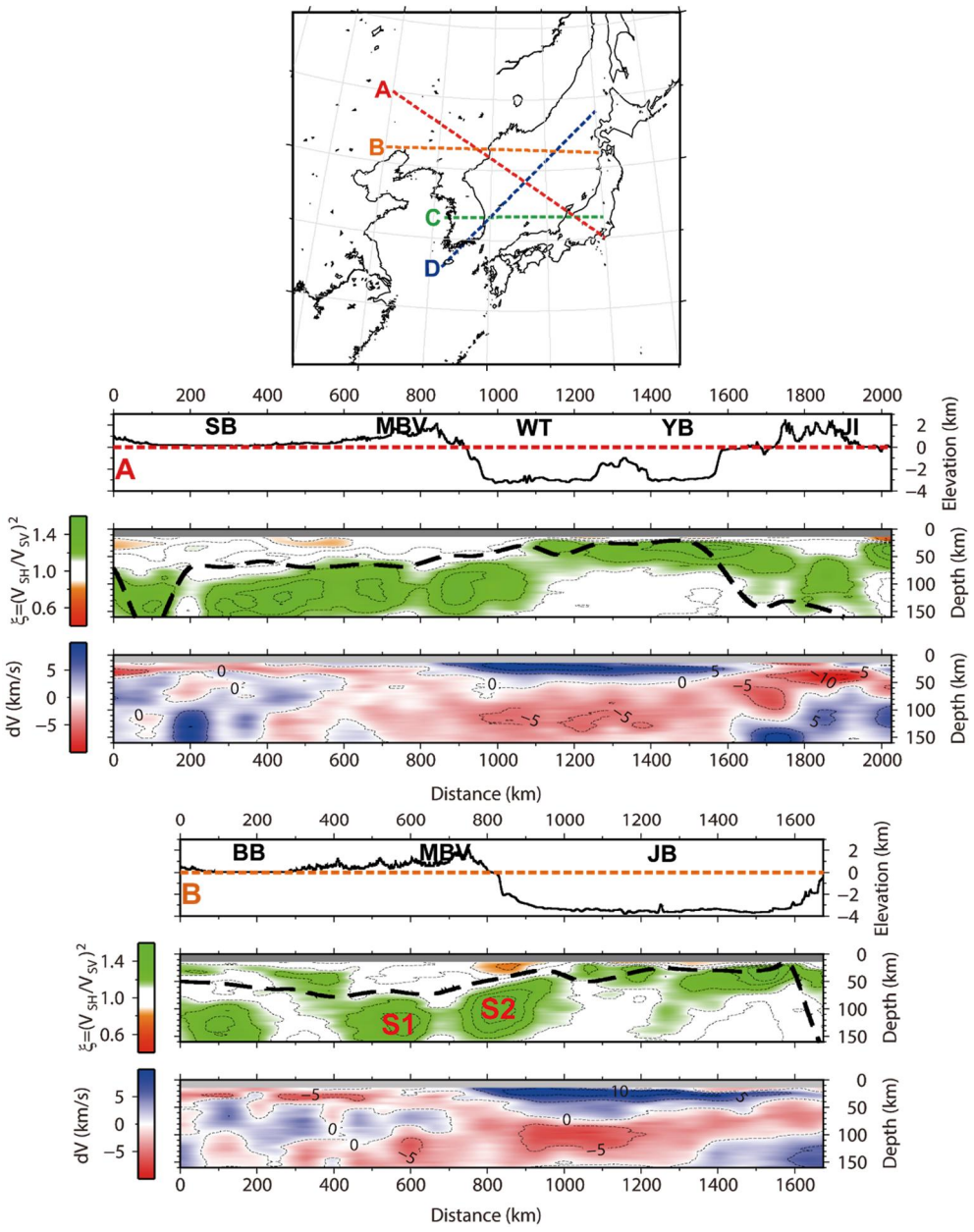

Figure 4.7. Vertical sections of the anisotropic model and Vsv models (relative) following profiles. LAB from Litho 1.0 is plotted with the anisotropic model (black dashed line).

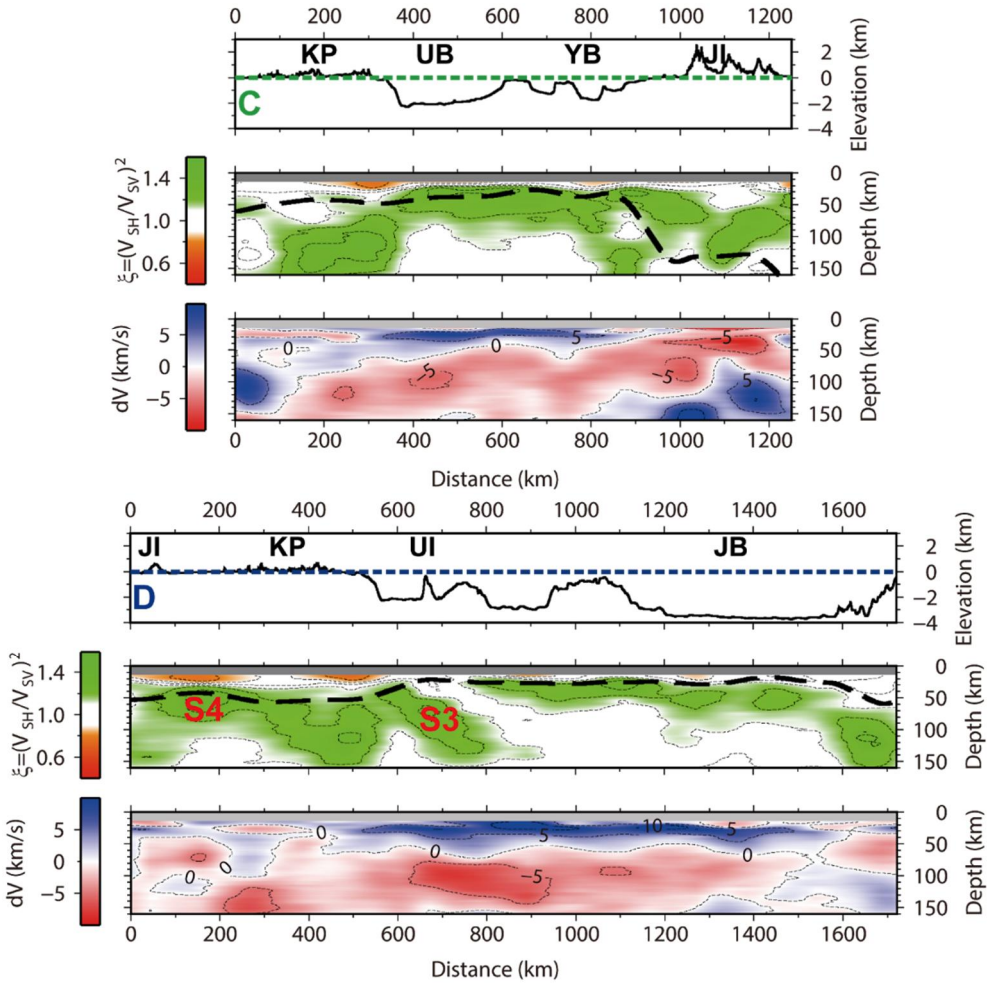

Figure 4.7. Continued

In contrast, the UB and YB were known to be formed by extension of the continental crust during the ES opening (Tamaki, 1988; Chough et al., 2000). The upper mantle structure in the inverted model of these regions was similar to the JB. Jolivet et al. (2009) insisted that a total estimated amount of extension of the order of 50–100 km over a time span of 10 Ma is sufficient to reset the mantle fabric in cases where the lithosphere is warm through studies of the Mediterranean region with scattered back-arc basins. The UB and YB were known to have experienced more than 10 Ma of extension on a scale of 100–200 km (Tamaki, 1988; Chough et al., 2000). Indeed, the amount of geothermal heat flow in the ES is much higher than the fore-arc or KP (Currie and Hyndman., 2006). Additionally, previous tomography studies have revealed the presence of a strong low-velocity anomaly beneath the ES, also confirmed by an inverted V_{SV} model (Wei et al., 2012; Simute et al., 2016). Meanwhile, the low-velocity anomaly tilted down westward and seemed to be connected to the mantle wedge beneath the NEA imaged by the previous study (Wei et al., 2012). Thus, the condition of the UB and YB seemed to be sufficient to reset the mantle fabric in the lithosphere horizontally during the ES opening.

Dynamic modeling results indicated that hot mantle upwelling can cause small-scale convection in the asthenosphere (Currie and Hyndman, 2006; Currie et al., 2008). Furthermore, chemical heterogeneities caused by upwelling can drive convection in the

asthenosphere (Alder et al., 2017). When such convection occurred, dynamic modeling confirmed that the upper part of the convection appeared to have positive radial anisotropy due to the horizontal flow beneath the lithosphere, and the negative radial anisotropy is strengthened within the asthenosphere where the upward flow is predominant (Alder et al., 2017). Therefore, the dominant positive radial anisotropy up to 70 km in the UB and YB seemed to represent a horizontally reset mantle fabric in the lithosphere with the horizontal flow in the upper part of the convection in the asthenosphere, while the horizontal flow beneath the general continental lithosphere was disturbed by convection and was imaged as weak anisotropy. These anisotropic changes in the basins can also be confirmed by the azimuthal anisotropy results of previous studies (Liu and Zhao, 2016; Jolivet et al., 2018; Ma et a., 2019). These studies showed that anisotropy in the northwest–southeast or north–south direction is strong at the depth of the lithosphere (~50 km) similar to the extensional direction of the ES. In contrast, the anisotropy in the east–west direction parallel to the current absolute plate motion was generally dominant at depths of the asthenosphere (~200 km), while the regional–scale result showed weak azimuthal anisotropy in the ES at a shallower depth (~100 km) (Liu and Zhao, 2016; Ma et a., 2019).

There are some back–arc basins showing similar V_{SV} and ξ models with the ES such as the Liguro–Provenciral and Tyrrhenian

basin in the Mediterranean and Lau basin in Fiji Tonga (Jolivet et al., 2009; Chang et al., 2010; Isse et al., 2019). All three basins were formed in the back-arc extension environment, and there was a trace of the mantle upwelling. Moreover, the positive radial anisotropy is predominant in the lithosphere and the anisotropy is weakened in the asthenosphere, identical to the UB and JB in the ES

Previous studies have proposed various deep source mechanisms of the intraplate volcanism in the NEA based on seismic tomography or the composition of the rock samples. Some suggested wet plume(s) models generated from the top of the stagnant slab in the mantle transition zone (Lei and Zhao, 2005; Lei et al., 2013; Zhang et al., 2018; Choi et al., 2020). Other ideas included hot and wet upwelling flows in the big mantle wedge associated with the deep subduction of the western Pacific plate or hot upwelling models feeding from deeper (below the mantle transition zone) sources (Ma et al., 2018; Yang et al., 2018; Tao et al., 2018; Ma et al., 2019; Lü et al., 2019). Meanwhile, geodynamic modeling results have confirmed that various localized processes (e.g., cracking of the lithosphere, small-scale convections, or shear flow beneath the lithosphere) can also cause basaltic intraplate volcanisms (King and Ritsema, 2000; Raddick et al., 2002; Till et al., 2010; Ballmer et al., 2015). Therefore, considering our inversion depth (up to 160 km), we will now discuss the possible relation between localized tectonic processes and intraplate volcanisms

inferred from our isotropic and anisotropic models.

The strong low-velocity anomaly beneath the ES tends to rise from west to east with a gentle slope (Fig. 4.7). The mantle wedge beneath the NEA has been imaged by previous tomographic studies (Wei et al., 2012; Zhao et al., 2017; Tao et al., 2018). In addition, some tomography results indicate that the lithospheric magma fed obliquely from the low-velocity anomaly beneath the ES to the MBV (Lei and Zhao, 2005; Ma et al., 2019). Meanwhile, the positive radial anisotropy beneath the MBV can be divided into S1 and S2 (profile B of Fig. 4.7). S1 corresponds to the thickest corner of the lithosphere in northeastern China, and S2 is located at the slope between the western thick and eastern thin lithosphere, while the positive radial anisotropy in S2 is stronger than that in S1.

Conard et al. (2011) showed a statistical correlation between intraplate volcanism and the rapid shear zone in the asthenosphere due to mantle convection. Additionally, many geodynamic modeling results have confirmed that localized hot asthenospheric shear flow from underneath the thicker lithosphere to the thinner lithosphere can cause edge-driven convection (EDC) and partial melt along areas with a large gradient in the LAB (King and Anderson, 1998; King and Ritsema, 2000; Till et al., 2010; Kaislaniemi and Jeroen van Hunen, 2014; Davies and Rawlinson, 2014). In our models, the difference in lithosphere thickness between northeast China and the

ES is about 50 km (Fig. 4.7). There are two types of EDCs. One is dominated by cold down-welling and its return flow at the relatively cold slope following the LAB on the order of 300-500 km in diameter, and the other is caused by sublithospheric lateral flow from the thicker lithosphere to the thinner lithosphere with smaller convection sizes up to ~200 km (King and Anderson, 1998; King and Ritsema, 2000). Assuming S1 and S2 are localized lateral asthenospheric shear flows, the latter type of the EDC can be driven between northeast China and the ES (Fig. 4.7). Geodynamic modeling results also indicate that the stronger sublithospheric flow from the thicker to thinner lithosphere causes stronger EDC, and the horizontal flow below the LAB slope can be enhanced (King and Anderson, 1998; Till et al., 2010; Davies and Rawlinson et al., 2014; Kaislaniemi and van Hunen, 2014). This is consistent with the result that the positive radial anisotropy in S2 is stronger than that in S1.

In contrast, S2 overlaps with a branch of the low-velocity anomaly extending to the MBV (Fig. 4.7). This is consistent with previous tomography results that showed obliquely intruded magma from the low-velocity anomaly beneath the ES to the MBV (Lei and Zhao, 2005; Ma et al., 2019). Recent Pn tomography results also calculated that the magma supply of intraplate volcanic regions in northeast China started from the MBV to the west and northward (Du and Lei, 2019). In addition, Till et al. (2010) confirmed that the

size of upwelling was sensitive to the depth of the thicker lithosphere and the gradient of the LAB. The thickness of the lithosphere beneath the MBV reaches up to 100 km and the width of the step to the ES reaches up to 300 km. Therefore, upwelling can be expected along narrow areas in tens of kilometers. In addition, the 3-D dynamic modeling result of the EDC shows that melting pockets are formed separately along the gradient of the LAB (Kaislaniemi and van Hunen, 2014). These correspond well to the low-velocity anomaly along the ES, continental boundaries at depths of 60 km, and distinctive locations of intraplate volcanoes in the NEA (Fig. 4.6). Meanwhile, the ES experienced a back-arc extension from the Early Oligocene (~32 Ma) to about 15 Ma, the basaltic eruption of the MBV started from the Miocene to Pliocene (20-2.6 Ma), and other Cenozoic volcanoes in the NEA also erupted in the latter part of the opening of the ES (22 Ma-1 ka) (Tamaki, 1988; Chough et al., 2000; Park et al., 2017; Choi et al., 2020). Therefore, it can be interpreted that the opening of the ES that culminated at about 15 Ma accompanied the difference in lithosphere thickness, which can cause EDC in the NEA. Considering these tectonic histories and our model with dynamic modeling results, S1 in profile B of Fig. 4.7 seems to represent sublithospheric lateral flow of the mantle wedge, and S2 can represent enhanced lateral flow with the EDC along areas with a large gradient of the LAB. Then, these shallow and localized

tectonic process mechanisms, as well as the source from the deeper mantle, can also cause basaltic intraplate volcanism beneath the MBV.

Thus, a possible scenario for supplying magma to the MBV is as follows. (1) The subduction of the Pacific plate caused a mantle wedge (Wei et al., 2012; Liu et al., 2017; Ma et al., 2019). (2) Small-scale convections were induced by thermal and chemical heterogeneities in the asthenosphere during the ES opening (from the Early Oligocene (~32 Ma) to about 15 Ma), and the lithosphere beneath the ES became thinned (Currie and Hyndman, 2006; Currie et al., 2008; Alder et al., 2017). (3) The difference in the thickness in the lithosphere triggered the EDC and the magma supplied from the sublithosphere to the MBV (King and Ritsema, 2000; Kaislaniemi and van Hunen. 2014). Additionally, the magma supply through various depths could explain various compositional eruptions at the MBV (from basalt to ignimbrite) from the Miocene to Holocene (Wang et al., 2003; Wei et al., 2007; Park et al., 2017; Choi et al., 2020).

The tectonic setting of Ulleung Island (UI) is similar to the MBV (profile D of Fig. 4.7). Recent studies have shown that there is a thick lithosphere (>150 km) in the southwestern part of the KP (Tao et al., 2018; Ma et al., 2019). In addition, a strong positive radial anisotropy, S3, was located at the slope between the western

thick and eastern thin lithosphere and overlapped with the low-velocity anomaly (>-5 %) beneath UI. The eruption of UI also started from 16 Ma, the latter part of the extension. However, the low-velocity branch connecting the low-velocity anomaly and UI was not imaged in the V_{SV} model. This seems to be due to the relatively narrow intrusion beneath UI compared to the inversion resolution.

In the case of Jeju Island (JI), a strong positive radial anisotropy, S4, shallower (50-80 km) than the others, was located beneath JI and overlapped with the low-velocity anomaly. It is consistent with the results of Song et al. (2018). Song et al. (2018) confirmed the existence of partial melt near a depth 60 km beneath JI through travel time tomography and interpreted it as focused decompressional melting in the lower part of the lithosphere. Though the Yellow Sea basin, western side of JI, was also known to have a thick lithosphere, the anisotropy pattern cannot be confirmed, because it is not included in our ξ model. Meanwhile, Tao et al. (2018) showed that the positive radial anisotropy was strong beneath the Yellow Sea basin at a depth of 80-100 km. Therefore, the tectonic setting around JI could be similar to that of the MBV and UI. In contrast, Brenna et al. (2012) suggested the possibility of the existence of shear zones in the lithosphere beneath JI from geochemical data. It was also consistent with our ξ model that overlapped with the low-velocity anomaly. Meanwhile, Ballmer et al.

(2015) showed that the effective viscosity of the asthenospheric flow can change critically near the thick lithosphere beneath the plateau; and small-scale EDC can also be triggered in lateral variation of the LAB. Thus, a thick lithosphere (>150 km) in the southwestern part of the KP can also cause basaltic intraplate volcanisms in JI. Therefore, in order to better understand the magma process in the upper mantle beneath JI, a wider range of studies including the Yellow Sea and the South China Sea are needed.

4.4. Summary

In this study, we calculated Love wave dispersion maps using the horizontal component of the ambient noise continuous data recorded at broadband networks in the NEA region and constructed 3-D ξ and V_{SV} models using dispersion data from previous studies together. The well-known major tectonic structures of NEA, such as the subducting Pacific plate, SB, and low-velocity anomaly beneath the ES, were imaged well in our models. Our models also provided ideas for understanding the mechanisms of various tectonic processes in the ES and surrounding regions. The predominant depth of positive radial anisotropy in the ES was shallower than 20–70 km in the inland area (70–150 km) and became weak with depth. This could be interpreted as the trace of

small-scale convection and extension caused by the physical and chemical heterogeneities from the mantle wedge beneath the ES. In addition, a difference in lithosphere thickness caused by extension could produce the EDC, and it seems to be related to sublithospheric localized processes for intraplate volcanoes in NEA.

Chapter 5.

Summary and conclusion

In this thesis, the ambient noise tomography technique is basically used to image the seismic velocity structures of specific regions in northeast Asia, such as the Northern Korean Peninsula (NKP), Jeju Island (JI), East Sea and surrounding regions For inversion, surface wave dispersion curves for each inversion node are calculated from the overall average or group and phase velocity maps. The combination of fast marching method (FMM) and the subspace method is applied for group and phase velocity maps. The obtained surface wave dispersion data are inverted to estimate 1-D shear wave, 3-D isotropic and anisotropic velocity models for the Korean Peninsula and surrounding regions

Firstly, I present 1-D velocity models for both the inland and offshore (western East Sea) of the NKP. I constrained the models based on the results of a Bayesian inversion process using Rayleigh wave dispersion data, which were measured from ambient noise cross-correlations between stations in the southern Korean Peninsula and northeast China. The proposed models were evaluated by performing full moment tensor inversion for the 2013 Democratic Peoples republic of Korea (DPRK) nuclear test. Using the composite model consisting of both inland and offshore models resulted in consistently higher goodness of fit to observed

waveforms than previous models. This indicates that seismic monitoring can be improved by using the proposed models, which resolve propagation effects along different paths in the NKP region.

Secondly, I imaged upper crustal isotropic and radial anisotropic structures beneath JI using ambient noise data from a temporary seismic network. The results show that layers of negative anisotropy ($V_{SH} < V_{SV}$) are predominant at shallower (<2 km) and deeper (>5 km) depths, which was interpreted as reflecting dyke swarms responsible for the more than 400 cinder cones at the surface and the vertical plumbing systems supplying magma from deeper sources, respectively. Additionally, a layer with significantly positive radial anisotropy ($V_{SH} > V_{SV}$, up to 5%) was found at middle depths (2–5 km), and was interpreted as horizontally aligned magma plumbing systems (e.g., sills) through comparisons with several other volcanoes worldwide. In comparison with the isotropic structure, the positive anisotropic layer was separated into upper and lower layers with locally neutral to slightly fast and slower shear wave velocities, respectively, beneath the largest central crater (Mt. Halla). Such a structure indicates that the cooled upper part of the magma plumbing systems formed within the horizontally developed sill complex, and is underlain by still-warm sill structures, potentially with a small fraction of melting. With dykes predominant above and below, the island-wide sill layer and locally high-temperature body at the center explain the evolution of the

Jeju Island volcanoes by island-forming surface lava flows and central volcanic eruptions before and after the eruptions of cinder cones.

Lastly, I jointly inverted different types of dispersion data to construct a 3-D radial anisotropy model in northeast Asia. The model images detailed 3D variations in radial anisotropy beneath the study area and I focus on radial anisotropic structures beneath three characteristic regions: (1) Continental regions (Region 1), (2) Regions experienced extension during the Cenozoic (Region 2), and (3) Intraplate volcanic regions (Region 3). For Region 1, thick and deep layers with positive radial anisotropy ($V_{SH} > V_{SV}$) commonly exist at depths between 70 and 150 km. It may represent the existence of horizontal upper mantle flow. On the other hand, layers with positive radial anisotropy become shallower and thinner (30 ~ 60 km) beneath Region 2. Radial anisotropy is nearly negligible at depths between 70 and 150 km in contrast to Region 1. Radial anisotropy in Region 3 can be characterized as shallow layers with negative radial anisotropy ($V_{SV} > V_{SH}$, up to 50 km) and deep layers (50 ~ 150 km) with positive radial anisotropy.

References

Alder, C., Bodin, T., Ricard, Y., Capdeville, Y., Debayle, E., & Montagner, J. P. (2017). Quantifying seismic anisotropy induced by small-scale chemical heterogeneities. *Geophysical Journal International*, *211*(3), 1585-1600.

Almqvist, B. S., & Mainprice, D. (2017). Seismic properties and anisotropy of the continental crust: predictions based on mineral texture and rock microstructure. *Reviews of Geophysics*, *55*(2), 367-433.

Aloisi, M., Cocina, O., Neri, G., Orecchio, B., & Privitera, E. (2002). Seismic tomography of the crust underneath the Etna volcano, Sicily. *Physics of the Earth and Planetary Interiors*, *134*(3-4), 139-155.

Archer, S. G., Bergman, S. C., Iliffe, J., Murphy, C. M., & Thornton, M. (2005). Palaeogene igneous rocks reveal new insights into the geodynamic evolution and petroleum potential of the Rockall Trough, NE Atlantic Margin. *Basin Research*, *17*(1), 171-201.

Artemieva, I. M., Billien, M., Lévêque, J. J., & Mooney, W. D. (2004). Shear wave velocity, seismic attenuation, and thermal

structure of the continental upper mantle. *Geophysical Journal International*, *157*(2), 607-628.

Bagnardi, M., & Amelung, F. (2012). Space□geodetic evidence for multiple magma reservoirs and subvolcanic lateral intrusions at Fernandina Volcano, Galápagos Islands. *Journal of Geophysical Research: Solid Earth*, *117*(B10).

Baker, S., & Amelung, F. (2012). Top□down inflation and deflation at the summit of Kīlauea Volcano, Hawai ‘i observed with InSAR. *Journal of Geophysical Research: Solid Earth*, *117*(B12)

Ballmer, M. D., Conrad, C. P., Smith, E. I., & Johnsen, R. (2015). Intraplate volcanism at the edges of the C olorado P lateau sustained by a combination of triggered edge□driven convection and shear□driven upwelling. *Geochemistry, Geophysics, Geosystems*, *16*(2), 366-379.

Barth, A. (2014). Significant release of shear energy of the North Korean nuclear test on February 12, 2013. *Journal of seismology*, *18*(3), 605-615.

Beghein, C., Yuan, K., Schmerr, N., & Xing, Z. (2014). Changes in seismic anisotropy shed light on the nature of the Gutenberg discontinuity. *Science*, *343*(6176), 1237-1240.

Benediktsdóttir, Á., Gudmundsson, Ó., Brandsdóttir, B., & Tryggvason, A. (2017). Ambient noise tomography of Eyjafjallajökull volcano, Iceland. *Journal of Volcanology and Geothermal Research*, *347*, 250-263.

Bensen, G. D., Ritzwoller, M. H., Barmin, M. P., Levshin, A. L., Lin, F., Moschetti, M. P., & Yang, Y. (2007). Processing seismic ambient noise data to obtain reliable broad-band surface wave dispersion measurements.*Geophysical Journal International*, *169*(3), 1239-1260.

Bodin, T., Leiva, J., Romanowicz, B., Maupin, V., & Yuan, H. (2016). Imaging anisotropic layering with Bayesian inversion of multiple data types. *Geophysical Journal International*, *206*(1), 605-629.

Brenna, M., Cronin, S. J., Smith, I. E., Maas, R., & Sohn, Y. K. (2012). How small-volume basaltic magmatic systems develop: a case study from the Jeju Island Volcanic Field, Korea. *Journal of Petrology*, *53*(5), 985-1018.

Brenna, M., Cronin, S. J., Kereszturi, G., Sohn, Y. K., Smith, I. E., & Wijbrans, J. (2015). Intraplate volcanism influenced by distal subduction tectonics at Jeju Island, Republic of Korea. *Bulletin of volcanology*, *77*(1), 7.

Brenguier, F., Shapiro, N. M., Campillo, M., Nercessian, A., & Ferrazzini, V. (2007). 3□D surface wave tomography of the Piton de la Fournaise volcano using seismic noise correlations. *Geophysical research letters*, *34*(2).

Çakır, Ö. (2018). Seismic crust structure beneath the Aegean region in southwest Turkey from radial anisotropic inversion of Rayleigh and Love surface waves. *Acta Geophysica*, *66*(6), 1303-1340.

Cammarano, F., Tackley, P., & Boschi, L. (2011). Seismic, petrological and geodynamical constraints on thermal and compositional structure of the upper mantle: global thermochemical models. *Geophysical Journal International*, *187*(3), 1301-1318.

Cashman, K. V., & Giordano, G. (2014). Calderas and magma reservoirs. *Journal of Volcanology and Geothermal Research*, *288*, 28-45.

Cervelli, P. F., & Miklius, A. (2003). The shallow magmatic system of Kilauea Volcano. *US Geol. Surv. Prof. Pap*, *1676*, 149-163.

Cesca, S., Heimann, S., Kriegerowski, M., Saul, J., & Dahm, T. (2017). Moment Tensor Inversion for Nuclear Explosions: What Can We Learn from the 6 January and 9 September

2016 Nuclear Tests, North Korea?. *Seismological Research Letters*.

Chang, S. J., & Baag, C. E. (2005). Crustal structure in southern Korea from joint analysis of teleseismic receiver functions and surface-wave dispersion. *Bulletin of the Seismological Society of America*, *95*(4), 1516-1534.

Chang, S. J., & Baag, C. E. (2006). Crustal structure in southern Korea from joint analysis of regional broadband waveforms and travel times. *Bulletin of the Seismological Society of America*, *96*(3), 856-870.

Chang, S. J., Van Der Lee, S., Matzel, E., & Bedle, H. (2010). Radial anisotropy along the Tethyan margin. *Geophysical Journal International*, *182*(2), 1013-1024.

Choi, J., Kang, T. S., & Baag, C. E. (2009). Three-dimensional surface wave tomography for the upper crustal velocity structure of southern Korea using seismic noise correlations. *Geosciences Journal*, *13*(4), 423-432.

Choi, S. H., Jwa, Y. J., & Lee, H. Y. (2001). Geothermal gradient of the upper mantle beneath Jeju Island, Korea: Evidence from mantle xenoliths. *Island Arc*, *10*(2), 175-193.

Choi, H. O., Choi, S. H., Lee, Y. S., Ryu, J. S., Lee, D. C., Lee, S. G., & Liu, J. Q. (2020). Petrogenesis and mantle source characteristics of the late Cenozoic Baekdusan (Changbaishan) basalts, North China Craton. Gondwana Research, 78, 156-171.

Chough, S. K., Lee, H. J., & Yoon, S. H. (2000). *Marine geology of Korean seas*. Elsevier.

Clague, D. A., & Dixon, J. E. (2000). Extrinsic controls on the evolution of Hawaiian ocean island volcanoes. *Geochemistry, Geophysics, Geosystems*, *1*(4).

Conrad, C. P., Bianco, T. A., Smith, E. I., & Wessel, P. (2011). Patterns of intraplate volcanism controlled by asthenospheric shear. *Nature Geoscience*, *4*(5), 317.

Crampin, S. (1981). A review of wave motion in anisotropic and cracked elastic-media. *Wave motion*, *3*(4), 343-391.

Crampin, S. (1984). An introduction to wave propagation in anisotropic media. *Geophysical Journal International*, *76*(1), 17-28.

Crampin, S. (1989). Suggestions for a consistent terminology for seismic anisotropy 1. *Geophysical Prospecting*, *37*(7), 753-770.

Crampin, S., & Lovell, J. H. (1991). A decade of shear-wave splitting in the Earth's crust: what does it mean? what use can we make of it? and what should we do next?. *Geophysical Journal International*, *107*(3), 387-407.

Currie, C. A., & Hyndman, R. D. (2006). The thermal structure of subduction zone back arcs. *Journal of Geophysical Research: Solid Earth*, *111*(B8).

Currie, C. A., Huismans, R. S., & Beaumont, C. (2008). Thinning of continental backarc lithosphere by flow-induced gravitational instability. *Earth and Planetary Science Letters*, *269*(3-4), 436-447.

Davies, D. R., & Rawlinson, N. (2014). On the origin of recent intraplate volcanism in Australia. *Geology*, *42*(12), 1031-1034.

Dalton, C. A., Ekström, G., & Dziewonski, A. M. (2009). Global seismological shear velocity and attenuation: A comparison with experimental observations. *Earth and Planetary Science Letters*, *284*(1-2), 65-75.

Debayle, E., & Kennett, B. L. N. (2000). Anisotropy in the Australasian upper mantle from Love and Rayleigh waveform inversion. *Earth and Planetary Science Letters*, *184*(1), 339-351.

Doglioni, C., & Panza, G. (2015). Polarized plate tectonics. In *Advances in Geophysics* (Vol. 56, pp. 1–167). Elsevier.

Du, M., & Lei, J. (2019). Pn anisotropic tomography of Northeast China and its implications to mantle dynamics. *Journal of Asian Earth Sciences*, *171*, 334–347.

Edmonds, M., Cashman, K. V., Holness, M., & Jackson, M. (2019). Architecture and dynamics of magma reservoirs.

Eilon, Z., Abers, G. A., Jin, G., & Gaherty, J. B. (2014). Anisotropy beneath a highly extended continental rift. *Geochemistry, Geophysics, Geosystems*, *15*(3), 545–564.

Ekström, G., & Dziewonski, A. M. (1998). The unique anisotropy of the Pacific upper mantle. *Nature*, *394*(6689), 168.

Fischer, K. M., Ford, H. A., Abt, D. L., & Rychert, C. A. (2010). The lithosphere–asthenosphere boundary. *Annual Review of Earth and Planetary Sciences*, *38*, 551–575.

Fouch, M. J., & Rondenay, S. (2006). Seismic anisotropy beneath stable continental interiors. *Physics of the Earth and Planetary Interiors*, *158*(2–4), 292–320.

Ford, S. R., Dreger, D. S., & Walter, W. R. (2009). Source analysis of the Memorial Day explosion, Kimchaek, North Korea. *Geophysical Research Letters*, *36*(21).

Ford, S. R., Phillips, W. S., Walter, W. R., Pasyanos, M. E., Mayeda, K., & Dreger, D. S. (2010). Attenuation tomography of the Yellow Sea/Korean Peninsula from coda-source normalized and direct Lg amplitudes. *Pure and applied geophysics*, *167*(10), 1163-1170.

González, P. J., Samsonov, S. V., Pepe, S., Tiampo, K. F., Tizzani, P., Casu, F., & Sansosti, E. (2013). Magma storage and migration associated with the 2011-2012 El Hierro eruption: implications for crustal magmatic systems at oceanic island volcanoes. *Journal of Geophysical Research: Solid Earth*, *118*(8), 4361-4377.

Godfrey, H. J., Fry, B., & Savage, M. K. (2017). Shear-wave velocity structure of the Tongariro Volcanic Centre, New Zealand: Fast Rayleigh and slow Love waves indicate strong shallow anisotropy. *Journal of Volcanology and Geothermal Research*, *336*, 33-50.

Guo, Z., Gao, X., Wang, W., & Yao, Z. (2012). Upper-and mid-crustal radial anisotropy beneath the central Himalaya and southern Tibet from seismic ambient noise tomography. *Geophysical Journal International*, *189*(2), 1169-1182.

Guo, Z., Chen, Y. J., Ning, J., Feng, Y., Grand, S. P., Niu, F., ... & Ni, J. (2015). High resolution 3-D crustal structure beneath NE China from joint inversion of ambient noise and receiver functions using NECESSArray data.*Earth and Planetary Science Letters*, *416*, 1-11.

Guo, Z., Yang, Y., & Chen, Y. J. (2016). Crustal radial anisotropy in Northeast China and its implications for the regional tectonic extension. *Geophysical Journal International*, *207*(1), 197-208.

Hamza, V. M., & Vieira, F. P. (2012). Global distribution of the lithosphere-asthenosphere boundary: a new look. *Solid Earth*, *3*(2), 199-212.

Han, S. I., Lee, J. M., & Kang, T. S. (2010). 1D crustal velocity structure beneath broadband seismic stations in the Okcheon Fold Belt of Korea by receiver function analysis. *Geosciences Journal*, *14*(1), 57-66.

Herrmann, R.B. and Ammon, C.J. (2002). Computer programs in seismology: Surface waves, receiver functions and crustal structure. Version 3.30, Saint Louis University.

Hildner, E., Klügel, A., & Hansteen, T. H. (2012). Barometry of lavas from the 1951 eruption of Fogo, Cape Verde Islands: Implications for historic and prehistoric magma plumbing

systems. *Journal of Volcanology and Geothermal Research*, *217*, 73-90.

Hong, T. K., Baag, C. E., Choi, H., & Sheen, D. H. (2008). Regional seismic observations of the 9 October 2006 underground nuclear explosion in North Korea and the influence of crustal structure on regional phases. *Journal of Geophysical Research: Solid Earth*, *113*(B3).

Hong, T. K., & Rhie, J. (2009). Regional source scaling of the 9 October 2006 underground nuclear explosion in North Korea. *Bulletin of the Seismological Society of America*, *99*(4), 2523-2540.

Hudson, J. A., Pearce, R. G., & Rogers, R. M. (1989). Source type plot for inversion of the moment tensor. *Journal of Geophysical Research: Solid Earth*, *94*(B1), 765-774.

Huang, H., Yao, H., & van der Hilst, R. D. (2010). Radial anisotropy in the crust of SE Tibet and SW China from ambient noise interferometry. *Geophysical Research Letters*, *37*(21).

Huang, H. H., Lin, F. C., Schmandt, B., Farrell, J., Smith, R. B., & Tsai, V. C. (2015). The Yellowstone magmatic system from the mantle plume to the upper crust. *Science*, *348*(6236), 773-776.

Ishizuka, O., Geshi, N., Itoh, J. I., Kawanabe, Y., & TuZino, T. (2008). The magmatic plumbing of the submarine Hachijo NW volcanic chain, Hachijojima, Japan: Long□distance magma transport?. *Journal of Geophysical Research: Solid Earth*, *113*(B8).

Isse, T., Kawakatsu, H., Yoshizawa, K., Takeo, A., Shiobara, H., Sugioka, H., ... & Reymond, D. (2019). Surface wave tomography for the Pacific Ocean incorporating seafloor seismic observations and plate thermal evolution. *Earth and Planetary Science Letters*, *510*, 116-130.

Jaxybulatov, K., Shapiro, N. M., Koulakov, I., Mordret, A., Landès, M., & Sens-Schönfelder, C. (2014). A large magmatic sill complex beneath the Toba caldera. *science*, *346*(6209), 617-619.

Jeddi, Z., Gudmundsson, O., & Tryggvason, A. (2017). Ambient-noise tomography of Katla volcano, south Iceland. *Journal of Volcanology and Geothermal Research*, *347*, 264-277.

Jeon, T., Kim, K. Y., & Woo, N. (2013). S-Wave Velocities Beneath Jeju Island, Korea, Using Inversion of Receiver Functions and the H-κ Stacking Method. *Geophysics and Geophysical Exploration*, *16*(1), 18-26.

Jiang, C., Schmandt, B., Farrell, J., Lin, F. C., & Ward, K. M. (2018). Seismically anisotropic magma reservoirs underlying silicic calderas. *Geology*, *46*(8), 727-730.

Jolivet, L., Faccenna, C., & Piromallo, C. (2009). From mantle to crust: Stretching the Mediterranean. *Earth and Planetary Science Letters*, *285*(1-2), 198-209.

Jolivet, L., Faccenna, C., Becker, T., Tesauro, M., Sternai, P., & Bouilhol, P. (2018). Mantle flow and deforming continents: From India□Asia convergence to Pacific subduction. *Tectonics*, *37*(9), 2887-2914.

Jung, H. (2017). Crystal preferred orientations of olivine, orthopyroxene, serpentine, chlorite, and amphibole, and implications for seismic anisotropy in subduction zones: a review. *Geosciences Journal*, *21*(6), 985-1011.

Kaislaniemi, L., & van Hunen, J. (2014). Dynamics of lithospheric thinning and mantle melting by edge□driven convection: Application to Moroccan Atlas mountains. *Geochemistry, Geophysics, Geosystems*, *15*(8), 3175-3189.

Kang, T.S., & Jun, M.S.(2011) Some studies on the 1952 earthquake near Pyeongyang, North Korea, The 1st Annual Meeting of the Project of Seismic Hazard Assessment for the Next Generation Map: Strategic Japanese-Chinese-Korean

Cooperative Program:Seismic Hazard Assessment for the Next Generation Map, November 25-30, 2011, Harbin, China, http://www.j-shis.bosai.go.jp/intl/cjk/1st_annual_meeting.html (last accessed in June 8, 2017)

Kang, T. S., & Shin, J. S. (2006). Surface□wave tomography from ambient seismic noise of accelerograph networks in southern Korea. *Geophysical Research Letters*, *33*(17).

Karato, S. I., Jung, H., Katayama, I., & Skemer, P. (2008). Geodynamic significance of seismic anisotropy of the upper mantle: new insights from laboratory studies. *Annu. Rev. Earth Planet. Sci.*, *36*, 59-95.

Kawakatsu, H., Kumar, P., Takei, Y., Shinohara, M., Kanazawa, T., Araki, E., & Suyehiro, K. (2009). Seismic evidence for sharp lithosphere-asthenosphere boundaries of oceanic plates. *Science*, *324*(5926), 499-502.

Kennett, B. L. N., Sambridge, M. S., & Williamson, P. R. (1988). Subspace methods for large inverse problems with multiple parameter classes. *Geophysical Journal International*, *94*(2), 237-247.

Kennett BLN, Engdahl ER, Buland R (1995) Constraints on seismic velocities in the Earth from traveltimes. Geophysical Journal International 122(1): 108-124.

Kim, J. I., Choi, S. H., Koh, G. W., Park, J. B., & Ryu, J. S. (2019). Petrogenesis and mantle source characteristics of volcanic rocks on Jeju Island, South Korea. *Lithos*, *326*, 476-490.

Kim, K. Y., & Hong, M. H. (2012). Shear-wave velocity structure of Jeju Island, Korea. *Geosciences Journal*, *16*(1), 35-45.

Kim, J., & Jung, H. (2019). New crystal preferred orientation of amphibole experimentally found in simple shear. *Geophysical Research Letters*, *46*(22), 12996-13005.

Kim, S., Rhie, J., & Kim, G. (2011). Forward waveform modelling procedure for 1-D crustal velocity structure and its application to the southern Korean Peninsula. *Geophysical Journal International*, *185*(1), 453-468.

Kim, S., Dettmer, J., Rhie, J., & Tkalčić, H. (2016). Highly efficient Bayesian joint inversion for receiver-based data and its application to lithospheric structure beneath the southern Korean Peninsula. *Geophysical Journal International*, *206*(1), 328-344.

Kim, S., Tkalčić, H., Rhie, J., & Chen, Y. (2016). Intraplate volcanism controlled by back□arc and continental structures in NE Asia inferred from transdimensional Bayesian ambient noise tomography, *Geophysical Research Letters*, 43, 8390-8398.

Kim, S., H. Tkalčić, and J. Rhie (2017), Seismic constraints on magma evolution beneath Mount Baekdu (Changbai) volcano from transdimensional Bayesian inversion of ambient noise data, *J. Geophys. Res.*, *122*, 5452–5473, doi:10.1002/2017JB014105.

King, S. D., & Anderson, D. L. (1998). Edge-driven convection. *Earth and Planetary Science Letters*, *160*(3-4), 289-296.

King, S. D., & Ritsema, J. (2000). African hot spot volcanism: small-scale convection in the upper mantle beneath cratons. *Science*, *290*(5494), 1137-1140.

Ko, B., & Jung, H. (2015). Crystal preferred orientation of an amphibole experimentally deformed by simple shear. *Nature communications*, *6*(1), 1-10.

Koh, G. W., Park, J. B., Kang, B. R., Kim, G. P., & Moon, D. C. (2013). Volcanism in Jeju Island. *Journal of the Geological Society of Korea*, *49*(2), 209-230.

Klügel, A., Hansteen, T. H., & Galipp, K. (2005). Magma storage and underplating beneath Cumbre Vieja volcano, la Palma (Canary Islands). *Earth and Planetary Science Letters*, *236*(1-2), 211-226.

Kyung, J., Kim, M., Lee, S., & Kim, J. (2016). An Analysis of Probabilistic Seismic Hazard in the Korean Peninsula- Probabilistic Peak Ground Acceleration (PGA) in Korean. *The Journal of The Korean Earth Science Society37*(1), 52-61.

Leary, P. C., Crampin, S., & McEvilly, T. V. (1990). Seismic fracture anisotropy in the Earth's crust: An overview. *Journal of Geophysical Research: Solid Earth*, *95*(B7), 11105-11114

Lee, S. J., & Rhie, J. (2015). Determining the orientations of broadband stations in south Korea using ambient noise cross-correlation. *Geophysics and Geophysical Exploration*, *18*(2), 85-90.

Lee, S. J., Rhie, J., Kim, S., Kang, T. S., & Kim, G. B. (2015). Ambient seismic noise tomography of the southern East Sea (Japan Sea) and the Korea Strait. *Geosciences Journal*, *19*(4), 709-720.

Lee, W., & Baag, C. E. (2008). Local crustal structures of southern Korea from joint analysis of waveforms and travel times. *Geosciences Journal*, *12*(4), 419-428.

Lei, J., & Zhao, D. (2005). P-wave tomography and origin of the Changbai intraplate volcano in Northeast Asia. *Tectonophysics*, *397*(3-4), 281-295.

Lei, J., Xie, F., Fan, Q., & Santosh, M. (2013). Seismic imaging of the deep structure under the Chinese volcanoes: an overview. *Physics of the Earth and Planetary Interiors*, *224*, 104-123.

Li, Z., Ni, S., Zhang, B., Bao, F., Zhang, S., Deng, Y., & Yuen, D. A. (2016). Shallow magma chamber under the Wudalianchi Volcanic Field unveiled by seismic imaging with dense array. *Geophysical Research Letters*, *43*(10), 4954-4961.

Lin, F. C., Moschetti, M. P., & Ritzwoller, M. H. (2008). Surface wave tomography of the western United States from ambient seismic noise: Rayleigh and Love wave phase velocity maps. *Geophysical Journal International*, *173*(1),281-298.

Liu, Y., Li, W., Feng, Z., Wen, Q., Neubauer, F., & Liang, C. (2017). A review of the Paleozoic tectonics in the eastern part of Central Asian Orogenic Belt. *Gondwana Research*, *43*, 123-148.

Liu, X., & Zhao, D. (2016). Seismic velocity azimuthal anisotropy of the Japan subduction zone: Constraints from P and S wave traveltimes. *Journal of Geophysical Research: Solid Earth*, *121*(7), 5086-5115.

Long, M. D., & Becker, T. W. (2010). Mantle dynamics and seismic anisotropy. *Earth and Planetary Science Letters*, *297*(3-4), 341-354.

Lü, Y., Li, J., Liu, L., & Zhao, L. (2019). Complex uppermost mantle structure and deformation beneath the Northwest Pacific region. *Journal of Geophysical Research: Solid Earth*.

Lynner, C., Beck, S. L., Zandt, G., Porritt, R. W., Lin, F. C., & Eilon, Z. C. (2018). Midcrustal Deformation in the Central Andes Constrained by Radial Anisotropy. *Journal of Geophysical Research: Solid Earth*.

Ma, J., Tian, Y., Liu, C., Zhao, D., Feng, X., & Zhu, H. (2018). P-wave tomography of Northeast Asia: Constraints on the western Pacific plate subduction and mantle dynamics. *Physics of the Earth and Planetary Interiors*, *274*, 105-126.

Ma, J., Tian, Y., Zhao, D., Liu, C., & Liu, T. (2019). Mantle dynamics of western Pacific and East Asia: New insights from P wave anisotropic tomography. *Geochemistry, Geophysics, Geosystems*, *20*(7), 3628-3658.

Mainprice, D. (2010). 16 Seismic Anisotropy of the Deep Earth from a Mineral and Rock Physics Perspective. *Treatise on Geophysics, Volume 2: Mineral Physics*, 437.

Maggi, A., Debayle, E., Priestley, K., & Barruol, G. (2006). Azimuthal anisotropy of the Pacific region. *Earth and Planetary Science Letters*, *250*(1-2), 53-71.

Masterlark, T., Haney, M., Dickinson, H., Fournier, T., & Searcy, C. (2010). Rheologic and structural controls on the deformation of Okmok volcano, Alaska: FEMs, InSAR, and ambient noise tomography. *Journal of Geophysical Research: Solid Earth*, *115*(B2).

McLean, C. E., Schofield, N., Brown, D. J., Jolley, D. W., & Reid, A. (2017). 3D seismic imaging of the shallow plumbing system beneath the Ben Nevis Monogenetic Volcanic Field: Faroe-Shetland Basin. *Journal of the Geological Society*, *174*(3), 468-485.

Meissner, R., Rabbel, W., & Kern, H. (2006). Seismic lamination and anisotropy of the lower continental crust. *Tectonophysics*, *416*(1-4), 81-99.

Montagner, J. P. (1998). Where can seismic anisotropy be detected in the Earth's mantle? In boundary layers... *Pure and Applied Geophysics*, *151*(2-4), 223-256.

Mordret, A., Rivet, D., Landès, M., & Shapiro, N. M. (2015). Three□ dimensional shear velocity anisotropic model of Piton de la Fournaise Volcano (La Réunion Island) from ambient seismic

noise. *Journal of Geophysical Research: Solid Earth*, *120*(1), 406-427.

Moschetti, M. P., Ritzwoller, M. H., Lin, F. C., & Yang, Y. (2010). Crustal shear wave velocity structure of the western United States inferred from ambient seismic noise and earthquake data. *Journal of Geophysical Research: Solid Earth*, *115*(B10).

Nakamura, E., McCulloch, M. T., & Campbell, I. H. (1990). Chemical geodynamics in the back-arc region of Japan based on the trace element and Sr-Nd isotopic compositions. *Tectonophysics*, *174*(3-4), 207-233.

Okaya, D., Christensen, N., Stanley, D., Stern, T., & Transect, S. I. G. (1995). Crustal anisotropy in the vicinity of the Alpine Fault zone, South Island, New Zealand. *New Zealand journal of geology and geophysics*, *38*(4), 579-583.

Park, K. H., Koh, D. C., Kim, Y. C., Moon, S. H., Seong, K. S., Shin, J. H., & Kim, G. Y. (2008). *Integrated analysis of groundwater occurrence in Jeju. Korea Institute of Geoscience and Mineral Resources*. GP2007-009-04-2008 (2), 365 p (in Korean with English abstract).

Park, K., Choi, S. H., Cho, M., & Lee, D. C. (2017). Evolution of the lithospheric mantle beneath Mt. Baekdu (Changbaishan):

constraints from geochemical and Sr–Nd–Hf isotopic studies on peridotite xenoliths in trachybasalt. *Lithos*, *286*, 330–344.

Pasyanos, M. E., Masters, T. G., Laske, G., & Ma, Z. (2014). LITHO1. 0: An updated crust and lithospheric model of the Earth. *Journal of Geophysical Research: Solid Earth*, *119*(3), 2153–2173.

Paulatto, M., Minshull, T. A., Baptie, B., Dean, S., Hammond, J. O., Henstock, T., & Ryan, G. (2010). Upper crustal structure of an active volcano from refraction/reflection tomography, Montserrat, Lesser Antilles. *Geophysical Journal International*, *180*(2), 685–696.

Pawlak, A., Eaton, D. W., Bastow, I. D., Kendall, J. M., Helffrich, G., Wookey, J., & Snyder, D. (2011). Crustal structure beneath Hudson Bay from ambient–noise tomography: implications for basin formation. *Geophysical Journal International*, *184*(1), 65–82.

Peltier, A., Staudacher, T., Bachèlery, P., & Cayol, V. (2009). Formation of the April 2007 caldera collapse at Piton de La Fournaise volcano: Insights from GPS data. *Journal of Volcanology and Geothermal Research*, *184*(1–2), 152–163.

Raddick, M. J., Parmentier, E. M., & Scheirer, D. S. (2002). Buoyant decompression melting: A possible mechanism for intraplate

volcanism. *Journal of Geophysical Research: Solid Earth*, *107*(B10), ECV-7.

Rawlinson, N., & Sambridge, M. (2005). The fast marching method: an effective tool for tomographic imaging and tracking multiple phases in complex layered media. *Exploration Geophysics*, *36*(4), 341-350.

Rhie, J., & Kim, S. (2010). Regional moment tensor determination in the southern Korean Peninsula. *Geosciences Journal*, *14*(4), 329-333.

Russell, J. B., Gaherty, J. B., Lin, P. Y. P., Lizarralde, D., Collins, J. A., Hirth, G., & Evans, R. L. (2019). High□Resolution Constraints on Pacific Upper Mantle Petrofabric Inferred From Surface□Wave Anisotropy. *Journal of Geophysical Research: Solid Earth*, *124*(1), 631-657.

Saikia, C. K. (1994). Modified frequency-wavenumber algorithm for regional seismograms using Filon's quadrature: modelling of Lg waves in eastern North America. *Geophysical Journal International*, *118*(1), 142-158.

Shapiro, N. M., Ritzwoller, M. H., Molnar, P., & Levin, V. (2004). Thinning and flow of Tibetan crust constrained by seismic anisotropy. *Science*, *305*(5681), 233-236.

Shen, W., Ritzwoller, M. H., Kang, D., Kim, Y., Lin, F. C., Ning, J., ... & Zhou, L. (2016). A seismic reference model for the crust and uppermost mantle beneath China from surface wave dispersion. *Geophysical Journal International*, *206*(2), 954-979

Shin, J. S., & Baag, C. E. (2000). Moho depths in the border region between northern Korea and northeastern China from waveform analysis of teleseismic pMP and pP phases. *Geosciences Journal*, *4*(4), 313-320.

Shervais, J. W., Vetter, S. K., & Hanan, B. B. (2006). Layered mafic sill complex beneath the eastern Snake River Plain: Evidence from cyclic geochemical variations in basalt. *Geology*, *34*(5), 365-368.

Shin, Y. H., Choi, K. S., Koh, J. S., Yun, S. H., Nakamura, E., & Na, S. H. (2012). Lithospheric□folding□based understanding on the origin of the back□arc basaltic magmatism beneath Jeju volcanic island. *Tectonics*, *31*(4).

Simutė, S., Steptoe, H., Cobden, L., Gokhberg, A., & Fichtner, A. (2016). Full□waveform inversion of the Japanese Islands region. *Journal of Geophysical Research: Solid Earth*, *121*(5), 3722-3741.

Song, J. H., Kim, S., Rhie, J., Lee, S. H., Kim, Y., & Kang, T. S. (2018). Imaging of lithospheric structure beneath Jeju Volcanic Island by teleseismic traveltime tomography. *Journal of Geophysical Research: Solid Earth*, *123*(8), 6784-6801.

Spica, Z., Legrand, D., Iglesias, A., Walter, T. R., Heimann, S., Dahm, T., & Pardo, M. (2015). Hydrothermal and magmatic reservoirs at Lazufre volcanic area, revealed by a high-resolution seismic noise tomography. *Earth and Planetary Science Letters*, *421*, 27-38.

Spica, Z., Perton, M., & Legrand, D. (2017). Anatomy of the Colima volcano magmatic system, Mexico. *Earth and Planetary Science Letters*, *459*, 1-13.

Stankiewicz, J., Ryberg, T., Haberland, C., & Natawidjaja, D. (2010). Lake Toba volcano magma chamber imaged by ambient seismic noise tomography. *Geophysical Research Letters*, *37*(17)

Tamaki, K. (1988). *Geological structure of the Japan Sea and its tectonic implications*. Geological Survey of Japan.

Tao, K., Grand, S. P., & Niu, F. (2018). Seismic structure of the upper mantle beneath Eastern Asia from full waveform seismic tomography. *Geochemistry, Geophysics, Geosystems*, *19*(8), 2732-2763.

Tibaldi, A. (2015). Structure of volcano plumbing systems: A review of multi-parametric effects. *Journal of Volcanology and Geothermal Research*, *298*, 85-135.

Till, C. B., Elkins□Tanton, L. T., & Fischer, K. M. (2010). A mechanism for low□extent melts at the lithosphere□asthenosphere boundary. *Geochemistry, Geophysics, Geosystems*, *11*(10).

Van Horne, A., Sato, H., & Ishiyama, T. (2017). Evolution of the Sea of Japan back-arc and some unsolved issues. *Tectonophysics*, *710*, 6-20.

van Wijk, K., Mikesell, T. D., Schulte-Pelkum, V., and Stachnik J., 2011, Estimating the Rayleigh-wave impulse response between seismic stations with the cross terms of the Green tensor, Geophysical Research Letters, 38, L16301

Wang, Q., Song, X., & Ren, J. (2017). Ambient noise surface wave tomography of marginal seas in east Asia. *Earth and Planetary Physics*, *1*(1), 13-25.

Wang, Y., Li, C., Wei, H., & Shan, X. (2003). Late Pliocene-recent tectonic setting for the Tianchi volcanic zone, Changbai Mountains, northeast China. *Journal of Asian Earth Sciences*, *21*(10), 1159-1170.

Ward, K. M., Zandt, G., Beck, S. L., Christensen, D. H., & McFarlin, H. (2014). Seismic imaging of the magmatic underpinnings beneath the Altiplano-Puna volcanic complex from the joint inversion of surface wave dispersion and receiver functions. *Earth and Planetary Science Letters*, *404*, 43-53.

Wei, H., Wang, Y., Jin, J., Gao, L., Yun, S. H., & Jin, B. (2007). Timescale and evolution of the intracontinental Tianchi volcanic shield and ignimbrite-forming eruption, Changbaishan, Northeast China. *Lithos*, *96*(1-2), 315-324.

Wei, W., Xu, J., Zhao, D., & Shi, Y. (2012). East Asia mantle tomography: New insight into plate subduction and intraplate volcanism. *Journal of Asian Earth Sciences*, *60*, 88-103.

Witek, M., van der Lee, S., & Kang, T. S. (2014). Rayleigh wave group velocity distributions for East Asia using ambient seismic noise. *Geophysical Research Letters*, *41*(22), 8045-8052.

Yang, J., Zhao, L., Kaus, B. J., Lu, G., Wang, K., & Zhu, R. (2018). Slab-triggered wet upwellings produce large volumes of melt: Insights into the destruction of the North China Craton. *Tectonophysics*, *746*, 266-279.

Yao, H., van Der Hilst, R. D., & Maarten, V. (2006). Surface-wave array tomography in SE Tibet from ambient seismic noise and two-station analysis—I. Phase velocity maps. *Geophysical Journal International*, *166*(2), 732-744.

Yoon, S., Jung, C. Y., Hyun, W. H., & Song, S. T. (2014). Tectonic history of Jeju Island. *Journal of the Geological Society of Korea*, *50*(4), 457-474.

Yuan, H., & Romanowicz, B. (2010). Depth dependent azimuthal anisotropy in the western US upper mantle. *Earth and Planetary Science Letters*, *300*(3-4), 385-394.

Zha, Y., Webb, S. C., and Menke, W., 2013, Determining the orientations of ocean bottom seismometers using ambient noise correlation. Geophysical Research Letters, 40(14), 3585-359.

Zhao, D. (2017). Big mantle wedge, anisotropy, slabs and earthquakes beneath the Japan Sea. *Physics of the Earth and Planetary Interiors*, *270*, 9-28.

Zhang, M., Guo, Z., Liu, J., Liu, G., Zhang, L., Lei, M., ... & Ventura, G. (2018). The intraplate Changbaishan volcanic field (China/North Korea): A review on eruptive history, magma genesis, geodynamic significance, recent dynamics and potential hazards. *Earth-science reviews*, *187*, 19-52. 0.

Zheng, Y., Shen, W., Zhou, L., Yang, Y., Xie, Z., & Ritzwoller, M. H. (2011). Crust and uppermost mantle beneath the North China Craton, northeastern China, and the Sea of Japan from ambient noise tomography. *Journal of Geophysical Research: Solid Earth*, *116*(B12).

Abstract (in Korean)

유라시아판의 동부는 태평양판과 필리핀 해양판의 섭입 등 복합적인 구조운동은 겪었다. 이 때문에 이 지역에 산발적으로 분포하는 확장 분지들과 판내부 화산들은 하나의 기작으로 설명하기 쉽지 않다. 따라서 이 지역에서 발생하는 지진 활동과 복잡한 구조사를 이해하기 위해서는 신뢰도 있는 속도구조 모델이 필요하다. 이에 본 논문에서는 배경잡음 방법을 이용하여 동북아시아 지역에 대한 속도구조 모델을 작성했다. 배경잡음 방법은 지각과 상부맨틀의 속도구조 연구를 위해 통용되는 방법 중 하나이다. 이 방법은 지진 자료에 비해 지각 깊이를 지나는 단주기 자료를 얻기에 유리하며, 표면파의 장주기 신호를 사용하면 상부맨틀 깊이까지 속도구조를 구할 수 있다. 또한 이 방법은 관측소 사이 배경잡음의 상호상관 함수로부터 구한 그린함수(Green’s function)를 이용하기 때문에 지진발생빈도가 적거나 연구지역내에 위치한 관측소의 수가 적더라도 사용가능하다. 따라서 본 논문에서는 배경잡음 방법을 동북아시아지역의 다양한 관측망을 활용하여 이 지역의 특정지역에 대한 다양한 크기의 속도구조 모델을 만들었다.

첫 번째로, 북한의 내륙과 동해안에 대한 속도구조 모델을 중국과 남한의 관측망으로부터 얻은 레일리파 분산곡선 자료를 베이지안 역산을 통해 구했다. 그리고 구해진 모델을 2013년 북핵지진에 대한 풀 모멘트 텐서 역산을 통해 평가했다. 그 결과, 작성된 북한의 내륙과 동해안에 대한 속도구조 모델을 경로 따라 함께 사용하는 것이 기존의 속도구조 모델을 사용한 경우보다 더 좋은 역산 결과를 보이는 것으로 나타났다. 이는 북한지역을 지나는 파의 경로 효과를 고려함으로써 지진활동 관측

효과를 증대시킬 수 있음을 보여준다. 따라서 경로에 따른 모델은 북한지역에서 발생하는 자연지진 및 인공지진의 특성을 연구하고 관측하는데 유용할 것으로 보인다.

두 번째로, 제주도에 설치한 임시관측망 자료를 활용하여 제주도 상부지각에 대한 등방 및 이방성 속도구조 모델을 작성했다. 2-15 초 주기의 레일리판와 러프파의 군속도 및 위상속도의 분산 자료를 계층적이고 유동 차원적인(transdimensional) 베이지안 역산을 통해 함께 역산하여 제주도 하부 10 km 깊이에 대한 등방 및 이방성 속도구조 모델을 작성했다. 결과를 보면 2 km 보다 얕거나 5 km 보다 깊은 곳에서는 음의 이방성 ($V_{SH} < V_{SV}$)이 우세한 것으로 보이는데, 이는 지표 나타난 400개 이상의 오름들과 연관된 관입암 복합체 및 더 깊은 곳으로부터 마그마를 운반하는 수직적 공급구조를 각각 지시하는 것으로 볼 수 있다. 한편, 2-5 km 구간에서는 양의 이방성 ($V_{SH} > V_{SV}$)이 우세하며 이는 다른 화산에서 보고된 적이 있는 마그마의 수평적 공급에 의한 구조로 볼 수 있다. 한라산 중심에서 이 양의 이방성이 나타나는 층은 상부의 상대 속도가 빠른 구간과 그 하부의 상대 속도가 느린 구간으로 나눌 수 있다. 이러한 구조는 먼저 관입하여 충분히 식은 수평관입 구조와 아직 충분히 식지 않았거나 일부 녹아있을 가능성이 있는 하부의 따뜻한 수평관입 구조를 지시하는 것으로 볼 수 있다. 이러한 다층적인 구조는 제주도 하부로부터 지표로 이어지는 제주도 중심부의 복잡한 마그마 공급 구조를 지시하는 것으로 볼 수 있다.

마지막으로, 동해와 그 주변지역에 대한 방사상 이방성 (radial anisotropy) 모델을 레일리판와 러프파의 군속도 및 위상속도의 분산

자료를 계층적이고 유동 차원적인(transdimensional) 베이지안 역산을 통해 작성했다. 총 237개의 관측소를 이용하여 55,000개 이상의 러브파 군속도 및 위상속도 분산곡선을 5-60 초 주기에 대해 구했다. 그리고 이를 같은 지역에 대한 기존연구의 레일리파 분산곡선 자료 및 전지구 모델로부터 얻은 장주기 (70-200 초)의 레일리파 및 러브파 분산곡선 자료를 함께 역산했다. 이를 통해 연구지역 하부 160 km 깊이에 대한 3차원 이방성 델을 작성했다. 모델에서 나타나는 가장 주목할 점은 강한 양의 이방성 구간의 두께와 깊이 변화 양상이다. 양의 이방성이 강한 구간은 대륙하부에서 약 70-150 km 사이에 나타나지만, 신생대 확장을 겪은 동해에서는 주로 30-60 km의 상대적으로 더 얕은 구간에서 얇게 나타난다. 이는 암석권 깊이 변화 및 그로 인한 복잡한 동력학적 구조운동의 결과로 인한 암석권-연약권 경계의 깊이 변화에 따른 것으로 보인다.

주요어 : 배경잡음 영상화, 한반도, 북핵실험, 표면파, 베이지안 역산, 방사상 이방성, 지진파 속도 구조, 제주도, 동해

학번 : 2014-30089